Stony Brook University

The Mechanisms of NMDA Receptor Activation

A Dissertation Presented

by

Rashek Kazi

to

The Graduate School

in Partial Fulfillment of the

Requirements

for the Degree of

Doctor of Philosophy

in

Neuroscience

Stony Brook University

May 2014

Stony Brook University

The Graduate School

Rashek Kazi

We, the dissertation committee for the above candidate for the

Doctor of Philosophy degree, hereby recommend

acceptance of this dissertation.

Lonnie P. Wollmuth, Ph.D. – Dissertation Advisor
Professor, Department of Neurobiology and Behavior

Mark E. Bowen, Ph.D. - Chairperson of Defense
Associate Professor, Department of Physiology and Biophysics

Dennis W. Choi, M.D., Ph.D.
Professor and Chair, Department of Neurology

James R. Howe, Ph.D.
Professor, Pharmacology, Yale University

Michelino Puopolo, Ph.D.
Assistant Professor, Department of Anesthesiology

This dissertation is accepted by the Graduate School

Charles Taber

Dean of the Graduate School

Abstract of the Dissertation

The Mechanisms of NMDA Receptor Activation

by

Rashek Kazi

Doctor of Philosophy

in

Neuroscience

Stony Brook University

2014

Glutamate-gated ion channels embedded within the neuronal membrane are the primary mediators of fast excitatory synaptic transmission in the central nervous system. The ion channel of these glutamate receptors contains a pore-lining transmembrane M3 helix surrounded by peripheral M1 and M4 helices. In the NMDA receptor (NMDAR), opening of the ion channel pore requires rearrangements of these helical elements, but there is currently no functional model for how this occurs.

To address how agonist binding is transduced into pore opening in NMDARs, we manipulated the coupling between the ligand binding domain (LBD) and the M3 helix of the ion channel by inserting residues in a linker between them. We find that a single residue insertion dramatically attenuates the ability of NMDARs to convert a glutamate transient into a functional response. Computational and thermodynamic analyses suggest that insertions prevent the agonist-bound LBD from effectively pulling on pore lining elements, thereby destabilizing pore opening. Further, this pulling energy is more prominent in the GluN2 subunit. We conclude that an efficient NMDAR-mediated synaptic response relies on a mechanical coupling between the LBD and the ion channel.

We then sought to understand how the peripheral elements contribute to pore opening. We approached this question by constraining the relative movements of the linkers that connect these helices to the LBD using engineered cross-links, either within or between subunits. Constraining the peripheral linkers in any manner dramatically curtailed channel opening, highlighting the requirement for rearrangements of these peripheral structural elements for efficient gating to occur. However, the magnitude of this gating effect was most dramatic when the constraint was between subunits. Our results suggest an asynchrony in the displacement of the peripheral elements during the conformational and energetic changes leading to pore opening. Thus, the conformational changes induced by agonist binding in NMDA receptors converge asynchronously to permit pore opening.

Dedication Page

To my brothers.

Table of Contents

List of Figures

Supplementary Figures

List of Tables

List of Supplementary Tables

List of Equations

List of Abbreviations

iGluRs:	ionotropic glutamate receptors
NMDAR:	N-methyl-D-aspartate receptor
AMPAR:	a-amino-3-hydroxy-4-isoxazolepropionic acid receptor
EPSP:	Excitatory post synaptic potential
EPSC:	Excitatory post synaptic current
GABA:	Gamma amino butyric acid
TARP:	Transmembrane AMPAR regulatory protein
MAGuK:	Membrane associated guanylate kinase
LTP:	Long term potentiation
LTD:	Long term depression
HFS:	High frequency stimulation
LFS:	Low frequency stimulation
APV:	Amino-5-phosphonovaleric acid
CaMK-II:	Calmodulin dependent kinase II
DAPK1:	Death associated protein kinase 1
nNos1:	Neuronal nitric oxide synthase 1
PD:	Parkinson’s disease
BECTS:	Benign epilepsy with centrotemporal spikes
APBE:	Atypical benign partial epilepsy
ARE:	Atypical rolandic epilepsy
CSWS:	Epileptic encephalopathy with continuous spike and wave during sleep
LKS:	Landau Kleffner syndrome

MR:	Mental retardation
ATD:	Amino terminal domain
LBD:	Ligand binding domain
TMD:	Transmembrane domain
CTD:	Carboxy-terminal domain
nAChR:	Nicotinic acetylcholine receptor
KNF:	Koshland-Nemethy-Filmer
MWC:	Monod-Wyman-Changeux
KCl:	Potassium chloride
HEPES:	2-[4-(2-hydroxyethyl) piperazin-1-yl] ethanesulfonic acid
EGFP:	Enhanced green fluorescent protein
Hz:	Hertz
mM:	milli-Molar
NaOH:	Sodium Hydroxide
BAPTA:	1,2-bis(o-aminophenoxy)ethane-N,N,N’,N’-tetraacetic acid
SKM:	Segmental K-means
MIL:	Maximum interval likelihood
MOT:	Mean Open Time
MCT:	Mean Closed Time
RMSD:	Root mean squared deviation
P_o:	Open probability
LL:	Log-likelihood
K_{eq}:	Equilibrium constant

Acknowledgments

I first want to acknowledge Janet Allopenna – she was instrumental to all of the projects presented in this thesis and for that I am forever grateful. She performed a multitude of jobs in the lab and, more importantly, was very encouraging and friendly to all of us in the lab. Without her help, I would not have accomplished the majority of my goals.

I would like to thank my advisor, Lonnie Wollmuth, for his efforts in training me. We worked very hard together as a team to produce some truly inspiring and fantastic science. I would also like to thank the other members of the Wollmuth Lab, both past and present. I would specifically like to thank Quan 'Alfred' Gan. We worked very hard on multiple projects together and ultimately helped each other stay afloat and succeed in the lab.

Vita, Publications and/or Fields of Study

Research Papers

1. **Kazi R**, Dai J, Sweeney C, Zhou H-X, Wollmuth LP (2014). Mechanical coupling maintains the fidelity of NMDA receptor-mediated currents. Accepted, in press. Nature Neuroscience.

2. **Kazi R***, Gan Q*, Talukder I, Salussolia CL, Markowitz M, Wollmuth LP (2013). Asynchronous Movements Prior to Pore Opening in NMDA Receptors. Accepted, published. Journal of Neuroscience. * - equal contribution

3. Choi UB, **Kazi R**, Stenzoski N, Wollmuth LP, Uversky VN, Bowen ME (2013). Modulating the intrinsic disorder in the cytoplasmic domain alters the biological activity of the N-methyl D-aspartate-sensitive glutamate receptor. Accepted, published. J Biol Chem. 2013

4. Salussolia CL, Gan Q, **Kazi R**, Singh P, Allopenna J, Furukawa H, Wollmuth LP (2013). A Eukaryotic Specific Transmembrane Segment is Required for Tetramerization in AMPA Receptors. Accepted, published. Journal of Neuroscience.

5. **Kazi R***, Talukder I*, Wollmuth LP (2011)**.** GluN1-specific redox effects on the kinetic mechanism of NMDA receptor activation. Accepted, published. Biophysical Journal.* - equal contribution

6. Salussolia CL, Corrales A, Talukder I, **Kazi R**, Akgul, G, Bowen M, Wollmuth, LP. (2011) Interaction of the M4 segment with other transmembrane segments is required for efficient trafficking of AMPA receptors. Accepted, published. Journal of Biological Chemistry.

Textbook Chapters

1. **Kazi R**, Daniel M, Wollmuth LP. Characterizing the thermodynamics of NMDA receptor pore opening (2014). Technologies in Glutamate Receptor Physiology. Under Review.

Abstracts/Posters/Presentations

1. **R. Kazi**, J. Dai, M. Daniel, H-X. Zhou, LP. Wollmuth (2014). Energetic Coupling of the ligand-binding domain to pore opening in NMDA receptors. Biophysical Society. Platform talk

2. **R. Kazi**, LP. Wollmuth (2013). Tension Forces Drive Pore Opening in NMDA Receptors. Regional Glutamate Receptor Retreat. Cornell University. Platform talk

3. Q. Gan, C.L. Salussolia, **R. Kazi**, H. Furukawa, L. P. Wollmuth (2013) Mechanisms underlying ionotropic glutamate receptor oligmerization. Society for Neuroscience. Poster

4. **R. Kazi,** J. Dai, T. Jin, H.-X Zhou, L.P. Wollmuth (2013) Biophysical Coupling Mechanisms in NMDA receptor gating. Biophysical Society. Poster

5. Q. Gan, C. L. Salussolia, **R. Kazi**, L. P. Wollmuth (2013) Structural mechanisms underlying AMPA receptor oligmerization. Biophysical Society. Poster

6. **R. Kazi**, J. Dai, H.-X. Zhou, L.P. Wollmuth. (2012) Subunit specificity in linker tension during NMDA receptor gating. Society for Neuroscience. Poster

7. **R.Kazi**, I. Talukder, L.P. Wollmuth (2012) Electrostatics in the NMDA Receptor Transduction Pathway Alter Gating. Biophysical Society. Poster

8. **R. Kazi^,** I.Talukder, Q. Gan, C. Salussolia, M. Markowitz, L.P. Wollmuth (2012) Conformational Mobility of S1-M1 and S2-M4 Linkers Influence NMDA Receptor Gating**.** Biophysical Society. ^ - added post-submission

9. Talukder, **R.Kazi**, L.P. Wollmuth (2011) Constraining Gating Actions of Specific Subunits During NMDA Receptor activation. Biophysical Society. Poster

10. Corrales, A, I. Talukder, **R. Kazi**, and L. P. Wollmuth (2008) Channel gating in mammalian glutamate receptors requires the interaction of the M4 segment with other transmembrane elements. Society for Neuroscience. Poster

MECHANISMS OF NMDA RECEPTOR ACTIVATION

CHAPTER 1: INTRODUCTION

Fast communication between neurons in the nervous system occurs at highly specialized structures called synapses. Neuron-to-neuron signaling at synapses is mediated by chemical messengers known as neurotransmitters. Neurotransmitters are released from one neuron (the presynaptic neuron) and impact the function of the neighboring neuron (the postsynaptic neuron), typically by ligand-gated ion channels. Rapid chemical-to-electrical signaling is the basis for communication between neighboring neurons and across multiple neurophysiological networks. Tuning synaptic transmission mediates higher cognitive functions such as learning and memory. Mutations which perturb chemical-to-electrical signaling have been implicated in an array of neurodegenerative as well as psychiatric pathologies including autism spectrum disorders and schizophrenia. As such, delineating the molecular basis of synaptic signaling is vital from scientific and clinical perspectives.

Fast synaptic transmission in the central nervous system can be broadly defined as either excitatory or inhibitory. In general, excitatory transmission generates postsynaptic depolarization, which increases the likelihood of action potential generation; inhibitory transmission generates postsynaptic hyperpolarization, which reduces the likelihood of action potential generation. The neurotransmitter glutamate mediates the majority of excitatory synapses. Inhibitory synapses are mediated by gamma-aminobutyric acid (GABA) in the brain or glycine in the spine.

A hallmark of synapses is rapid communication. At fast chemical synapses mediated by the neurotransmitter glutamate, presynaptic calcium currents and vesicle fusion requires approximately 0.3 ms (Diamond and Jahr, 1995; Isaacson and Walmsley, 1995). The released glutamate reaches a peak cleft concentration of 1 mM within 0.1 ms (Raghavachari and Lisman,

2004) and subsequent opening of postsynaptic receptors requires an additional 0.1-0.2 ms (Forti et al., 1997; Smith et al., 2003). As such, the molecular events which take place during synaptic activation must work rapidly to maintain synaptic communication.

Conversion of the transient neurotransmitter into opening of the ion channel is a key step in synaptic transmission (Figure 1). Channel opening involves all of the conformational changes throughout the receptor that culminate in a pore-open configuration. What remains unknown is how agonist binding and pore opening are interconnected. Indeed, because the neurotransmitter signal is so transient, the speed and efficiency of pore opening determines the fidelity of synaptic signaling.

To better understand mechanisms of ion channel activation, scientists perform structure-function studies (Stuhmer, 1991; Hille, 2001). Structure-function experiments use current knowledge of protein structure to predict phenotypes and these functional outcomes are then used to modify our understanding of protein structure, upon which the cycle is repeated until a full model of ion channel activation can be derived. In the context of ligand-gated ion channels, there were three major technical advances, which propelled structure-function studies: electrophysiogical techniques (including single-channel resolution electrophysiology), molecular cloning, and single-protein structural studies. Detailed electrophysiology allowed scientists to probe the function of ion channels in both native and heterologous environments while molecular cloning and structural studies better elucidated the structural basis of protein function (Hille, 2001).

The interplay between these three techniques is elegantly told in the story of the potassium channel. Electrophysiological studies of potassium channels allowed scientists to discern functional metrics such as permeability, conductance, current-voltage relationships, etc.

(Hodgkin and Huxley, 1952; Armstrong and Bezanilla, 1974; Bezanilla et al., 1982). Following this, site-directed mutagenesis of the recombinant protein led to preliminary schematics of the channel architecture as well as educated guesses regarding the atomic details of the selectivity filter and the ion channel pore. In 1998, the first high-resolution structure of a full-length potassium channel not only revealed that much of the functional studies had indeed predicted correctly, but it also revealed novel structural elements, which were previously unexplored (Doyle et al., 1998). As such, the potassium channel field has grown even further with the availability of structures because it now allows for more detailed work to elucidate the mechanics of potassium channel activation. Thus, this streamlined process has vastly advanced the field of ion channel structure-function research.

Ionotropic glutamate receptors (iGluRs) are ligand-gated ion channels embedded in postsynaptic membranes of those that use glutamate. After glutamate binding, iGluRs undergo molecular transformations, converting the channel into a pore open conformation that conducts cations. As of yet, the detailed mechanisms and structure-function relationships of iGluR pore opening remain unknown. To approach this broad question, I studied the NMDA receptor (NMDAR) subfamily of iGluRs. While agonist binding is the initial driving force of function, much of my work focuses on the real-time dynamics between neurotransmitter binding and pore opening. Efficient opening of NMDARs is critical to neuronal maturation, learning and memory, and controlled apoptosis. From a clinical perspective, mutations within the NMDAR can lead to pathologies ranging from schizophrenia to epileptic encephalopathy. As such, it is vital to determine the structural and energetic basis of fast synaptic activity in NMDARs as it can lead to better understanding of pathological phenomena and drive the development of pharmacological therapeutics.

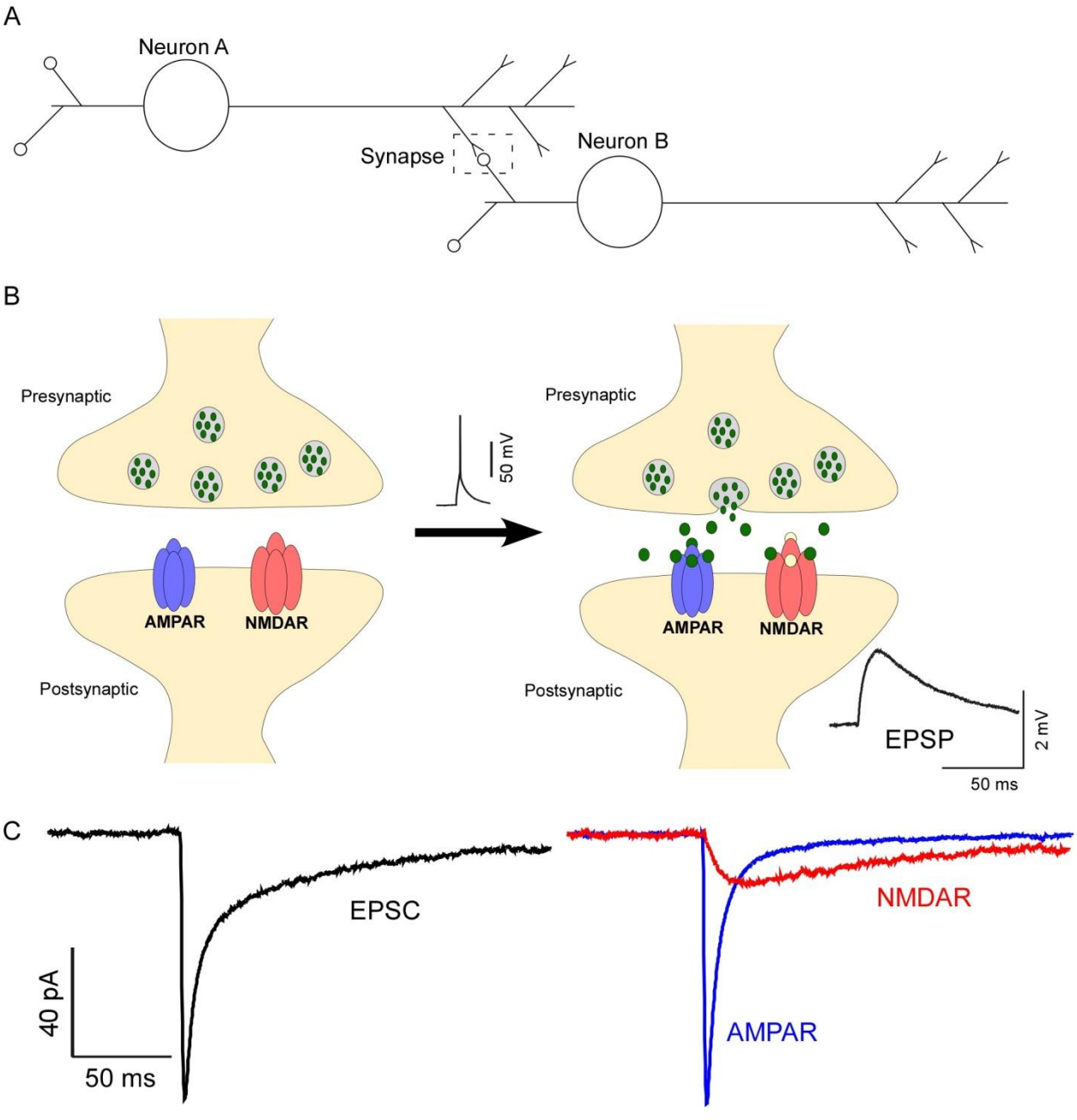

Figure 1.1 Glutamate-mediated excitatory synaptic transmission

(A & B) A glutamatergic synapse with AMPARs and NMDARs at the postsynaptic membrane. The presynaptic terminal is shown with vesicles filled with the neurotransmitter glutamate. The depolarization of this terminal by a presynaptic action potential drives vesicle fusion and consequent release of glutamate into the synaptic cleft. Activation of postsynaptic iGluRs generates an excitatory postsynaptic potential (EPSP).
(C) *Left*, Excitatory postsynaptic current (EPSC). *Right*, AMPAR (blue) and NMDAR (red) component of EPSC.

Physiology and biophysics of iGluRs at fast excitatory synapses

At glutamatergic synapses, glutamate binds to and activates postsynaptic AMPA and NMDA receptor iGluR subtypes (Figure 1B). Some synapses also express kainate receptor subtype, though they will not be further discussed. Open iGluRs pass a depolarizing cationic current, known as the as the excitatory postsynaptic current (EPSC), which generates an excitatory postsynaptic potential (EPSP). AMPARs contribute to the fast component of the EPSC while NMDARs contribute to the relatively slower component (Figure 1C). This unique interplay between AMPARs and NMDARs is critical to normal synaptic transmission as well as synaptic plasticity.

The number, subtype, and subunit composition of iGluRs at the postsynaptic membrane is the primary determinant of the magnitude and time course of glutamate-mediated EPSCs. Further, each iGluR subtype and subunit has distinct biophysical features. Biophysically, iGluR opening is characterized by activation (the rate at which the current through the open channel reaches its peak amplitude); deactivation (the rate at which the current decays following removal of agonist); and desensitization (the degree and rate at which the current decays in the continuous presence of agonist.

General biophysical properties of iGluRs are summarized in Table 1.1.

NMDAR

Subunit Composition of NMDARs

There are seven different NMDAR subunits, each encoded by its own gene: GluN1, GluN2(A-D), and GluN3(a-b). NMDARs are obligate heterotetramers; they always contain two glycine-binding GluN1 subunits. The other subunits in the complex could be glutamate-binding GluN2 subunits and/or glycine-binding GluN3 subunits. Most synaptic NMDARs are GluN1 and

GluN2 containing. In general, GluN1/GluN2A and GluN1/GluN2B (referred to as group I) NMDARs share common gating and permeation/block properties that are distinct from GluN1/GluN2C and GluN1/GluN2D (referred to as group II) NMDARs (Table 1.1). Subunit expression is tissue specific and also varies throughout development, with a notable switch between GluN2B-containing NMDARs early in development to GluN2A-containing NMDARs later in development (Traynelis et al., 2010).

Synaptic Activation of NMDARs

The co-agonists glycine and glutamate are required to activate NMDARs (Johnson and Ascher, 1987; Kleckner and Dingledine, 1988). At certain synapses, however, D-serine is the endogenous GluN1 agonist (Mothet et al., 2000; Panatier et al., 2006). The GluN1 subunit has a high affinity for glycine and, as such, ambient glycine (~20 μM) will cause the GluN1 subunit to be tonically agonist bound. Therefore, synaptically released glutamate drives NMDAR opening (Van Hove et al., 1993; Qian and Johnson, 2002).

Relative to AMPARs, NMDARs have slow macroscopic gating kinetics in terms of activation, deactivation, and desensitization (Table 1.1). NMDARs are also largely resistant to desensitization; GluN1/GluN2A desensitizes the most among NMDARs at ~50%. Group I NMDARs have larger single-channel conductance levels (~50 pS) than group II NMDARs (~35 pS). Under physiological conditions (i.e. in the presence of calcium), both groups have a second conductance level. In addition, group I NMDARs also have a greater open probability compared to group II NMDARs. Thus, group I NMDARs generally produce higher ensemble and peak current amplitudes relative to group II NMDARs. Within group I, there are critical biophysical differences. For example, GluN1/GluN2A and GluN1/GluN2B receptors show substantial differences in the rates of activation and deactivation (Erreger et al., 2005a). This is important

physiologically as there are developmental changes in group I NMDAR expression (Monyer et al., 1994).

Permeation and Block of NMDARs

Upon pore opening, NMDARs pass monovalent cations, as well as calcium. Group I NMDARs pass more calcium than group II NMDARs (Table 1.1) (Burnashev et al., 1995; Siegler Retchless et al., 2012). Calcium activates pathways involved in NMDAR-dependent synaptic plasticity (see Synaptic Plasticity and iGluRs). Further, calcium influx is involved in cell survival and apoptosis, as excess calcium influx can trigger neuronal death (see Pathophysiology of iGluRs). As such, NMDAR activation is central to the calcium mediated functions within the neuron.

At resting membrane potentials (~ -70 mV), the NMDAR ion channel pore is blocked by magnesium (Mayer et al., 1984; Nowak et al., 1984). Both groups of NMDARs are blocked by magnesium, though the block is stronger for group I NMDARs (Kuner and Schoepfer, 1996; Siegler Retchless et al., 2012). Therefore, weak activation of synapses will not generate a substantial NMDAR-mediated current. However, depolarization of the postsynaptic membrane will rapidly unblock the pore. Glutamate activation of synaptic AMPARs leads to a transient depolarization of the local postsynaptic membrane. This strong activation will lead to NMDAR unblock, allowing for calcium influx. Thus, presynaptic and postsynaptic events must work in synchrony to permit NMDAR activation. As such, NMDARs serve as molecular coincidence detectors.

NMDAR interacting partners and modulation

NMDARs interact with an array of proteins at the post-synaptic membrane. The majority of these proteins are scaffolding proteins which are involved in NMDAR trafficking and

membrane localization. Indeed, the intracellular C-terminal domains of GluN2 subunits contain motifs, which bind membrane associated guanylate kinases (MAGuKs). These proteins associate with NMDARs at the post-synaptic membrane at synaptic and extra-synaptic locations. Interestingly, mouse lines, which lack certain MAGuKs tend to show specific learning deficiencies, which may be associated with autism. Therefore, altered MAGuK-mediated trafficking of NMDARs may be central to the pathogenesis of learning disabilities.

Endogenous biomolecules and ions modulate NMDAR function in a subunit-specific manner. Zinc, protons, and calcium ions inhibit GluN1/GluN2A NMDAR gating. While this effect is strong in GluN2A-containing NMDARs, GluN2A-lacking NMDARs are largely resistant to zinc inhibition, though it is unclear why (Paoletti et al., 1997). This allows for a unique pharmacological advantage in that drugs can be developed to allow for subunit-specific modulation.

Several forms of activity dependent modulation of activation and desensitization have been characterized, including glycine dependent/independent (Lerma et al., 1990; Villarroel et al., 1998), calcium dependent/independent (Rosenmund et al., 1995; Krupp et al., 1996)., and voltage dependent/ independent modulation (Clarke and Johnson, 2008). Mechanistically, these forms of modulation remain poorly defined but are thought to be due to activation of secondary messengers such as calmodulin dependent kinase and protein kinase A. As these forms of modulation require persistent channel activity, they only arise physiologically upon rapid or tetanic synaptic activity.

	AMPARs		NMDARs		
	A2-containing	A2-lacking	N2A	N2B	N2C/N2D
Activation (ms)	Fast (< 1)	Fast (< 1)	Slow (<10)	Slow (<10)	Slow (<10)
Deactivation (ms)	Fast (~1)	Fast (~1)	Slow (20-200)	Slow (70-600)	Slow (200-4000)
Desensitization (rate, ms)	Fast (6)	Fast (1-5)	Slow (500-2000)	Slow (100-500)	NA
Desensitization (extent, %)	High (~90-95)	High (~99)	Mid (30-50)	Mid (30-50)	Low (< 5)
Conductance (pS)	Low (0.2-0.5)	Low (4-35)	High (51, 40)	High (51, 40)	Mid (35, 20)
Open Probability	?	High (0.4-1)	Mid (0.5)	Low (0.2)	Low (0.01-0.05)
Ca-Permeability (%)	0	3-4	12-14	12-14	8-10
Block	Low	Polyamine	Strong Mg^{+2}	Strong Mg^{+2}	Weak Mg^{+2}

Table 1.1 General biophysical properties of iGluRs

Calcium permeability is shown as a percent of total current at -60 mV.
Values were derived from personally collected data and various sources (Schneggenburger, 1996; Swanson et al., 1997; Prieto and Wollmuth, 2010; Traynelis et al., 2010; Siegler Retchless et al., 2012).

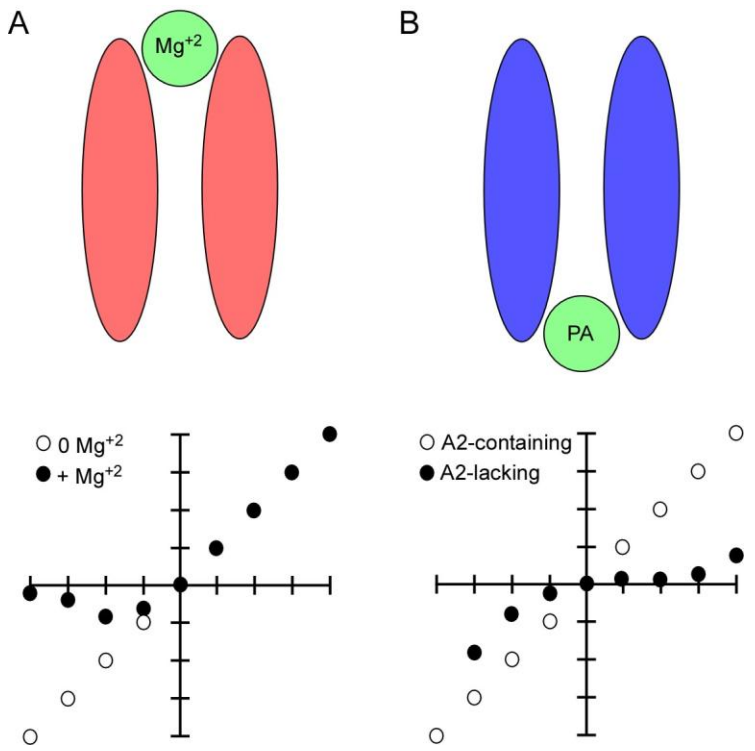

Figure 1.2 Current voltage relationships of NMDARs and AMPARs

(A) At negative membrane potentials, NMDARs are blocked by extracellular magnesium (*top*). This results in an outwardly rectifying current-voltage relationship (*bottom, black circles*). In the absence of magnesium, NMDARs display a linear current-voltage relationship (*bottom, white circles*).

(B) GluA2-lacking AMPARs undergo intracellular block by polyamines at positive membrane potentials (*top*). As such, GluA2-lacking AMPARs tend to display inwardly rectifying current-voltage relationships (*bottom, black circles*). However, GluA2-containing AMPARs are resistant to polyamine block and as such display a linear current-voltage relationship (*bottom, white circles*).

iGluRs and Synaptic Plasticity

Changes in the strength of synaptic connections – synaptic plasticity – are a fundamental component of learning and memory, higher order thinking, and neuronal growth and development. Aberrant plasticity has been implicated in drug addiction (Jones and Bonci, 2005; Luscher and Malenka, 2011). There are several types of synaptic plasticity such as homeostatic and Hebbian plasticity. iGluRs play a prominent role in all forms of plasticity, though the most common forms of Hebbian plasticity are NMDAR-dependent (Citri and Malenka, 2008). There are two general forms of Hebbian plasticity: long-term potentiation (LTP) and long-term depression (LTD): LTP is the increase in synaptic transmission due to high frequency stimulation (HFS) while LTD is the reduction in synaptic transmission due to low frequency stimulation (LFS) (Figure 1.3 B & C). Both forms of plasticity persist for days to weeks.

Hebbian plasticity postulates that functionally coupled neurons can modulate the excitability of one another (Hebb, 1949). For this to occur, the neurons must have coincident activation – simultaneous pre- and post-synaptic activity. The primary molecular coincidence detector is the NMDAR. Presynaptic depolarization results in glutamate release, which could activate NMDARs. However, NMDARs are blocked by magnesium at resting membrane potentials (Mayer et al., 1984; Nowak et al., 1984). Magnesium block is strongly voltage dependent being relieved by depolarization. A strong postsynaptic depolarizing signal, such as AMPAR activation or back-propagating action potentials, would unblock NMDARs, allowing calcium influx. As such, a robust NMDAR-current serves as a molecular indicator of presynaptic depolarization (which led to glutamate release) and postsynaptic depolarization (which led to magnesium unblock).

Plasticity occurs in two phases – induction phase and maintenance phase. NMDARs play a central role during the induction phase of plasticity as LTP can be blocked by the presence of APV, a selective NMDAR antagonist (Collingridge et al., 1983; Harris et al., 1984; Mulkey and Malenka, 1992). It is the influx of calcium through open NDMARs that is vital to plasticity as calcium chelators block LTP and LTD (Malenka et al., 1988; Brocher et al., 1992). As such, functional NMDARs and calcium influx are critically involved in inducing plasticity.

The magnitude and time course of postsynaptic calcium determines the form of Hebbian plasticity. In LTP, calcium is present briefly but at a relatively high concentration while in LTD, calcium is present for a relatively longer duration but at a lower concentration. The varied calcium transients activate different molecular pathways: LTP involves activation of calmodulin-dependent kinase II (CaMK-II) while LTD involves activation of calcineurin. In LTP, the cumulative effect is increased trafficking of AMPARs and increased conduction through AMPARs while in LTD there is a net reduction in synaptic AMPARs (Soderling and Derkach, 2000; Citri and Malenka, 2008; Kristensen et al., 2011). Therefore, Hebbian plasticity both begins and ends with iGluRs.

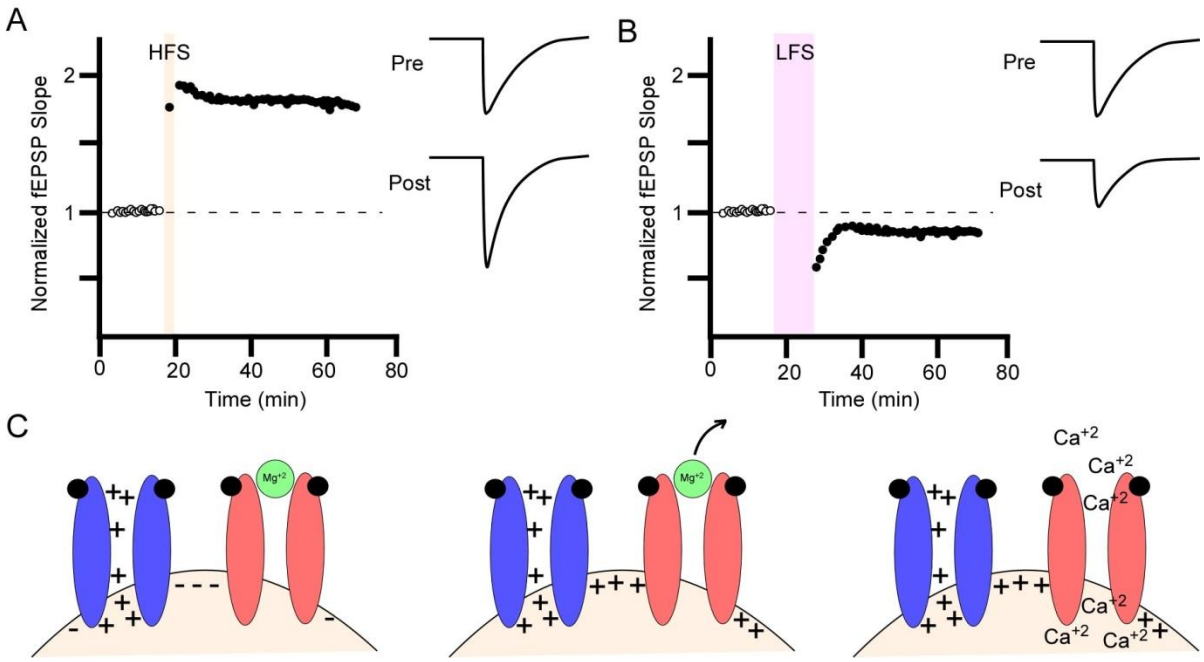

Figure 1.3 Mechanisms of NMDAR-dependent synaptic plasticity

(A & B) Example LTP (A) and LTD (B) experiments. HFS and LFS represent high frequency stimulation and low frequency stimulation, respectively. Adapted from (Citri and Malenka, 2008).

(C) Cartoon model of postsynaptic AMPAR (*blue*) and NMDAR (*red*) activation. Binding of glutamate (*black circles*) drives both channels into the open configuration but NMDARs at resting membrane potential (~ -70 mV) will be blocked by external magnesium (*left*). The local depolarization caused by currents flowing through the AMPAR will induce magnesium unblock (*middle*). The now unblocked pore of NMDARs will allow for the influx of calcium (*right*).

Pathophysiology of NMDARs

NMDAR dysfunction has been implicated in numerous diseases including acute and chronic neurodegenerative disorders such as stroke and Parkinson's Disease, respectively (Benarroch, 2011). Further, psychiatric disorders such as schizophrenia also involve NMDAR dysfunction. Recently, numerous *de novo* mutations in NMDARs (Table 1.2) have been associated with various epileptic and developmental disorders.

NMDAR hyperfunction in acute and chronic neurodegeneration

NMDAR-mediated excitotoxicity has been implicated in several acute and chronic neurodegenerative disorders. Under pathological conditions, excess glutamate overstimulates NMDARs, which leads to high levels of intracellular calcium (Olney et al., 1972; Choi et al., 1988; Villmann and Becker, 2007). Excess calcium triggers numerous apoptotic and necrotic pathways. Therefore, the over-excitation of NMDARs effectively leads to neuronal cell death (Hardingham and Bading, 2010).

In the case of ischemia or stroke, normal blood flow throughout nervous tissue is reduced, largely due to cerebrovascular occlusion. Clinically, ischemic insults have a rapid onset (minutes to hours) and patient presentation often involves, but is not limited to, agnosia, apraxia, unilateral weakness, aphasia/dysphasia, facial droop, confusion, and cognitive deficits. These symptoms are generally contralateral to the lesion.

During an ischemic attack, there is reduced influx of nutrients and oxygen as well as limited metabolic waste removal. Inadequate influx leads to neuronal death and necrosis, manifesting as a relatively small, focal lesion. However, the subsequent pathogenesis, driven by NMDAR-mediated excitoxicity, leads to rapid neuronal degeneration. The NMDAR mediated excitotoxicity is due to a combination of glutamate dumping from necrotic cells, potassium

driven depolarization, and excess neurotransmitter release/reduced neurotransmitter clearance (Benveniste et al., 1984). Under these conditions, activation of extrasynaptic GluN2B containing NMDARs drives apoptosis through multiple secondary pathways (Hardingham and Bading, 2010; Paoletti et al., 2013). For example, extrasynaptic GluN2B-containing NMDARs complex with proteins such as death-associated protein kinase 1 (DAPK1). DAPK1 potentiates NMDAR currents and activates downstream apoptotic and necrotic enzymes (Tu et al., 2010).

NMDAR antagonists have shown promising results in animal models of ischemia (Lai et al., 2011; Bach et al., 2012). However, first generation antagonists often failed during clinical trials because of issues related to delivery. Further, these pharmacological agents were non-specific NMDAR antagonists, which caused intolerable side effects (Lai et al., 2011). Recent efforts, therefore, are aimed towards specifically targeting GluN2 subunits as well as intracellular scaffolding structures (Bach et al., 2012; Paoletti et al., 2013). For example, recent developments have been made in targeting the CTD region of the GluN2B subunit, though intracellular delivery remains a substantial hurdle for treatment (Martel et al., 2012).

Similar excitotoxic mechanisms have been implicated in chronic neurodegenerative disorders, such as Parkinson's Disease (PD). The main cause of PD symptoms is an iGluR mediated degeneration of dopaminergic neurons in the substantia nigra pars compacta (Standaert et al., 1994; Christoffersen and Meltzer, 1995). While dopaminergic activity decreases in PD, there tends to be hyperexcitability of glutamatergic signaling as evidenced in rat models of PD (Sgambato-Faure and Cenci, 2012). PD generally occurs in the elderly population and is a slowly progressing disorder, which primarily involves several motor deficits including moderate to severe tremor, rigidity, and shuffling gait. The majority of cases are diagnosed clinically but patients generally appear symptomatic very late in disease progression. Thus, there is a serious

hurdle regarding prediction as well as treatment of PD. The majority of PD cases are idiopathic in origin and as such, the primary etiology of PD is unknown.

Dopamine replacement therapy, in the form of L-DOPA, has been successful in ameliorating PD symptoms but is unable to reverse the pathology. To that end, memantine, a broad scale NMDAR antagonist, has been used to treat PD although, the clinical outcomes were relatively mild (Paoletti et al., 2013). Subunit-specific therapeutics are currently being developed, with promising results shown with GluN2A specific modulators (Gardoni et al., 2012). As with ischemia, concerns of delivery, side-effects, and specificity are also important factors in PD.

NMDAR de novo point mutations in epilepsy and learning disorders

Recently, a series of longitudinal genetic screens of patients with specific forms of epilepsy and learning disabilities found that many contained point mutations in different NMDAR subunits (Tables 1.2 & 1.3) (Hamdan et al., 2011; Lemke et al., 2013; Lemke et al., 2014). For example, patients diagnosed with benign epilepsy with centrotemporal spikes (BECTS) had mutations in extracellular, transmembrane, and intracellular domains (Lemke et al., 2013). Some of the mutant NMDARs tested showed altered biophysical and pharmacological properties, but the majority are yet to be explored. Interestingly, a specific *de novo* missense mutation in the GRIN2A gene (encoding GluN2A subunits) was found in patients with early onset epileptic encephalopathy. This mutation caused a robust increase in channel activity as well as a prominent reduction in magnesium block (Yuan et al., 2014). This agrees with current models of epilepsy, which implicate hyperexcitability in NMDARs as a contributing factor (Ghasemi and Schachter, 2011). As such, advanced genetic screening can detect these mutations and carries great predictive and preventative power.

Domain	Mutation	Clinical Phenotype	Features	Citation
ATD	P12T/X	BECTS	Stop Codon	d
	P60R	CSWS		d
	T122M	APBE		d
	F164I	BECTS		d
	W179X	ABPE	Stop Codon	d
	I165S	CSWS		e
	Q199X	febrile and focal seizures, MR		a
	C212Y	LKS		e
	A224V	BECTS	Zn disinhibition, increase in P_o	d
	A271V	BECTS		d
	G276S	ARE		e
	L315X	CSWS	Stop Codon	d
	R351W	BECTS		d
ATD-S1	C417R	ABPE		d
S1	G464R	CSWS, ARE, dysphasia		e
	R485W	LKS		e
	R499H	CSWS, ARE, verbal dyspraxia	Decreased MCT, increased MOT	e
	V510W/X	BECTS	Stop Codon	d
	T512M	CSWS, epilepsy aphasia disorder	Increased MOT	c
S1-M1	S528del	APBE/CSWS	Truncation	d
S1-M1	A529T	LKS		e
M1-M2	R567K			a
M2	N596K	severe MR, seizures, myoclonies	Decreased Mg^{+2} block and Ca^{+2} permeability	a
M3	F633V	CSWS	Decreased MCT, increased MOT	e
S2	K650N	CSWS		e
	R662X	LKS	Stop Codon	d
	I675T	LKS		e
	P680S	BECTS		d
	M686S	BECTS		d
	E695K	CSWS		d
	A697T	ARE, verbal dyspraxia		e
	A708T	BECTS		d
	D712N	ARE, verbal dyspraxia		e
	V715L	BECTS		d
	L760X	CSWS	Stop Codon	d
M4	I795T	BECTS		d
CTD	I885F	BECTS		d
	D914N	LKS		e
	Y924X	CSWS	Stop Codon	d
	V948L	BECTS		d

N957S	CSWS/APBE		d
T1045A	BECTS		d
N1057K	BECTS/LKS		d
D1232N	ARE		e
A1257G	BECTS, CSWS		d
Y1368X	CSWS	Stop Codon	e
A968T	Autism		b

Table 1.2 Point mutations in the GluN2A subunit (*GRIN2A* gene) linked to epilepsy and learning disability

Note that most of the mutations have not been tested and as such, there are no attributable functional features.

APBE – Atypical Benign Partial Epilepsy
ARE - Atypical Rolandic Epilepsy
BECTS – Benign epilepsy with centrotemporal spikes
CSWS – Epileptic encephalopathy with continuous spike and wave during sleep
LKS – Landau-Kleffner syndrome
MR – Mental retardation

Citations:
a - (Endele et al., 2010)
b - (Tarabeux et al., 2011)
c - (Carvill et al., 2013)
d - (Lemke et al., 2013)
e - (Lesca et al., 2013)

Domain	Mutation	Clinical Phenotype	Functional Phenotype	Source
S1-M1	S542+1S	Severe intellectual disability, partial complex epilepsy, hypotonia	low agonist activated currents	A
M3-S2	E643K	moderate intellectual disability	Increased Ba^{+2} influx.	A

Table 1.3 Mutations in GluN1 subunit linked to epilepsy and learning disability

Citations:
A - (Hamdan et al., 2011)

Structure and Dynamics of iGluRs

iGluR subunits are composed of four modular domains: the extracellularly located amino-terminal (ATD) and ligand binding domains (LBD), the pore-forming transmembrane domain (TMD), and the intracellular carboxy-terminal domain (CTD) (Traynelis et al., 2010). Each of these domains is tethered to each other via short polypeptide linkers. In 2009, the near full-length AMPA homomeric structure in the antagonist bound closed state was solved (Figures 1.4 & 1.5) (Sobolevsky et al., 2009). One of the major highlights of the structure is that it revealed the tertiary orientation between different domains and subunits. The receptor shows variable symmetry and organization at the different domain layers (ATD, LBD, and TMD). At the ATD and LBD layers, there is a two-fold degree of symmetry yet at the level of the TMD, the receptor has four-fold symmetry (Figure 1.4, *right*). The functional implications of this symmetry-mismatch are currently unknown.

The ATD is a bilobed structure with multiple ligand binding sites that contributes to the functional and heteromerization properties of iGluRs (Hansen et al., 2010; Lee and Gouaux, 2011). The ATD is. In NMDARs, the ATD directly influences subunit-specific gating properties including open probability and subconductance states (Gielen et al., 2009). The ATD is also a binding site for numerous endogenous biochemical and pharmacological agents. For example, the ATD binds zinc, which is a vital synaptic regulator of NMDAR channel opening (Christine and Choi, 1990; Williams, 2001; Huggins and Grant, 2005; Erreger and Traynelis, 2008). Further, mutations in the ATD that reduce zinc efficacy are associated with epileptic disorders (Lemke et al., 2013) . Several modulatory drugs bind to the ATD and alter channel opening (Karakas et al., 2009, 2011; Furukawa, 2012).

The LBD is the site of ligand binding for full agonists, partial agonists, and competitive antagonists. iGluR LBDs are formed by two polypeptide stretches, referred to as S1 and S2, which form two tertiary lobes, labeled D1 and D2 (Armstrong and Gouaux, 2000; Furukawa and Gouaux, 2003; Furukawa et al., 2005). The D1 and D2 lobes are oriented in a clamshell-like configuration and ligand binding leads to "closure" of the clamshell (Figure 1.4 & 1.5) (Armstrong and Gouaux, 2000; Sobolevsky et al., 2009). LBD pairs orient as dimers and the dimer interface is a critical component of AMPAR desensitization (Armstrong and Gouaux, 2000; Sun et al., 2002; Weston et al., 2006).

The TMD forms the ion channel. It consists of three transmembrane helices (M1, M3, and M4) and a re-entrant pore-loop (M2). The ion channel core (M1-M3) of iGluRs is homologous to that of potassium channels (Panchenko et al., 2001; Wollmuth and Sobolevsky, 2004). However, the ion channel core of iGluRs sits with an inverted topology compared to potassium channels, as the pore loop is located along the intracellular end of the TMD (Kuner et al., 2003). Compared with the M3 helix, which lines the ion channel pore, the M1 and M4 helices are more peripheral to the central ion channel. Elements of these peripheral elements have been shown to impact channel function but there is little understanding of their role during pore opening (Ren et al., 2012; Ogden and Traynelis, 2013). The M4 helix, however, is a necessary AMPAR tetramerization element, although it is not required in prokaryotic forms of iGluRs (Chen et al., 1999; Salussolia et al., 2011b).

The LBD is connected to the TMD by three distinct polypeptide linkers referred to as S1-M1, M3-S2, and S2-M4. While the M3-S2 is a disordered stretch of peptide, the S1-M1 and S2-M4 linkers have small helical elements known as the pre-M1 and pre-M4 helices, respectively. Mutations in the linkers alter activation and desensitization, suggesting that they play an

important role in channel opening (Krupp et al., 1996; Villarroel et al., 1998; Yelshansky et al., 2004). Recently, subunit-specific allosteric inhibitors were shown to bind to the linker region, suggesting that this is another region of the protein that can be targeted to treat disease (Hansen and Traynelis, 2011).

Structural Components of the Permeation Pathway

The pore is formed by the M2 reentrant loop and the extracellular end of the M3 helix. The M2 loop forms the selectivity filter and is involved in magnesium block and calcium permeability (Wollmuth et al., 1996; Wollmuth et al., 1998a, b; Kuner et al., 2001). The M3 helix is homologous to the M2 helix of potassium channels and as such forms the helical bundle-crossing that restricts ion flux. The extracellular half of M3 also contains elements, which influence ion permeation as well as gating. For example, a motif in the GluN1 M3 helix (D_{640}RPEER motif) has been implicated in calcium influx through NMDARs (Watanabe et al., 2002). Further, the extracellular end of M3 contains a highly conserved motif, known as SYTANLAAF, which forms portions of the activation gate. This stretch of peptide is critical to channel opening as mutations within it produces constitutively active iGluRs (Zuo et al., 1997; Jones et al., 2002; Kuner et al., 2003; Chang and Kuo, 2008).

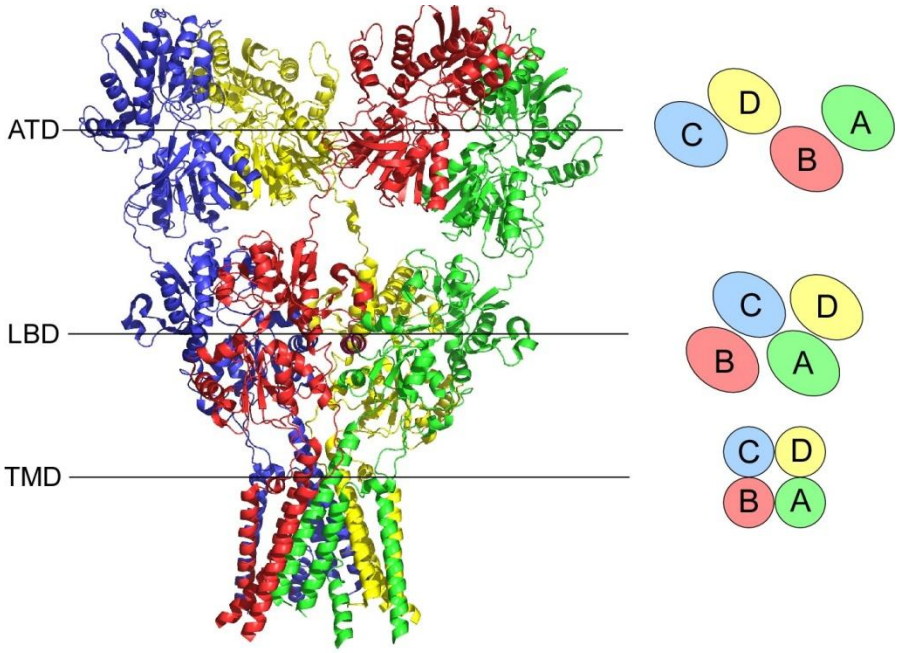

Figure 1.4 Architecture of an AMPA Receptor

Crystal structure of a single GluA2 tetrameric complex. The intracellular carboxy-terminal domain (CTD) was removed. Subunits are colored distinctly according to conformation (A/C subunits in green and blue; B/D in red and yellow). Subunits of a like conformation (A/C or B/D) are positioned across from each other. PDB ID: 3KG2 (Sobolevsky et al., 2009).

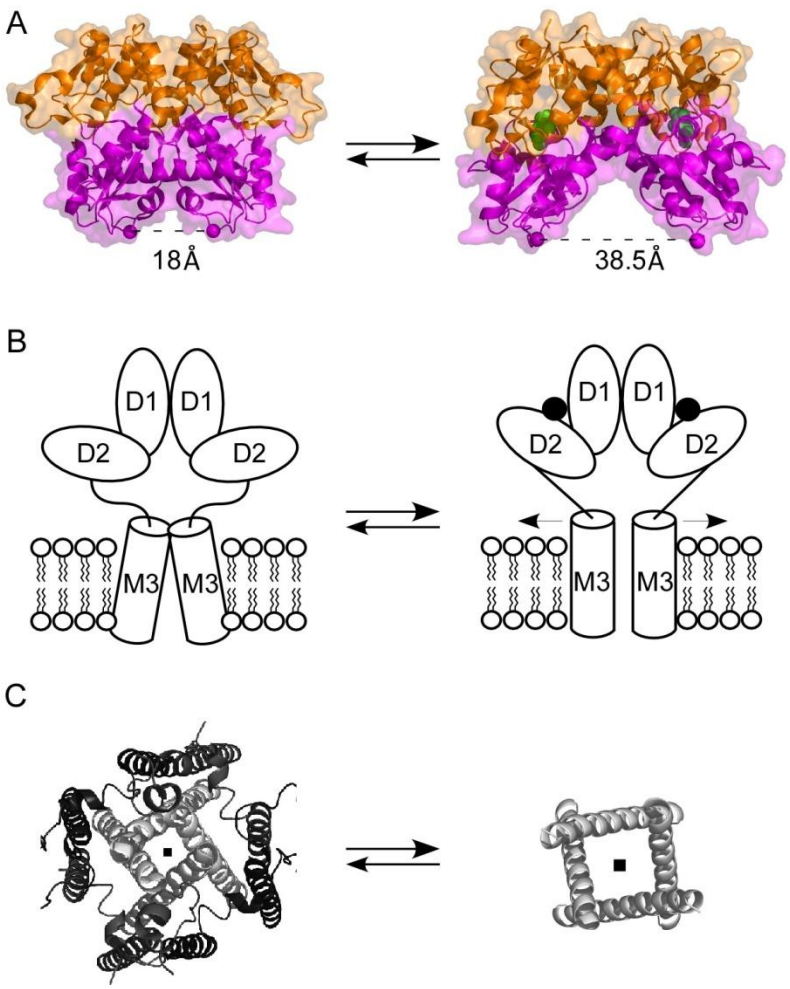

Figure 1.5 iGluR Gating Model

(A) Structure of the apo (*left*, PDB ID: 1FT0) and glutamate bound (*right*, PDB ID: 1FTJ) LBD from GluA2. D1 lobe is orange, D2 lobe is magenta. Also indicated is the distance between residue Pro632. Only two subunits are shown for clarity
(B) After agonist binding, the D2 lobe is hypothesized to shift upwards in a clamshell closure like movement. This is then thought to transfer to the TMD and cause the M3 helices to separate. Only two subunits are shown for clarity.
(C) *Left*, a top-down view of the transmembrane domain (helices M1, M3, & M4) in the antagonist-bound (channel pore closed) GluA2 structure (PDB ID 3KG2) (Sobolevsky et al., 2009). The M3 helices (light gray) directly line the ion channel pore (square indicates central axis of the pore). *Right*, open-channel structure of Shaker Kv1.2 (2A79) (Long et al., 2005), the TM2 helices.

Mechanisms of pore opening

When neurotransmitter-gated ion channels are in the resting state, the ion channel is in the closed or non-conducting configuration. Upon ligand binding, the channel is driven to the open or conducting configuration. Each neurotransmitter-gated ion channel (cys-loop receptors, purinergic receptors, and iGluRs (Figure 1.6)) has distinct gating movements during pore opening as well as unique allosteric mechanisms, which link agonist binding to ion channel opening. While there are numerous models for pore opening, it generally occurs via mechanisms analogous to a swinging door or a circumferential dilation similar to iris widening (Hille, 2001). For example, in cys-loop receptors, recent crystallographic work suggests that agonist binding shifts hydrophobic side-chain orientations and transmembrane helical positions, leading to a combined door-swing and iris-like widening of the channel pore (Hilf and Dutzler, 2008, 2009; Hibbs and Gouaux, 2011). In iGluRs, the closed channel is formed by the M3 transmembrane helices of each subunit forming a bundle crossing that precludes ion flux (Chang and Kuo, 2008; Sobolevsky et al., 2009). It has been proposed that channel opening in iGluRs involves a splaying apart of the M3 helices, leading to an iris-like widening of the channel (Sobolevsky et al., 2009). This is yet to be validated as no open structure of an iGluR is currently available. Ultimately, a major shortcoming of these putative models is that they are mostly based on individual static states of the receptors.

During the transition from closed to open, the receptors undergo a series of allosteric conformational shifts between the states, for which these structures give no resolution. Two mechanisms of coupling are mechanical and biochemical coupling. In mechanical coupling, the energy from the tertiary movements of the ligand-binding site is transferred to the channel pore through rigid-body physical means such as pulling, twisting, etc. For example, in nAChRs,

agonist binding induces a quaternary twisting of the protein at the agonist binding site and an opposite rotation at the transmembrane level (Figure 1.7) (Liu et al., 2008). Similarly, in calcium-activated potassium channels, calcium binding generates pulling force through the adjoining linkers, which ultimately drives the channel into an open conformation (Niu et al., 2004). Biochemical coupling involves energy transfer in the form of altered side-chain interactions. This mechanism is thought to also be involved in nAChR gating as pore opening involves changes in several side-chain interaction networks (Lee and Sine, 2005). As such, opening of ligand-gated ion channels is a complex mechanism, potentially involving multiple allosteric components.

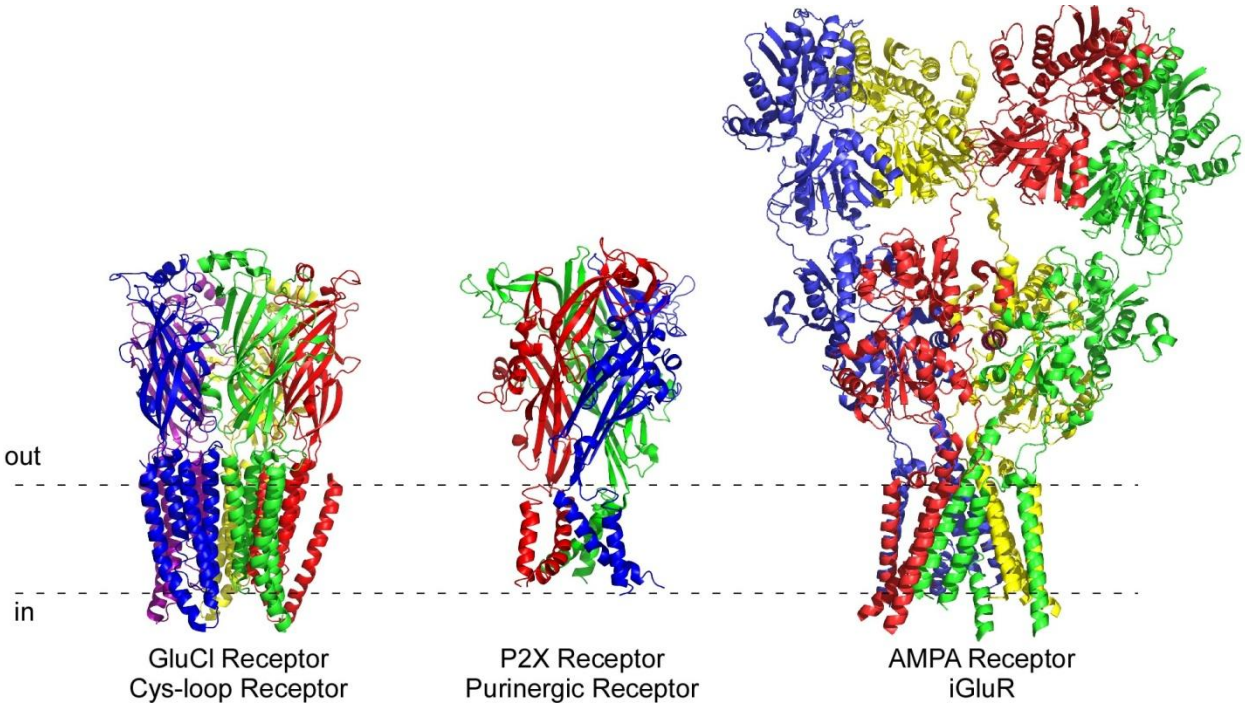

Figure 1.6 Superfamilies of neurotransmitter gated ion channels

Crystal structure representations of GluCl (PDB ID: 3RIF, (Hibbs and Gouaux, 2011)) P2X (PDB ID: 4DW0, (Hattori and Gouaux, 2012)), and AMPA (PDB ID: 3KG2, (Sobolevsky et al., 2009)) receptors.

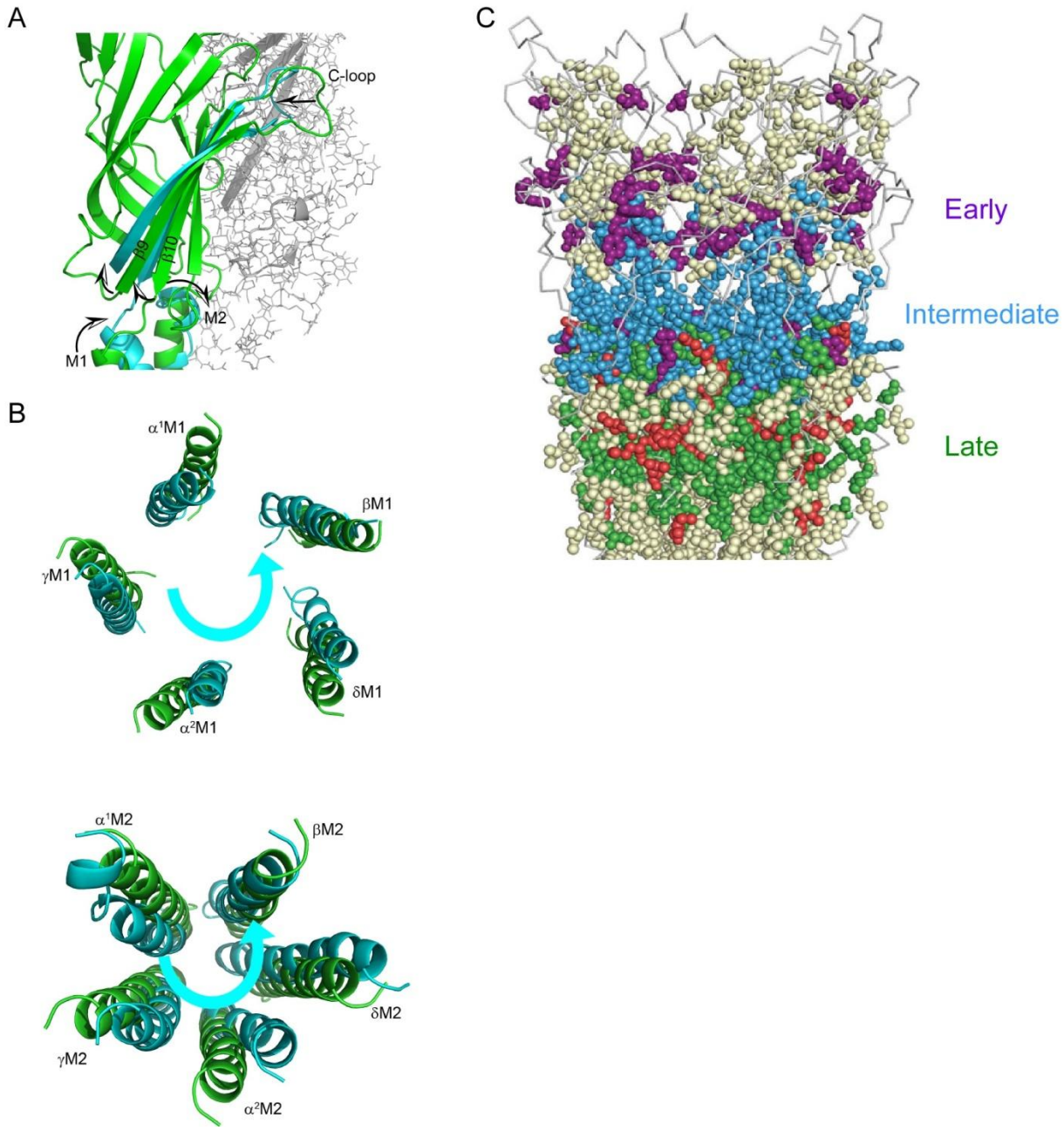

Figure 1.7 Proposed mechanisms of nAChR channel opening

(A & B) Predicted structural rearrangements at the agonist binding site **(A)** and transmembrane helices **(B)** based on molecular dynamics simulations.

(C) Functional experiments determine a relative map of structural rearrangements, which suggest that movements at the agonist binding site precede those of the transmembrane helices. A & B are recreated from (Liu et al., 2008). C is recreated from (Purohit et al., 2013).

Kinetic models of pore opening

Kinetic models are a quantitative representation of the presumed structural states the ion channel traverses during gating. Developing accurate kinetic models is essential to understanding synaptic function because the models describe, as well as predict, how synaptic function is affected by protein mutations as well as interactions with other proteins and the environment. The simplest gating model involves a ligand-gated channel in the agonist unbound, pore closed state (R), which then binds agonist (AR) , traverses through a transient agonist bound, pore closed state (C), and ultimately adopts an agonist bound, pore open state (O) (Figure 1.8A). These states will transition at a given frequency or rate. This simplified gating model is not likely to be the case for any ion channel (Hille, 2001). For example, all iGluRs enter desensitized states, which are long duration agonist bound, pore closed states. Further, the channel itself may traverse several resolvable closed and open states (Figure 1.8B). It is this unique array of states and cycling through these states, which shapes the synaptic response.

Kinetic models of iGluR opening: subunit-independent vs. concerted

Macroscopic and single-channel recordings of AMPARs indicated that when bound to glutamate, the channel will consistently adopt 3-4 discrete conductance levels (Rosenmund et al., 1998; Smith and Howe, 2000; Prieto and Wollmuth, 2010). NMDARs, however, generally adopt a single conductance level, though subconductances can arise due to different mechanisms (Siegler Retchless et al., 2012). This fundamental difference suggests that following agonist binding, these two iGluR subclasses traverse different paths toward pore opening.

The proposed gating model for AMPARs is termed “subunit-independent”. The subunit-independent model is analogous to the Koshland-Nemethy-Filmer (KNF) model, which postulates that each subunit can independently gate following agonist-driven activation. Further,

all subunits behave as independent units and there is no cooperativity. This model matches the gating mode of AMPARs as the receptor shows four distinct subconductance states. Each subconductance presumably reflects the fractional contribution to channel opening from each subunit.

The model for NMDARs is termed "concerted". The concerted gating model is analogous, though not entirely equivalent, to the Monod-Wyman-Changeux (MWC) model. The concerted model suggests that the non-conductive and fully conductive states can be adopted and that ligand-binding alters the likelihood of entering the fully conductive state (Figure 1.8). This is evident in NMDAR gating as there is only one, complete conductance state. This conductance state presumably arises as a result of the four subunits completely activating, most likely following the binding of all four agonists (Figure 1.8). A critical tenet of this model is that the transition from one conformation to the other involves an identical set of structural rearrangements and it is the rate at which these rearrangements occur that varies. Currently, there is no basis for the structural changes between the closed and open state of any iGluR.

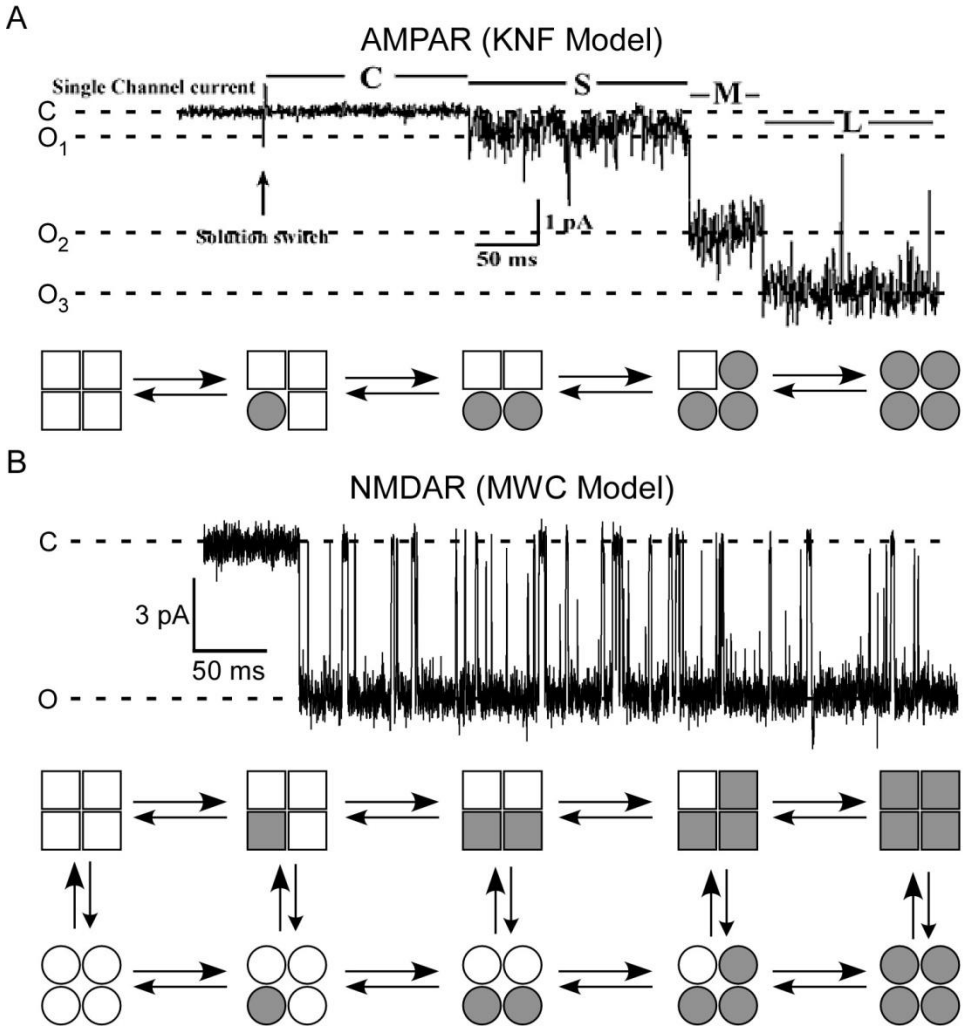

Figure 1.8 Kinetic Models of iGluR Pore Opening

(A) *Top*, AMPAR single channel activity. Dashed lines indicate (C)losed or (O)pen levels. Closed (C), Small (S), Medium (M), and large (L) conductance periods are indicated. *Bottom*, Schematic of KNF model. Squares and circles represent subunits in non-conducting and conducting conformations, representatively. Arrows are arbitrary and do not carry physical meaning. White represents agonist-unbound, gray represents agonist-bound.
(B) *Top*, Same as (A) but for NMDAR. *Bottom*, Schematic of MWC model.

Structural and kinetic mechanisms of pore opening allosterics in NMDARs

The current iGluR gating model is that clamshell closure of the LBD mechanically pulls the LBD-TMD linkers, which then forces the M3 helices apart and opens the gate (Jones et al., 2002; Chang and Kuo, 2008). Indeed, partial agonists show partial degrees of cleft closure, paralleling graded pore opening (Jin et al., 2003). Further, mutations which disrupt pore closure also deter efficient channel opening (Armstrong et al., 2003; Robert et al., 2005; Zhang et al., 2008). Nevertheless, while this model purports that the LBD is a major driver of pore opening, the mechanistic features of channel opening and LBD-TMD coupling remain unknown. As with nAChRs, allostery in iGluR opening may involve a complex mechanism of rigid-body tertiary movements as well as changes in interaction networks along a coupling pathway.

Due to their location between the LBD and the TMD, the LBD-TMD linkers must be critically involved in channel opening. Indeed, mutations and accessibility studies show that mutations in the linker alter channel opening (Yelshansky et al., 2004; Sobolevsky et al., 2007; Talukder et al., 2010). However, while the LBD-TMD linkers actively influence channel opening, it is unknown how this occurs, though it is proposed that the linkers pull upon the transmembrane helices, leading to pore opening (Armstrong and Gouaux, 2000; Hansen et al., 2007; Sobolevsky et al., 2009; Dong and Zhou, 2011). As such, my work focuses on determining the allosteric processes of NMDAR pore opening from both a kinetic and structural perspective. Specifically, I focus on how the LBD-TMD linkers are principally involved in transducing the energy of ligand binding into pore opening.

Chapter 2 is dedicated to the central mechanism of pore opening – how the LBD drives pore opening at the level of the M3 helix. The M3-S2 helix joins the LBD to the M3 helix and presumably transfers energy into pore opening. We hypothesize that, from a tertiary level, the

rigid-body movements of the LBD pulls the M3-S2 linker and the energetics of pulling drive the M3 helices into the open conformation. To address this, we combined single-molecule electrophysiological and computational tools to see how alterations of the pulling capacity of the linker modulate channel function. We find that not only is pulling required for efficient pore opening, but that the GluN2A subunit must pull more energetically than the GluN1 subunit.

Chapter 3 resolves how the peripheral elements – the M1 and M4 helices and their adjoining S1-M1 and S2-M4 linkers – reposition during opening. The M1 and M4 transmembrane helices encapsulate the central gating elements (M3 and M3-S2) of the ion channel. As such, we hypothesized that the outer elements must rearrange, specifically by splaying away from the central axis of the pore. This must occur efficiently and precede the pore opening event. To address this, we physically tethered the peripheral elements using engineered cysteines and observed the altered functionality of the channel. We find that limiting the movements of the peripheral elements robustly curtails pore opening, thus suggesting that these elements must rearrange, independent of the M3 helices, before pore opening.

Chapter 4 links the mathematical descriptions of kinetic states with structural movements during channel opening. Currently, the relationship between kinetic activity and structure is entirely speculative. However, mathematical tools have been developed to predict the temporal and dynamic nature of structural rearrangements using kinetic activity. To assay the degree of movements, we use a modified form of rate analysis to quantify the magnitude of residue movement during a given state transition. We then extend this analysis to perform a rate equilibrium free energy relationship (REFER) analysis to determine the relative timing of residue movements. We apply this approach to residues along the M3-S2 linker to speculate upon the movements of residues during pore opening and defining allostery.

CHAPTER 2: MECHANICAL COUPLING MAINTAINS THE FIDELITY OF NMDA RECEPTOR-MEDIATED CURRENTS

INTRODUCTION

Rapid chemical signaling between cells in the nervous system requires a close temporal connection between the release of neurotransmitter and the activation of the neurotransmitter-gated receptor. To facilitate the efficiency of signaling, fast chemical synapses typically employ neurotransmitter-gated ion channels. These protein complexes contain both the neurotransmitter binding site and the ion channel that mediates the cellular response, thereby facilitating the conversion of transient neurotransmitter into an efficient signal. In all neurotransmitter-gated ion channels, including cys-loop(Miyazawa et al., 2003; Dacosta and Baenziger, 2013), purinergic(Hattori and Gouaux, 2012), and ionotropic glutamate receptors(Sobolevsky et al., 2009; Traynelis et al., 2010), the neurotransmitter binding site and the transmembrane domain harboring the ion channel are spatially remote, requiring the conformational changes occurring at the transmitter binding site to be tightly linked to those occurring in the ion channel, culminating in pore opening.

NMDARs mediate plasticity in the nervous system by converting neuronal activity into changes in synaptic strength and connectivity(Citri and Malenka, 2008). These receptors efficiently integrate transient glutamate into a prolonged response. To address the coupling mechanism between the LBD and ion channel in NMDARs, we focused on a short polypeptide linker between the S2 segment of the LBD and the M3 transmembrane helix, the M3-S2 linker. In iGluRs, the M3 transmembrane helix, homologous to the TM2 or S6 segment in K^+ channels(Wo and Oswald, 1995; Wood et al., 1995; Sobolevsky et al., 2009), is the main pore-forming segment and presumably contains elements that preclude ion flux in the closed

state(Chang and Kuo, 2008; Sobolevsky et al., 2009). Using single molecule electrophysiological and computational approaches, we provide direct evidence that mechanical pulling is a significant component of NMDAR activation. The importance of this mechanism is highlighted by results showing that a single residue insertion in the M3-S2 linker nearly abolishes the ability of NMDARs to convert transient glutamate into a functional response. Further, NMDARs are obligate heterotetramers containing two glycine-binding GluN1 subunits and typically two glutamate-binding GluN2 subunits. We find that for robust pore opening to occur, the GluN2A subunits must transfer more energy and at an earlier time point than the GluN1 subunits. Therefore, NMDARs require mechanical coupling to efficiently convert transient glutamate into prolonged pore opening, a central feature of NMDARs in synaptic dynamics.

MATERIALS AND METHODS

Mutagenesis and heterologous expression. Mutations were made in rat GluN1a (NCBI Protein database accession no. P35439) or GluN2A (accession no. Q00959) via QuickChange site-directed mutagenesis (Stratagene, La Jolla, CA.) (Kazi et al., 2013). GluN1 and GluN2A cDNA constructs were cotransfected into mammalian human embryonic kidney 293 (HEK 293) cells along with a separate pEGFP-Cl vector at a ratio of 1:1:1 using X-tremeGene 9 (Roche). To improve cell survivability, transfected cells were bathed in media containing the GluN2A competitive antagonist DL-2-amino-5-phosphonopentanoic acid (APV; 100 μM) and magnesium (100 μM). All experiments were performed 12-48 hours post-transfection.

Single channel recordings. Single channel currents were recorded at room temperature using an integrating patch clamp amplifier (Axopatch 200B; Molecular Devices), analog filtered at 10 kHz (four-pole Bessel filter), and digitized between 25 and 50 kHz (ITC-16 interfaced with PatchMaster, HEKA). Our standard bath solution consisted of 150 mM NaCl, 2.5 mM KCl, and 10 mM HEPES (pH 8.0, NaOH). Patch pipettes (thick-wall, borosilicate, Sutter Instruments) were pulled and fire-polished achieving resistances between 3 and 30 MΩ when measured in the bath. For outside-out recordings, patch pipettes were filled with 140 mM KCl, 1 mM BAPTA, and 10 mM HEPES (pH 7.2, NaOH). At -100 mV, seal resistance ranged between 1 and 20 GΩ. Agonists were applied via a piezo driven double-barrel application pipette system with a 10%-90% rise time of 250-500 μs. For cell-attached recordings, patch pipettes were filled with the standard bath solution as well as 1 mM glutamate and 0.1 mM glycine. 1 mM EDTA was added to minimize gating effects of divalents (Popescu and Auerbach, 2003; Schorge et al., 2005; Traynelis et al., 2010). Inward currents were elicited by applying a pipette potential of +100 mV.

For outside-out patches, we used two different protocols: either a brief (2 ms, Fig. 2.1) or a long (1 s, Fig. 2.2) application. Different patches were used for the different protocols. For the brief protocol, the baseline barrel contained 150 mM NaCl, 2.5 mM KCl, 0.1 mM glycine, 0.02 mM EDTA, 0.5 mM $CaCl_2$, and 10 mM HEPES (pH 7.3, NaOH) while the test barrel contained the same solution with added 1 mM glutamate. This solution approximates a physiological extracellular solution with minimized zinc(Erreger et al., 2005a). Patches were held at -70 mV. Glutamate was applied for 2 ms every 4 seconds. After 25-50 consecutive brief applications, glutamate was applied for 1 s approximately 5-10 times to test whether activity arose from a single channel. For GluN1/GluN2A, which has a high open probability (~0.7), no analyzed patches contained more than one channel. For the insertion constructs, which have a much lower open probability, it was difficult to ensure that activity was only from one channel. Nevertheless, we estimate that most recordings showed activity from 1, and at most 2, channels. The 2 ms and 1 s protocols were alternated until activity was no longer detectable.

For the long protocol (Fig. 2.2), the baseline barrel contained 150 mM NaCl, 2.5 mM KCl, 0.1 mM glycine, 1 mM EDTA, and 10 mM HEPES (pH 8.0, NaOH) while the test barrel contained the same solution with added 1 mM glutamate. Patches were held at -100 mV. Glutamate was applied for 1 s and pulses were delivered every 3 seconds to allow for recovery from desensitization. Because of the greater number of events collected for these experiments, we are more confident that patches contained a single channel.

Summation of channel activity from brief applications. For the brief application recordings, the lowest number of consecutive applications was 25. Numerous patches contained more than 25 consecutive applications, but to avoid bias, we analyzed these data in sets of 25 consecutive applications. Briefly, each patch was divided into separate sets of 25 consecutive applications. A

set of 25 consecutive applications, which contained failures, was summed. The resultant summed current for each set was then averaged with the summed currents of the other sets of 25 current applications for that patch. For example, if there were 100 total applications recorded from a single patch, the currents from applications 1 through 25 would be summed and count as a single set. This would be repeated for each subsequent set of 25 applications resulting in 4 sets. The 4 sets for this patch would be averaged. The resulting averaged current, referred to as the summed current profile, for each patch was used for statistical analysis. Explicitly, the number of patches, applications, and sets were: GluN1/GluN2A: 5 patches, 250 applications, and 10 sets; GluN1(G648+1G)/GluN2A: 3 patches, 725 applications, and 29 sets; and GluN1/GluN2A(G645+1G): 2 patches, 475 applications, and 19 sets. The average summed currents for each patch were analyzed for peak amplitude and charge transfer. Charge transfer was the total charge integral following agonist application.

Single channel analysis from long applications. For long applications (1 s), the number of applications per patch ranged from 20-180. Briefly, data was exported from PatchMaster to QuB (http://www.qub.buffalo.edu) for analysis. Applications displaying significant amounts of noise were removed (~5-10% of applications). After data processing, the segmental k-means (SKM) algorithm was run to idealize the data (with a dead time of 0.020 ms) using a two state model (1 closed, 1 open) (Qin et al., 2000a). The idealized data was then manually scanned to remove false events.

Failure to open. In some instances, agonist application showed no discernible NMDAR mediated currents either during or after the removal of glutamate(Gibb and Colquhoun, 1992; Erreger et al., 2005a). These instances are referred to as failures. % failures were calculated as:

Eq. 2.1

$$\%\ Failure = 100 * (\#\ failures\ \ \#\ total\ applications)$$

Latency to 1st opening. Durations from the start of an application to the first idealized open event were reported. We further manually checked each pulse to ensure that latencies reported were to properly idealized events (as opposed to misclassified events).

Latency to 1st opening times were pooled and imported into ChanneLab2 (Synaptosoft). The latencies were binned at ~ 60 μs intervals and histograms displaying number of events as a function of latency to 1st opening were generated. The cumulative histogram was fit by multiple exponential functions. Exponential components were added until the log likelihood could not be further improved. All constructs were best fit by 2 components as the addition of a 3rd component did not improve the log likelihood value.

Channel open time. To characterize the effect of insertions on the amount of time channels spent in the open state, we calculated the average open time. For each application with activity, the total open time was calculated from the idealization tool in QuB. These values were averaged for a given patch to yield the average open time. This value reflects the average amount of time the channel spends in the open state for an individual patch and was used for further statistical analyses. Note that the average open time is distinct from mean open time, which is the average amount of time the channel spends in the open state for a single opening event.

Secondary structure prediction and homology modeling. Insertions and deletion are presumed to alter the length of the M3-S2 linker. Alternatively, these manipulations may significantly perturb local secondary structures. We used two general approaches to test for the structural effects induced by our manipulations: homology modeling using servers (PHYRE/SWISS-MODEL) (Bordoli et al., 2009; Kelley and Sternberg, 2009) and homology modeling using MODELLER (Sali and Blundell, 1993). The modeling servers provide a unique advantage because they incorporate secondary structure prediction (PSI-PRED, SSPro, JNet, and

Disopred) in the modeling algorithm (Kelley and Sternberg, 2009). Models of the insertion constructs were overlaid with wild type models to qualitatively detect secondary structural changes.

Computational models were based on a model structure of GluN1/GluN2A(Dai and Zhou, 2013). To insert residues into this full-length NMDAR model, we initially removed a few residues around the insertion point to create a gap in the wild type GluN1/GluN2A model and filled this gap with residues that correspond to the primary sequence of the mutated receptor. For example, for the model of GluN1(G648+1G)/GluN2A, with the insertion point between G648 and I649 in the GluN1 subunit, residues T647 and G648 were removed to create a gap; then this gap was filled in by residues T647, G648 and G648+1G. The resultant sequence became T647, G648, G648+1G, and I649. GluN2A subunits were left intact for the GluN1(G648+1G)/GluN2A model. Other insertion constructs were obtained in a similar fashion. All modeling for MD simulations was done using MODELLER(Sali and Blundell, 1993).

All-atom molecular dynamics simulations. Molecular dynamics (MD) simulations were performed for a specific subset of constructs: GluN1/GluN2A, GluN1(G648+1G)/GluN2A, GluN1(G648+4G)/GluN2A, GluN1/GluN2A(G645+1G), and GluN1/GluN2A(G645+4G). Each model was independently energy minimized in vacuum, with a fixed backbone, for 2000 steps. The receptor was then incorporated into a lipid POPC bilayer. Lipid and water molecules that overlapped with the protein were subsequently removed. Ions were added to make the salt concentration of the system equal to 150 mM NaCl. System preparations were conducted using VMD(Humphrey et al., 1996). After minimization, a simulation was run for 1 ns with protein backbone harmonically restrained at their initial positions using a 20 kcal/mol/A^2 force constant.

The targeted molecular dynamics simulation for each structure was performed similarly to what has been done for wild type receptors (Dong and Zhou, 2011; Dai and Zhou, 2013). Briefly, the root mean square deviation (RMSD) values of the C-α atoms of the LBDs in our simulations were forced to gradually decrease to zero, with respect to the agonist-bound structure of the wild type GluN1/GluN2A LBD dimer (PDB ID: 2A5T) (Furukawa et al., 2005). For WT simulations, the target LBD contains residues T378 to T419, P434 to K525 and I646 to C780 in GluN1 and N385 to S519 and V643 to C781 in GluN2A; for simulations of GluN1 insertion constructs, the target LBD contains residues T378 to T419, P434 to K525 and I649 to C780 in GluN1 while residues in GluN2A subunits remain the same as in the WT simulation; for simulations of GluN2A insertion constructs, the target LBD contains residues N385 to S519 and L646 to C781 in GluN2A while residues in GluN1 subunits remain the same as in the WT simulation.

All simulations were done using NAMD 2.9(Phillips et al., 2005). The simulation parameters for all structures were the same as those used for the simulation of the wild type receptor(Dai and Zhou, 2013). Each simulation was carried out for 65 ns using the CHARMM27 force field(Mackerell et al., 2004). During the first 20 ns, the LBD slowly transformed to the conformation of the activated state. Pore radius was calculated using the HOLE program(Smart et al., 1993). Frames which showed pore radii of < 1 Å were categorized as "pore collapsed". % pore collapse was calculated as the # pore collapse frames/total # frames. This was calculated for the last 45 ns (using 900 frames) of the simulation.

Single channel analysis for cell-attached patches. Analysis of single-channel records was comparable to(Kazi et al., 2013). Recordings of GluN1/GluN2A receptors consisted of long clusters of activity separated by seconds-long periods of inactivity, simplifying detection of

multiple channels in the patch(Popescu and Auerbach, 2003; Schorge et al., 2005). For these recordings, the relatively high open probability (P_o) and duration of recordings (~60,000-600,000 events) indicated that we were recording from single-channel patches.

For certain insertion constructs, the P_o was extremely low which made single-channel patch detection difficult. First, many patches were recorded but excluded during analysis because of obvious simultaneous openings of multiple channels. Of the remaining patches, only several minutes-long recordings without any apparent simultaneous openings were further analyzed. Of the single-channel P_o values tabulated, the lowest was 0.002 for GluN1/GluN2A(G645+4G). If the patch contained two active channels of equivalent open probability, then a double-channel opening would be expected approximately once every 500 events(Colquhoun and Hawkes, 1990b; Kazi et al., 2013). Of our records, only 4 of 103 on-cell patches showed less than 99% confidence in single channel activity.

Kinetic modeling was performed on the idealized data of an entire record. Equilibrium kinetic modeling was done using the maximum interval likelihood (MIL) algorithm (dead time of 0.024 ms). Models were built by increasing open and closed states until log-likelihood (LL) values improved by less than 10 LL units or if the next added state resulted in a state occupancy of 0%(Kussius and Popescu, 2009; Kazi et al., 2013). Kinetic models of NMDAR gating activation have been proposed to contain approximately 5 closed states and more than one open state(Banke and Traynelis, 2003; Popescu and Auerbach, 2003; Auerbach and Zhou, 2005; Schorge et al., 2005). We used a linear, fully-liganded model containing 3 closed states, 2 desensitized states, and 2 open states(Auerbach and Zhou, 2005; Kussius and Popescu, 2009; Kazi et al., 2013). Time constants and the relative areas of each component, the transition rate

constants (k_f & k_r), as well as mean closed time (MCT) and mean open time (MOT) were averaged for each construct and compared with each other.

Current simulations were performed as in(Talukder et al., 2011). Briefly, simulations were performed using QuB software using 200 channels for GluN1/GluN2A, 100 channels for GluN1(G648+1G)/GluN2A, and 100 channels for GluN1/GluN2A(G645+1G). Because the kinetic rates were calculated at equilibrium, it could not account for the failure rate of channel opening. Therefore, the difference in channel number is to account for the failure rate as approximated in Figure 2. Each channel was given a single-channel amplitude of 7.5 pA. The simulated pulse consisted of a fully liganded square pulse lasting 2 ms during a 2-s recording (250-ms prepulse). Two consecutive ligand binding steps were connected to the C_3 gating step (Fig. 2.6), with glutamate binding and unbinding constants of 1.7×10^7 M^{-1} s^{-1} and 60 s^{-1}, respectively.

Thermodynamic analysis. To define the thermodynamic impact of decoupling the LBD from the ion channel, we characterized the free energy change for each kinetic transition. We quantified the Gibbs free energy difference ($\Delta\Delta G$) between wild type and insertion constructs for each activation transition (C_3-C_2, C_2-C_1, C_1-O_1):

Eq. 2.2

$$\Delta G = -RTln(K_{eq})$$

Eq. 2.3

$$\Delta\Delta G = \Delta G_{mut} - \Delta G_{WT}$$

Statistics. Data analysis and statistics was performed using IgorPro (WaveMetrics), QuB, Excel (Microsoft), PyMol, VMD, and ChanneLab2 (Synaptosoft). Unless otherwise noted, macroscopic and microscope current amplitudes and single-channel properties are presented as mean ± SEM. We used a two-tailed Student's t-test to test significant differences between

specific properties between different constructs. Multiple comparisons were not made because we are primarily interested in whether specific properties between two specific constructs differ from one another (i.e., comparing only open probability between only GluN1/GluN2A and GluN1(G648+1G)/GluN2A), instead of trying to discern the overall difference among multiple comparisons. Unless otherwise noted, statistical significance was set at $p < 0.05$.

Unless otherwise indicated, a significant difference is indicated relative either to GluN1/GluN2A (*); to like constructs (e.g., single glycine insertions) between subunits [e.g., GluN1(G648+1G)/GluN2A versus GluN1/GluN2A(G645+1G)] ($^{\#}$); or to the single glycine insertions within subunits [e.g., GluN1(G648+1G)/GluN2A versus GluN1(G648+4G)/GluN2A] ($^{\wedge}$) ($p < 0.05$, two-tailed Student's t-test, unpaired).

RESULTS

Single glycine insertions in either GluN1 or GluN2A M3-S2 eliminates the fidelity of NMDAR-mediated synaptic currents

The glutamate transient in the synaptic cleft rises rapidly to a peak concentration of around 1 mM and then decays within several milliseconds(Clements et al., 1992). We therefore rapidly applied glutamate (1 mM for 2 ms) to outside-out patches containing a single (wild type) or no more than two (insertion constructs) NMDARs in the continual presence of glycine (Fig. 2.1a). In response to this brief glutamate application, wild type NMDARs composed of GluN1/GluN2A showed frequent activity (Fig. 2.1a$_1$). This included a brief interval between the application of glutamate and the 1st opening of the ion channel as well as persistent channel activity, generally for many tens of milliseconds(Gibb and Colquhoun, 1991; Erreger et al., 2005a). As is found for NMDAR-mediated synaptic responses, the sum of this individual activity showed a rapid rise (~5-6 ms) followed by a slower decay (~40 ms) (*lower trace*, Fig. 2.1a$_1$) (Lester et al., 1990). This profile of ion channel opening in response to transient glutamate contributes to the unique role of NMDARs to synaptic function.

The NMDAR-mediated synaptic profile is defined by the mechanism of ion channel opening following ligand binding(Lester et al., 1990). The LBD is connected to the transmembrane domain through polypeptide linkers (Fig. 2.1b). We rapidly applied glutamate to NMDARs where a single glycine residue was inserted, adjacent to an endogenous glycine, in the M3-S2 linker (Fig. 2.1c) of either the GluN1 [GluN1(G648+1G)] (Fig. 2.1a$_2$) or GluN2A [GluN2A(G645+1G)] (Fig. 2.1a$_3$) subunit. These single glycines, inserted in the pathway between the LBD and the ion channel (Figs. 2.1b,c), dramatically attenuated the transduction of the transient glutamate signal as evidenced by an increased number of applications where no

channel activity was detected (failures) and greatly truncated activity even when channels opened. Consequently, summed currents (Figs. 2.1a_2,a_3, *lowest traces*) showed peak amplitudes (Fig. 2.1d) and charge transfers (Fig. 2.1e) that were significantly reduced compared to those of wild type by about 70% for the GluN1 insertion and 90% for the GluN2A insertion. Thus, a single glycine introduced in the M3-S2 linker between the LBD and the ion channel of either GluN1 or GluN2A largely eliminates the ability of NMDARs to efficiently integrate the transient glutamate signal into a postsynaptic response.

Single glycine insertions in the M3-S2 linker reduce the likelihood and stability of channel opening

To begin addressing how a single glycine insertion in the M3-S2 linker impacts NMDAR activation, we recorded currents from outside-out patches exposed to longer pulses (1 s) of glutamate. These outside-out patches contained a single NMDAR. To maximize NMDAR activity, we transitioned to an external solution that was NaCl-based but at a higher pH (8.0) and contained high EDTA (1 mM) (see Materials and Methods).

In response to the long glutamate application, single wild type GluN1/GluN2A NMDARs were typically continually active (Fig. 2.2a_1, *upper two traces*), though certain activations were truncated (Fig. 2.2a_1, *third trace)*, and some applications showed failures (18.3 ± 1.9%, mean ± SEM, n = 6 patches, 244 applications). In contrast, NMDARs containing single glycine insertions in GluN1 (Fig. 2.2a_2) or GluN2A (Fig. 2.2a_3) showed dramatically reduced activity. In part, this arose because of a significantly increased failure rate (GluN1(G648+1G), 49.7 ± 6.6%, n = 8 patches, 297 applications; GluN2A(G645+1G), 47.1 ± 4.0%, n = 9 patches, 398 applications) (Fig. 2.2b_1) as well as a prolonged latency to 1st opening (GluN1/GluN2A, 57.7 ± 12 ms; GluN1(G648+1G), 106 ± 30 ms; & GluN2A(G645+1G), 311 ± 15.3 ms) (Fig. 2.2b_2).

However, even when channels opened, activity was significantly truncated as indexed by the average open time when channels were active during an application (GluN1/GluN2A, 358.9 ± 85 ms; GluN1(G648+1G), 54.5 ± 9 ms; & GluN2A(G645+1G), 21.8 ± 5 ms) (Fig. 2.2b_3).

The effect of single glycine insertions on opening of the ion channel in response to glutamate – the increase in failure rates and in latencies to 1st opening as well as the decrease in open time per application – could arise via three general mechanisms. (1) These manipulations could dramatically alter the efficiency of agonist binding and/or the subsequent conformational changes in the LBD. Our data suggest that glycine insertions have limited effects on LBD function (Supplementary Fig. 2.1). (2) Alternatively, the glycine insertions could promote NMDAR desensitization, but this is unlikely since wild type and glycine-inserted constructs show comparable desensitization (Fig. 2.2d). (3) Finally, insertions in the M3-S2 linker could impede the coupling mechanism between the LBD and the ion channel.

As an initial test of this latter idea, we quantified the distribution of latencies to 1st opening (Fig. 2.2c). These distributions presumably reflect the occupancy of ligand-bound closed states that precede channel opening(Pallotta, 1985). Therefore, if the coupling mechanism between the LBD and the ion channel is affected by these single glycine insertions, we would anticipate changes in these latency distributions. For wild type GluN1/GluN2A, the distribution was best fit by two exponential functions (Fig. 2.2c_1) (see Materials and Methods), which suggests that the channel traverses through multiple closed states prior to opening, consistent with proposed mechanisms of activation for NMDARs(Howe et al., 1991; Auerbach and Zhou, 2005; Erreger et al., 2005a; Schorge et al., 2005). For both single glycine insertion constructs (Figs. 2.2c_2,c_3), the distributions of latencies were again best fit by two exponentials, suggesting that the fundamental mechanism of activation of these constructs is preserved. However,

compared to GluN1/GluN2A, there were qualitative differences in the time constants and occupancies of each component (Fig. 2.2c). Indeed, both insertion constructs had increased time constants and decreased occupancy of the brief state while concomitantly increasing the occupancy of the long state. Further, these effects appeared greater for the GluN2A insertion construct than GluN1, suggesting that there may be subunit-specific differences in coupling. Thus, insertions in the M3-S2 linker primarily preclude efficient energy coupling between the LBD and the ion channel.

All-atom molecular dynamics simulations suggest that pore opening involves a mechanical coupling between the LBD and the ion channel

To elucidate the molecular basis for the role of the M3-S2 linker in coupling the energetics of the LBD to the ion channel, we carried out molecular modeling and all-atom targeted molecular dynamics (MD) simulations. One potential problem with the insertion of a residue in the M3-S2 linker is that it may induce unanticipated changes in secondary structure. We therefore used a homology model of the GluN1/GluN2A NMDAR(Dai and Zhou, 2013) (Figs. 2.3a,b, *left panels*) and introduced single glycine residues either in GluN1 (Fig. 2.3a, *center panel*) or GluN2A (Fig. 2.3b, *center panel*) M3-S2 linker (see Materials and Methods). A comparison of the M3-S2 linker between wild type and insertion construct models (Figs. 2.3a,b, *right panels*) indicates that single glycine insertions add length without altering secondary structures (see also Supplementary Figs. 2.2 & 2.3). Further, to limit introducing additional flexibility, we inserted the single glycine adjacent to an endogenous glycine (Fig. 2.1c). Thus, the main structural effect of the single glycine insertion, at least in a putative closed state, is to add length to the M3-S2 linker.

We then performed targeted MD simulations of these modeled tetrameric NMDARs to address how glycine insertions affect the transition to an activated state (see Materials and Methods). In these simulations, the LBD was targeted to the agonist bound conformation(Furukawa et al., 2005; Dai and Zhou, 2013) and then changes at the pore-lining M3 helices were monitored. For wild type GluN1/GluN2A, the M3 helices splay apart and are distant from the central-pore axis by the end of the simulations, due to the upward deflection of the lower lobe of the agonist-bound LBD pulls on the M3 helices through the M3-S2 linkers(Jin et al., 2003; Dong and Zhou, 2011; Dai and Zhou, 2013). The GluN2A subunit showed larger displacements of the M3 helix (Fig. 2.3c_1) (Dai and Zhou, 2013). These displacements presumably reflect the structural dynamics during activation of NMDARs, though the end-state of these simulations is unlikely to be the open state.

In the single glycine insertion constructs, the activated LBD also displaced the M3 helices (Figs 2.3c_2,c_3) but the extent was limited (Fig. 2.3d). Further, compared to GluN1/GluN2A, the pore was more likely to stay in the resting conformation ($\leq$ 1 Å pore radius) for the insertion constructs (Fig. 2.3e). All of these effects were more dramatic for the GluN2A insertion construct. Overall, these results suggest that, along the pathway to opening of the ion channel, the M3-S2 linker transduces the energetics of the LBD to pore-opening via a mechanical pulling mechanism, and a glycine insertion reduces the efficiency of the transduction, more so in the GluN2A subunit than in the GluN1 subunit.

Single residue insertions in the M3-S2 linkers reduce pore opening

If channel opening involves a mechanical pulling process, then insertions at different points between the LBD and M3 helix should reduce coupling, and thus pore opening. We therefore inserted individual glycine residues at different positions in the M3-S2 linker in either GluN1

(Fig. 2.4b$_1$) or GluN2A (Fig. 2.4c$_1$). For these and subsequent experiments, we recorded single-channel activity using the cell-attached configuration because it provides longer term recordings with low noise, simplifying detection of patches with a single channel, especially for constructs with low open probabilities. Further, recording large numbers of events allows for more accurate kinetic modeling of NMDAR activation(Popescu and Auerbach, 2003; Schorge et al., 2005)

At steady state, wild type GluN1/GluN2A NMDARs have an equilibrium open probability (P_o) of 0.67 ± 0.05 (n = 8 patches) (Fig. 2.4a, Table 2.1) (Popescu and Auerbach, 2003; Erreger et al., 2005a; Schorge et al., 2005). Not unexpectedly, the single glycine insertion constructs previously tested (Figs. 2.1-2.3) reduced P_o significantly to 0.36 ± 0.06 (n = 8) for GluN1(G648+1G) (Fig. 2.4b$_3$) and even more dramatically to 0.08 ± 0.02 (n = 6) for GluN2A(G645+1G) (Fig. 2.4c$_3$). Glycines inserted at more membrane-proximal positions in the M3-S2 linker in GluN1 (Fig. 2.4b) or GluN2A (Fig. 2.4c) also significantly reduced P_o. For GluN1, the reduction in P_o for the different positions was indistinguishable, whereas for GluN2A, the reduction for the membrane-proximal positions was significantly greater than that of the membrane-distal position (Fig. 2.4c, inset) (Supplementary Table 2.1). Thus, insertions in the M3-S2 linker at different points caused reductions in P_o, consistent with mechanical coupling between ligand binding and pore opening.

We initially used glycine insertions to test coupling because their absence of a side chain should prevent the introduction of new local interactions. Further, we inserted a glycine at a site where an endogenous glycine was already present (Fig. 2.1c), which should limit artificially introducing flexibility into the linker. Still, if pulling is important to pore opening, then insertions of different types of amino acids should, at minimum, reduce P_o. Indeed, like the glycine insertions, insertion of alanine or serine at GluN1(G648) or GluN2A(G645) (Supplementary

Table 2.2) strongly reduced P_o. In fact, the reduction was greater than that observed for the glycine insertions. We do not know the basis for this additional reduction in gating but it may reflect unanticipated changes in local interactions. Overall, these results are consistent with the hypothesis that mechanical pulling is a significant component of pore opening in NMDARs.

Additional insertions in GluN1 or GluN2A further reduce pore opening

If pore opening is largely driven by mechanical pulling, additional insertions, which presumably make the M3-S2 linker longer, should further curtail pore opening. We therefore inserted multiple consecutive glycines (+2G and +4G) at GluN1(G648) (Fig. 2.5a_1) or GluN2A(G645) (Fig. 2.5a_2). Compared to the P_o values for the single glycine insertions at these sites, 0.36 for GluN1 and 0.08 for GluN2A (Fig. 2.4), the insertion of an additional glycine in GluN1 [GluN1(G648+2G)] (Fig. 2.5a_1) or GluN2A [GluN2A(G645+2G)] (Fig. 2.5a_2) resulted in a significantly lower P_o (0.16 ± 0.05, $n = 5$ & 0.008 ± 0.002, $n = 5$, respectively). The insertion of 4 glycines in GluN1 [GluN1(G648+4G)] (Fig. 2.5a_1) or GluN2A [GluN2A(G645+4G)] (Fig. 2.5a_2) also resulted in P_o values that were significantly less than their respective single glycine insertions (0.13 ± 0.02, $n = 4$ & 0.003 ± 0.001, $n = 6$, respectively) (Table 2.1). For GluN2A, the P_o values for the +2G and +4G constructs were significantly different ($p < 0.05$), whereas for GluN1 the difference was not statistically significant. One possibility for the lack of a significant decrease for GluN1 is that insertions beyond +2G may not result in the expected increases in linker length. Indeed, for insertions beyond +2G in GluN1 (Supplementary Fig. 2.2a) and to a lesser extent in GluN2A (Supplementary Fig. 2.3a), there were hints of new structural elements that might not increase the linker length as much as expected. Nevertheless, these results are consistent with the idea that pulling is required for efficient pore opening in NMDARs.

We also performed targeted MD simulations on NMDAR models containing the +4G insertions (Supplementary Fig. 2.4). Consistent with mechanical coupling, these additional insertions limited pore widening even more than the single glycine insertions (Supplementary Fig. 2.4c). We also found a striking parallel between pore radius derived from MD simulations and P_o (Fig. 2.5b), highlighting the relationship between these parameters.

Reductions in P_o must result from increases in mean closed time (MCT) and/or decreases in mean open time (MOT). Presumably, equivalent insertions in the different NMDAR subunits could exert their effects on MCT and MOT in a qualitatively comparable manner. Indeed, this alternative seems likely given that NMDARs gate in a concerted manner(Banke and Traynelis, 2003). Surprisingly, however, the effect of equivalent insertions in the different subunits was not comparable (Fig. 2.5c). In particular, single glycine insertions (+1G) in either GluN1 or GluN2A significantly increased MCT (8.5 ± 1.3 ms & 76.2 ± 27 ms, respectively) and reduced MOT (4.2 ± 0.5 ms & 4.2 ± 0.4 ms, respectively) relative to wild type MCT (3.8 ± 0.8 ms) and MOT (7.9 ± 0.9 ms). However, compared to +1G, four glycine insertions (+4G) in GluN2A further increased MCT (2300 ± 600 ms) but did not significantly increase MCT in GluN1 (12.4 ± 1.8 ms). On the other hand, +4G further decreased MOT in GluN1 (1.7 ± 0.1 ms) but not in GluN2A (3.7 ± 0.4 ms). Thus, it appears that pulling from the different subunits contributes to distinct features of pore opening with GluN2A mainly regulating the frequency of opening and GluN1 mainly regulating the duration of opening, though this distinction is by no means absolute. This idea is consistent with the prominent regulatory role of GluN2 in NMDAR activity (Siegler Retchless et al., 2012; Paoletti et al., 2013).

Deletions of residues in the M3-S2 linker could also affect the mechanical coupling between the LBD and the ion channel. However, from homology modeling (Phyre and SWISS-

MODEL), we often found that deletions in the M3-S2 linker altered local structures and led to ambiguous results from simulations (data not shown). Since interpreting the effects of insertions/deletions requires unaltered local structures and clear simulation results, we did not pursue the deletion experiments further.

Subunit-specific pulling energies during NMDAR activation

Subsequent to agonist binding, NMDARs undergo a series of kinetically resolvable transitions prior to pore opening (Fig. 2.2c) (Gibb and Colquhoun, 1991; Banke and Traynelis, 2003; Popescu and Auerbach, 2003; Auerbach and Zhou, 2005; Schorge et al., 2005). To discern how the pulling actions of the different subunits affect this activation sequence, we fit our cell-attached recordings to a kinetic model of NMDAR activation (Supplementary Figs. 2.5 & 2.6). Single glycine insertions in GluN1 (1.4 ± 0.2) or GluN2A (0.7 ± 0.1) (Fig. 2.6b$_1$) significantly reduced the equilibrium constant (K_{eq}) of the opening isomerization, C_1-O_1, compared to wild type (2.6 ± 0.3). In contrast, K_{eq} values for earlier transitions were only significantly reduced for GluN2A (C_3-C_2: 3.5 ± 0.4; C_2-C_1: 0.1 ± 0.02) but not for GluN1 (C_3-C_2: 6.5 ± 0.8; C_2-C_1: 0.3 ± 0.03) (Fig. 2.6b) compared to wild type (C_3-C_2: 7.1 ± 0.8; C_2-C_1: 0.4 ± 0.03) (Supplementary Table 2.4).

To test the functional implications of these kinetic models, we used the derived rates for GluN1/GluN2A (Fig. 2.6c$_1$), GluN1(G648+1G)/GluN2A (Fig. 2.6c$_2$), and GluN1/GluN2A(G645+1G) (Fig. 2.6c$_3$) to simulate NMDAR-mediated currents (Fig. 2.6c, *lower* panels) in response to 2 ms glutamate applications, as in Figure 2.1 (Fig. 2.6c, *upper panels*). Simulated currents for insertion constructs, compared to wild type, showed reduced peak amplitudes (Fig. 2.6c) and charge transfers (Fig. 2.6d), which largely paralleled experimental outcomes. The simulations also captured the strong subunit-specific differences. One notable

difference was that the simulated currents showed a slower rate of deactivation. This is most likely due to the differences in extracellular solutions (Traynelis et al., 2010) since the simulations were derived from single-channel experiments performed in a divalent-free, EDTA-containing media.

To quantify the energy by which the different linkers pull on the ion channel, we used the derived kinetic rates (Supplementary Table 2.4) to calculate the Gibbs free energy difference ($\Delta\Delta G$) for each kinetic transition (Fig. 2.7a). From the linear fit to these plots, we determined a pulling factor (k) which quantifies the pulling strength along the linker during a given transition. At the concerted opening transition, C_1-O_1, the pulling factors for GluN1 and GluN2A were comparable (1.3 & 1.1 kcal/mol/nm, respectively). In contrast, GluN2 exerts greater pulling energy during earlier transitions. Thus the different subunits pull on the ion channel with about equal veracity during the final pore opening transition (C_1-O_1). This is consistent with concerted gating in NMDARs with a rapid, but relatively uniform pore opening isomerization. On the other hand, prior to this pore opening transition, the GluN2 subunit is exerting significant energy and hence must undergo more extensive isomerization compared to GluN1. Indeed, the average GluN2A k across all transitions (1.6 ± 0.3 kcal/mol/nm) is greater than the average k for GluN1 (0.66 ± 0.3 kcal/mol/nm) by a factor of approximately 2.4. From our MD simulations, the GluN2A M3 helices at the level of the pore entrance were found to separate more (8.5 Å) than that of GluN1 (3.6 Å) by a factor of approximately 2.4 (Fig. 2.7c). Thus, subunit-specific pulling energy may account for the differences in M3 helix separation and suggests asymmetrical pre-open state conformational changes before concerted pore opening.

DISCUSSION

Our results indicate that the tight linkage between agonist binding and ion channel opening in NMDARs is critical to their ability to convert transient glutamate into a robust functional response. We propose that this linkage is mainly, though not exclusively, due to mechanical coupling between domains in which the LBD of the NMDAR subunits pulls on the pore-lining M3 helix, facilitating pore opening. Both the glycine-bound GluN1 and glutamate-bound GluN2 subunits pull on M3 with about equivalent energy to open the pore (C_1-O_1), but surprisingly the GluN2 subunit transduces more energy during earlier transitions (Fig. 2.7b). Thus, under synaptic conditions where the glycine-binding site is generally thought to be saturated, synaptically-released glutamate acts as a rate limiting step to pore opening.

The functional properties of NMDARs, including pore opening, are determined by the specific GluN2 subunit (GluN2A, 2B, 2C, 2D) (Yuan et al., 2009; Paoletti et al., 2013). While both GluN1 and GluN2A showed evidence of pulling, we find that pulling in GluN2A occurs earlier and is more dynamic (Fig. 2.7b). As such, varied pulling energetics across the GluN2 subunits may contribute to the diversity of NMDAR activity. Further, because the GluN2 subunit must transfer more energy, mutations in it would likely produce more dramatic pathological phenotypes. Indeed, compared to GluN1, a greater number of missense mutations in the GluN2A subunit have been associated with neurological diseases (Hamdan et al., 2011; Lemke et al., 2013; Lesca et al., 2013).

Although our results are consistent with a mechanical pulling model of channel opening(Armstrong and Gouaux, 2000; Jin et al., 2003; Niu et al., 2004; Furukawa et al., 2005; Dong and Zhou, 2011; Dai and Zhou, 2013), the nature of the mechanical components remains to be resolved. Indeed, mechanical forces could entail twisting or rocking components(Yao et al.,

2013). Further, it is possible for channel opening to depend on shuffling the interactions of residue side chains, as is found in pentameric channels (Lee and Sine, 2005; Purohit et al., 2007; Dacosta and Baenziger, 2013). Indeed, mutations along the coupling linkers in iGluRs impact the stability of activation and desensitization states but it is unclear how such mutations may affect the dynamics of pore opening (Jones et al., 2002; Traynelis et al., 2010). The availability of a full-length structure of NMDARs, as opposed to a homology model, would provide better insights into these questions.

Recently, several neurological pathologies were associated with inherited and *de novo* NMDAR mutations that alter channel opening. Indeed, missense mutations within the GluN1 and GluN2A linkers have been identified in patients diagnosed with epileptic aphasic syndromes (specifically, Landau-Kleffner syndrome) and intellectual disabilities (Hamdan et al., 2011; Lesca et al., 2013). Surprisingly, insertion and deletion mutations in GluN2A or GluN1 were found in patients exhibiting focal epilepsies or mental retardation coupled with hypotonia, respectively (Hamdan et al., 2011; Lemke et al., 2013). Thus, efficient mechanical coupling is vital to NMDAR function and disruption of this process can lead to devastating clinical pathologies.

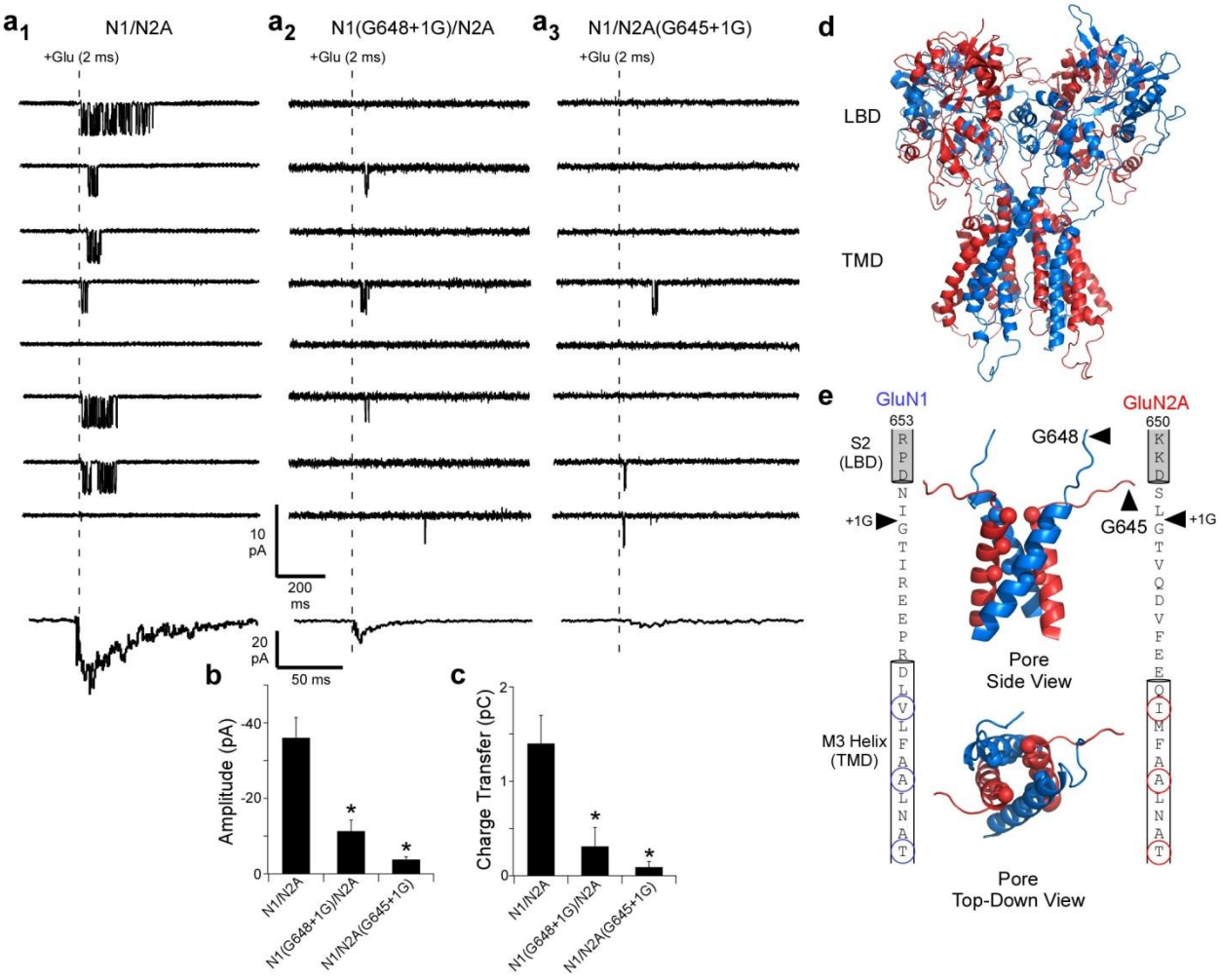

Figure 2.1 A single glycine insertion in the GluN1 or GluN2A M3-S2 linker dramatically attenuates activity in response to transient glutamate

(**a**) *Top*, current traces (sampled at 25 kHz, displayed at 0.7 kHz) from outside-out patches in response to a brief application (2 ms, dashed line) of glutamate (1 mM) for GluN1/GluN2A (**a**$_1$), GluN1(G648+1G)/GluN2A (**a**$_2$), or GluN1/GluN2A(G645+1G) (**a**$_3$). Currents were recorded in the continual presence of glycine (0.1 mM). For GluN1/GluN2A, all patches contained exactly one channel but for the insertion constructs there were $\leq$ 2 channels. *Bottom*, summed current profile for individual patches (See Materials and Methods). Current profiles are the average of currents summed over 25 consecutive applications, including applications with no detectable openings (failures). Total applications & sets averaged: GluN1/GluN2A, 50 & 2; GluN1(G648+1G)/GluN2A, 300 & 12; GluN1/GluN2A(G645+1G), 225 & 9.
(**b**) Model structure of a GluN1(*blue*)/GluN2A(*red*) NMDAR(Dai and Zhou, 2013).
(**c**) *Inner panels*, side (*top*) and top-down (*bottom*) view of the pore, formed by the M3 transmembrane helices. Spheres indicate α-carbons presumed to form the NMDAR gate(Chang and Kuo, 2008; Sobolevsky et al., 2009): top-to-bottom: GluN1(V638)/GluN2A(I635); GluN1(A634)/GluN2A(A631); and GluN1(T630)/GluN2A(T627). *Outer panels*, Sequence of the M3-S2 linkers and adjoining M3 transmembrane helices and S2 segments for GluN1 (*left*)

and GluN2A (*right*). Helical cut-offs are based on the NMDAR model. Arrowheads indicate sites of glycine insertion. Circles (spheres in structure) highlight gate-forming residues. (**d & e**) Mean (± SEM) peak amplitude (**b**) and charge transfer (**c**) for summed currents (**a**, *bottom traces*); GluN1/GluN2A (n = 5 patches, 10 sets), GluN1(G648+1G)/GluN2A (n = 3 patches, 29 sets), GluN1/GluN2A(G645+1G) (n = 2 patches, 19 sets). * indicates a significant difference relative to GluN1/GluN2A ($p < 0.05$, two-tailed Student's t-test, unpaired).

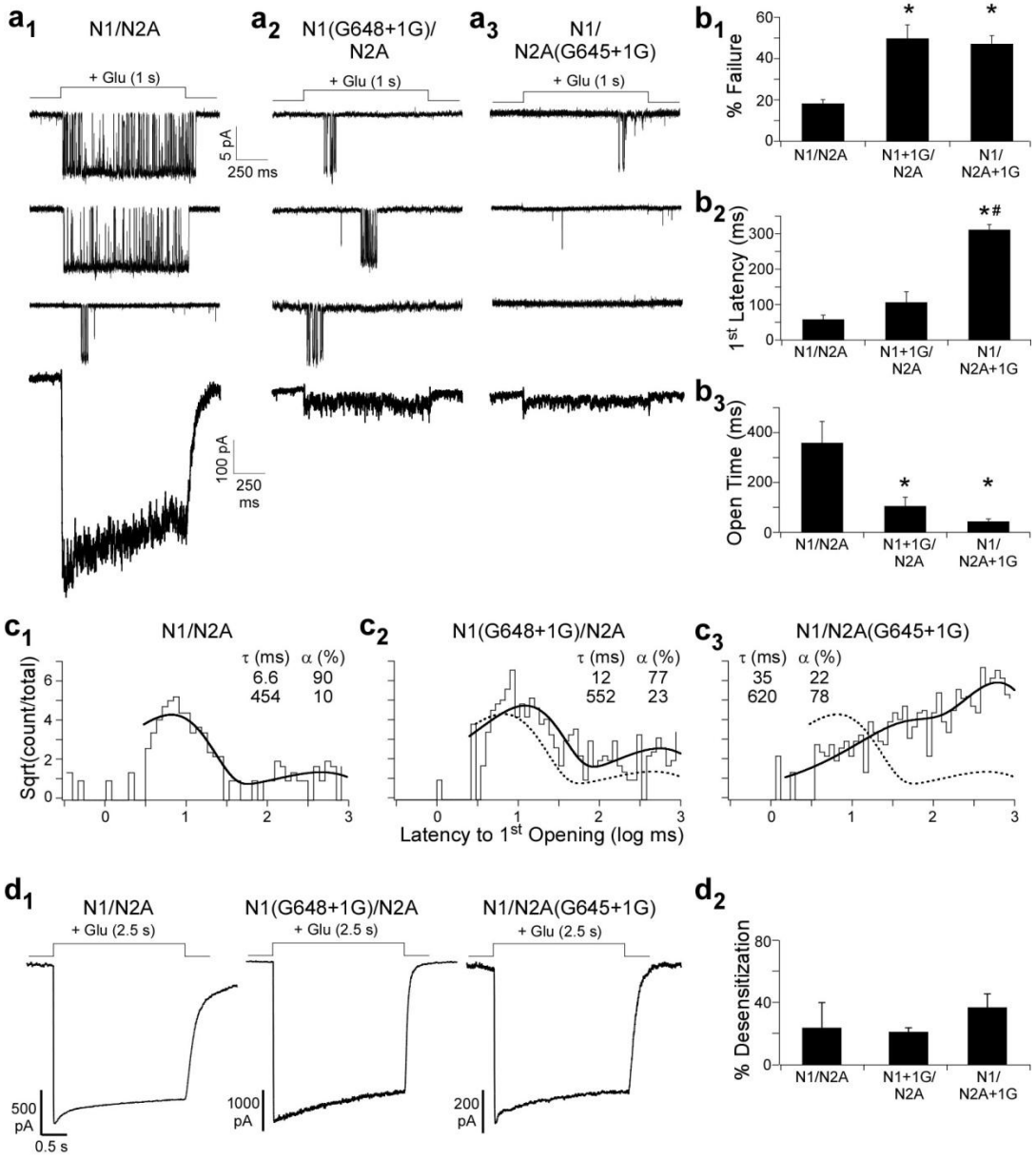

Figure 2.2 Insertions in the M3-S2 linkers increase failure rate and latency to 1st opening and reduce channel open time

(**a**) *Top*, Current traces (3 total) from outside-out patches in response to long applications (1 s) of glutamate (1 mM) for GluN1/GluN2A (**a$_1$**), GluN1(G648+1G)/GluN2A (**a$_2$**), or GluN1/GluN2A(G645+1G) (**a$_3$**). Pulses were delivered approximately every 3 seconds. Currents were recorded in the continual presence of glycine (0.1 mM) and sampled at 50 kHz (shown at ~ 1 kHz). All patches contained a single channel. *Bottom*, current profile after summing 100 consecutive sweeps.

(**b**) Mean (± SEM) % failure (**b$_1$**), latency to 1st channel opening (**b$_2$**), and channel open time (**b$_3$**) for GluN1/GluN2A (n = 6 patches), GluN1(G648+1G)/GluN2A (n = 8 patches), and GluN1/GluN2A(G645+1G) (n = 9 patches). Channel open time (**b$_3$**) is the average time spent in the open state per application that shows activity (see Materials and Methods). A significant

difference is indicated either relative to GluN1/GluN2A (*) or to GluN1(G648+1G)/GluN2A ($^{\#}$) ($p < 0.05$, two-tailed Student's t-test, unpaired).
(**c**) Cumulative distribution of latency to 1st opening for GluN1/GluN2A (**c_1**, 244 applications), GluN1(G648+1G)/GluN2A (**c_2**, 297 applications), and GluN1/GluN2A(G645+1G) (**c_3**, 388 applications). All distributions were best fit by the sum of two exponential functions (thick line) with time constants (τ, ms) and occupancies (α, %) shown. The dashed line in **c_2** and **c_3** is the superimposed best fit for GluN1/GluN2A in **c_1**.
(**d**) Whole-cell current recordings (**d_1**) in response to a 2.5 s application of glutamate (1 mM).
(**d_2**) Mean (± SEM, $n \geq 3$) % desensitization. Values were not statistically different.

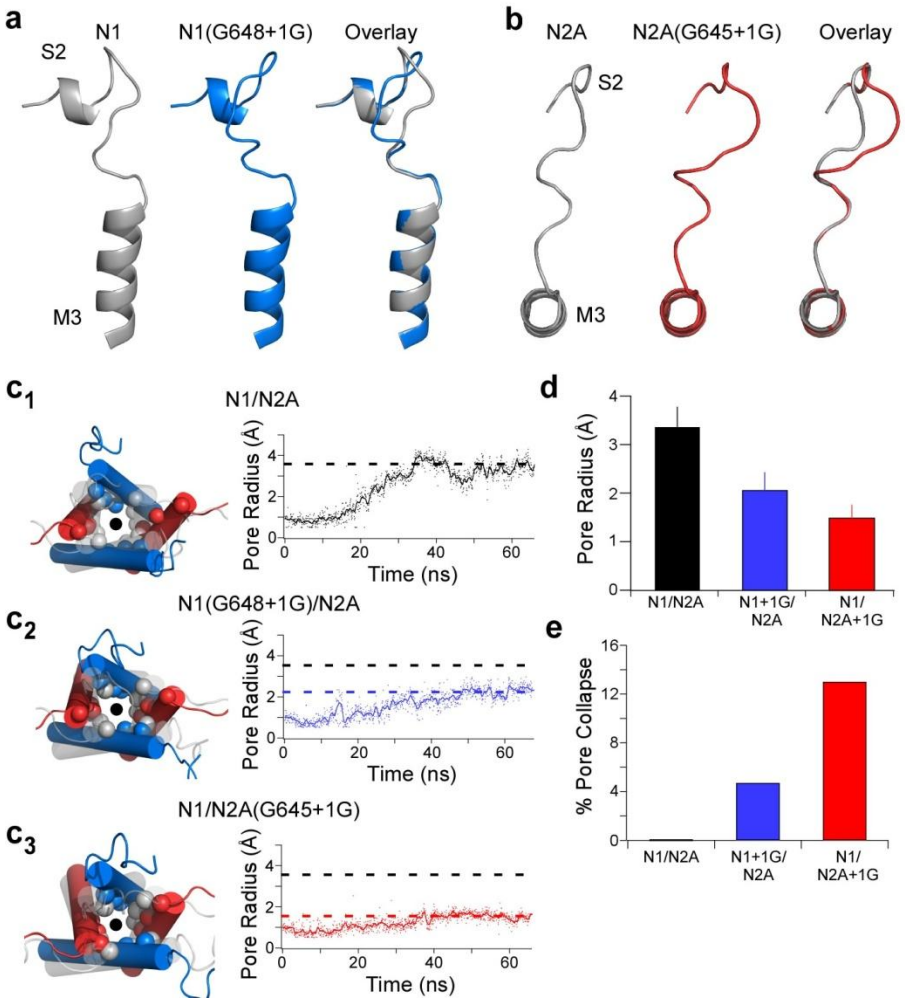

Figure 2.3 M3-S2 insertions attenuate pore opening in all-atom molecular dynamics simulations of modeled GluN1/GluN2A NMDARs

(**a & b**) Glycine insertions in the M3-S2 linker increase linker length. Model structures for the region around M3-S2 of GluN1(G648+1G) (**a**, *side view*) and GluN2A(G645+1G) (**b**, *top-down view*) in the resting state. Shown are M3-S2 for wild type (*left, grey*), the +1G insertion (*middle, color*), and their overlay (*right*).

(**c_1-c_3**) *Left*, Overlaid structural snapshots of the ion channel pore (circle) at 0 ns (*grey, faded*) and after 65 ns of simulation (colored) with spheres highlighting α-carbons of the three gate-forming rings (Fig. 2.1c). *Right*, Change in pore radius from 0 ns to 65 ns. Shown are the filtered (line) and unfiltered (dots) traces for each construct. Dashed lines reflect average pore radius for the last 35 ns for GluN1/GluN2A (*black*), GluN1(G648+1G)/GluN2A (*blue*), and GluN1/GluN2A(G645+1G) (*red*). Pore radius was measured at the most extracellular ring formed by GluN1(V638) and GluN2A(I635).

(**d**) Mean (± standard deviation) pore radius across the final 35 ns (using 700 frames) of the MD simulations for tested constructs.

(**e**) % pore collapse (% of time with pore radius < 1 Å) for each construct.

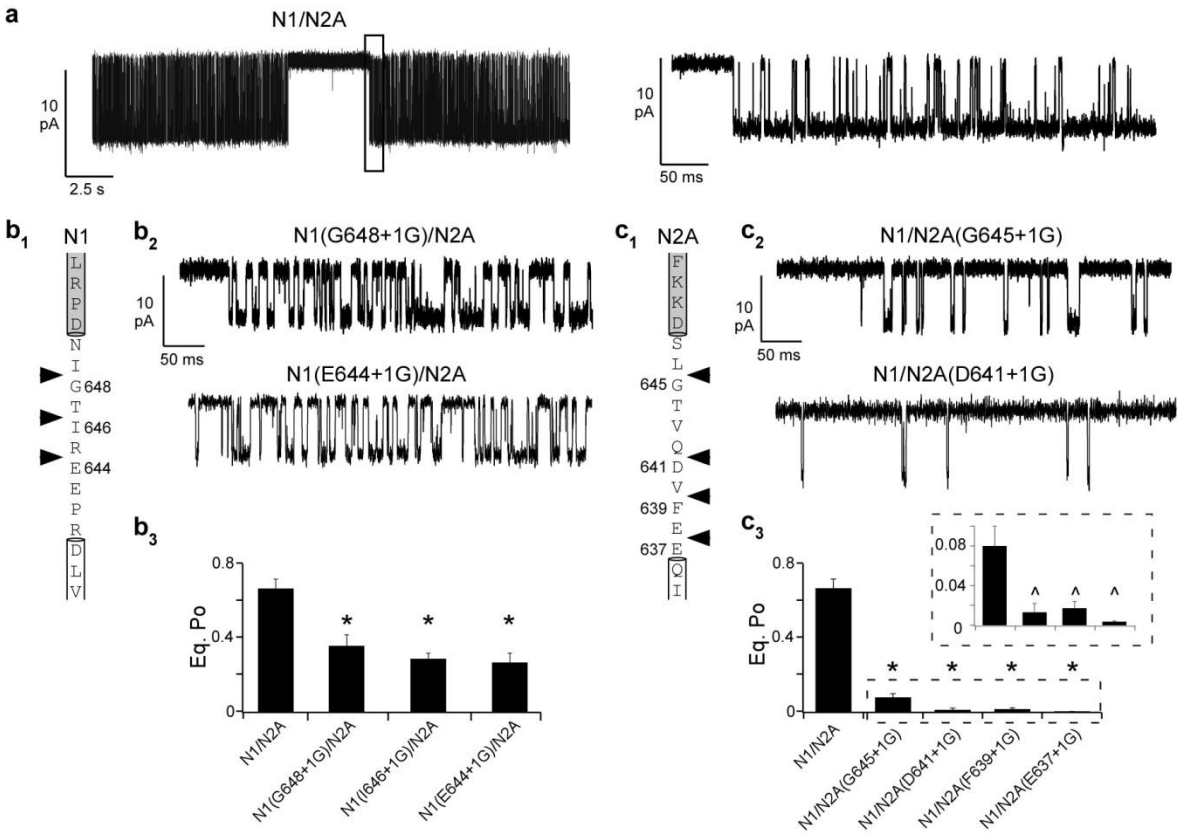

Figure 2.4 Insertions at different points in the M3-S2 linker attenuate pore opening

(**a**) Current traces from cell-attached patches for a single GluN1/GluN2A NMDAR at steady state either at low resolution (*left*, digitally filtered at 1 kHz) or high resolution of the boxed region (*right*, digitally filtered at 3 kHz). Patch pipettes contained saturating agonists (1 mM glutamate, 0.1 mM glycine).
(**b & c**) Glycine insertions at different points throughout the M3-S2 linker in either GluN1 (**b**) or GluN2A (**c**) significantly reduce equilibrium open probability (P_o) compared to GluN1/GluN2A.
(**b_1 & c_1**) Sequence of the GluN1 (**b_1**) and GluN2A (**c_1**) M3-S2 linkers with the adjoining M3 helix (*white box*) and S2 segment (*grey box*). Arrowheads indicate points of single glycine insertions.
(**b_2 & c_2**) Single channel traces (approximately 0.5 s, digitally filtered at 3 kHz) for GluN1(G648+1G)/GluN2A (**b_2**, *top*) or GluN1(E644+1G)/GluN2A (**b_2**, *bottom*) and GluN1/GluN2A(G645+1G) (**c_2**, *top*) or GluN1/GluN2A(D641+1G) (**c_2**, *bottom*).
(**b_3 & c_3**) Mean (± SEM) equilibrium P_o for glycine insertions in the GluN1 (**b_3**) or GluN2A (**c_3**) M3-S2 linker. The boxed inset in C_3 shows equilibrium P_o at a higher resolution. Significant difference is indicated either relative to GluN1/GluN2A (*) or to GluN1/GluN2A(G645+1G) (^) ($p < 0.05$, two-tailed Student's t-test, unpaired).

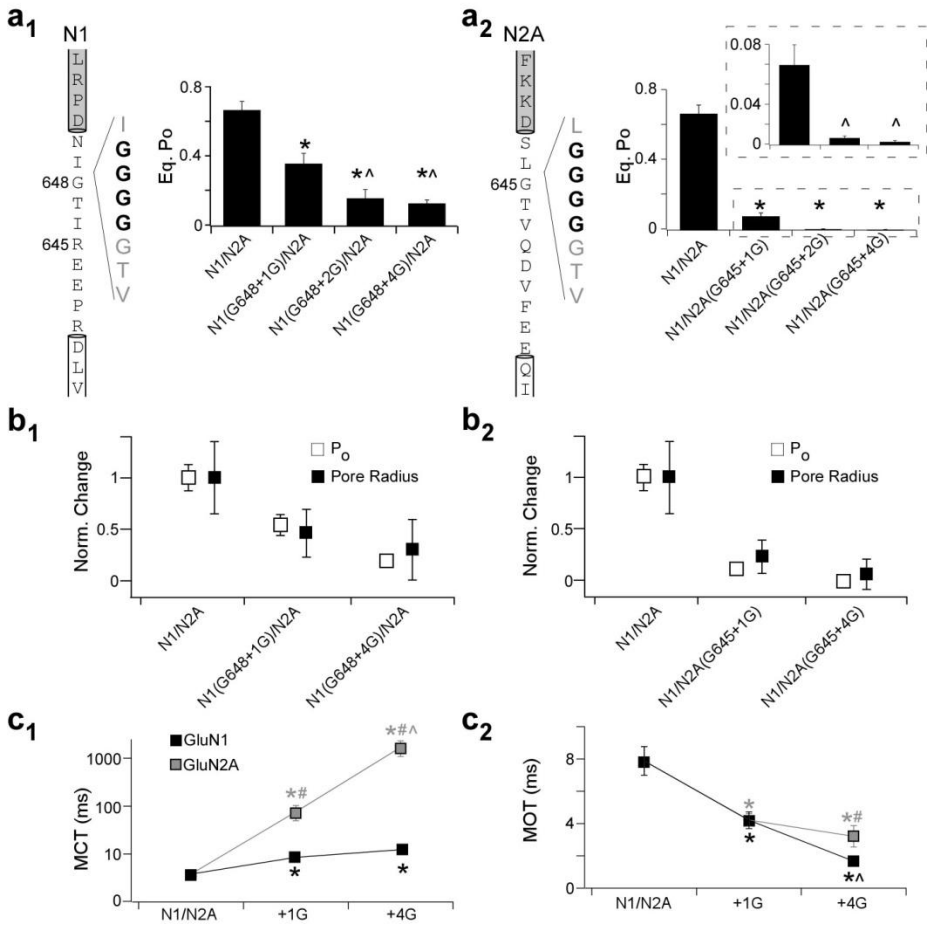

Figure 2.5 Additional insertions in the M3-S2 linkers further reduce pore opening

(**a**) *Left*, sequence for GluN1 (**a$_1$**) and GluN2A (**a$_2$**) M3-S2 linkers, with +4G insertions indicated in bold text. *Right*, mean (± SEM) equilibrium P_o for increasing glycine insertions. A significant difference is indicated either relative to GluN1/GluN2A (*) or to the respective +1G construct for each subunit (^) ($p < 0.05$, two-tailed Student's t-test, unpaired).
(**b**) Glycine insertions have parallel effects on pore radius (*black squares*) and P_o (*open squares*) for +1G and +4G insertions in GluN1 (**b$_1$**) and GluN2A (**b$_2$**). All values are normalized to those for GluN1/GluN2A.
(**c**) Insertions have subunit-specific effects on mean closed (MCT) and mean open (MOT) times. Mean (± SEM) closed (**c$_1$**) and open (**c$_2$**) time for +1G and +4G insertions for GluN1 (*black*) or GluN2A (*grey*). Note that MCT is plotted on a logarithmic scale. Significant difference is indicated either relative to GluN1/GluN2A (*), between GluN1 and GluN2A for the same manipulation ($^{\#}$), or to the respective +1G construct for each subunit (^) ($p < 0.05$, two-tailed Student's t-test, unpaired).

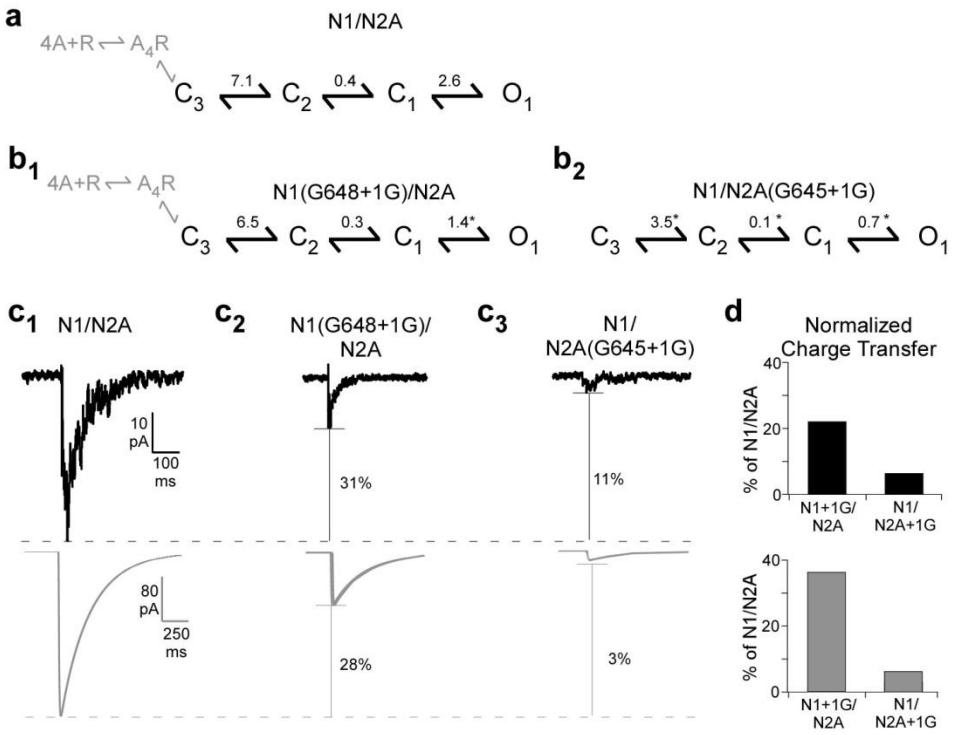

Figure 2.6 Activation models for single glycine insertions in GluN1 or GluN2A

All kinetic analysis was performed at a dead time of 0.024 ms.
(**a**) Kinetic schemes and equilibrium constants (Supplementary Table 4) for GluN1/GluN2A analyzed at equilibrium. Ligand binding steps are shown in grey.
(**b**) Kinetic schemes and equilibrium constants for GluN1(G648+1G) (**b_1**) or GluN2A(G645+1G) (**b_2**). Significant difference is indicated relative to GluN1/GluN2A (*).
(**c**) Simulated currents for single glycine insertion constructs parallel measured responses. *Top*, summed current profiles from Fig.2.1a for 2 ms glutamate applications to outside-out patches for GluN1/GluN2A (**c_1**), GluN1(G648+1G)/GluN2A (**c_2**), or GluN1/GluN2A(G645+1G) (**c_3**). *Bottom,* simulated current traces for the same constructs. Simulations were performed using derived kinetic rates (Supplementary Table 4) in response to a 2 ms glutamate application. Indicated for each is the % reduction in peak current amplitude.
(**d**) Charge transfer for measured (*top*) and simulated (*bottom*) currents normalized to GluN1/GluN2A.

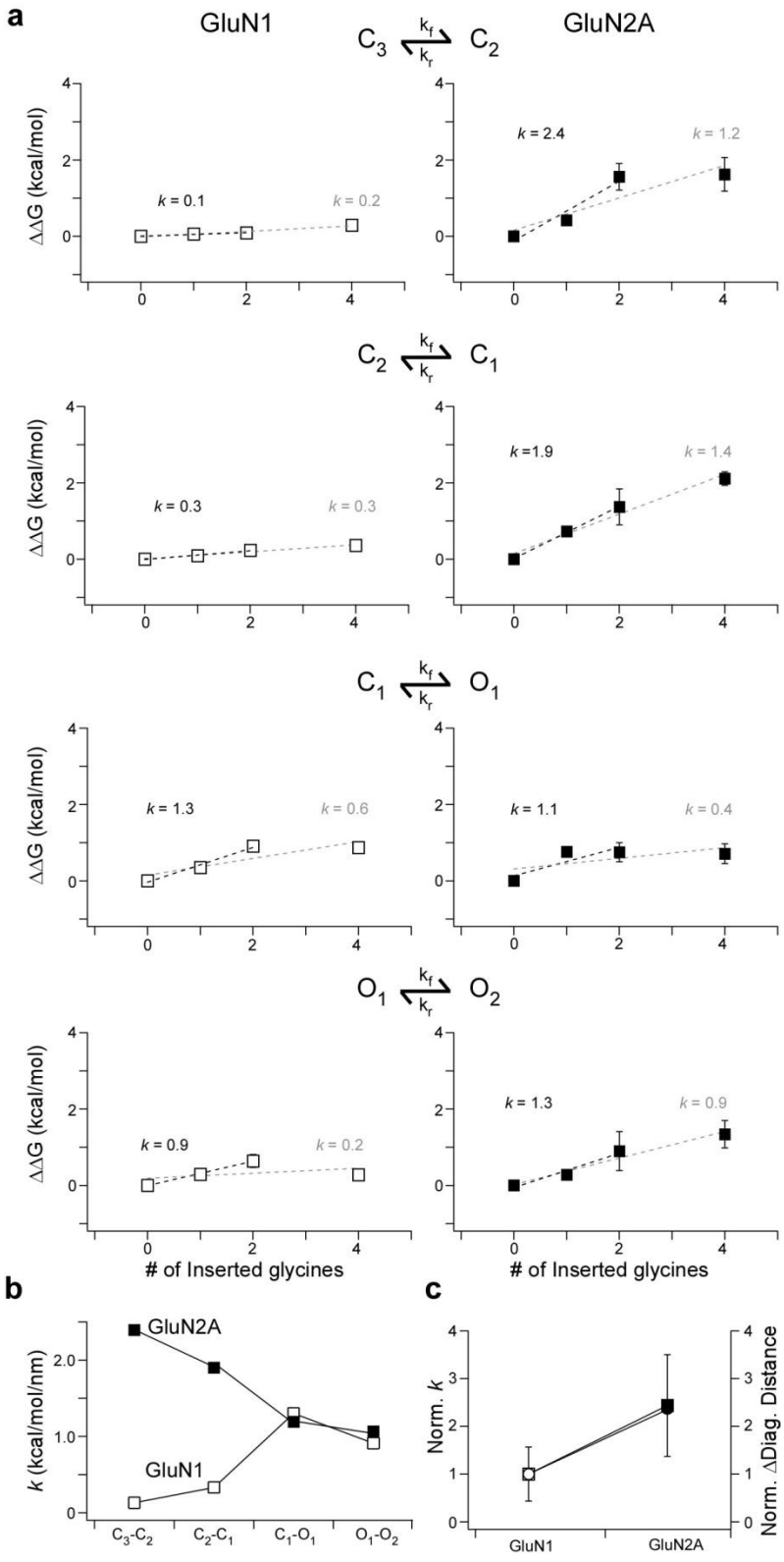

Figure 2.7 The GluN2A subunit moves earlier and transduces more energy than the GluN1 subunit

(**a**) The GluN2A subunit transfers more energy per unit length than GluN1. Plots correlating ΔΔG (kcal/mol) as a function of insertion length for GluN1 (*left, white*) or GluN2A (*right, black*) for the NMDAR activation transitions (C_3-C_2, C_2-C_1, C_1-O_1, O_1-O_2). Also shown is the slope (*k*, kcal/mol/nm) for linear fits to the first three (*black*) or four (*grey*) points. For subsequent analysis, we used values derived from the three-point fit due to uncertainty whether residue insertions beyond +2G were increasing the linker length as expected (Supplementary Figs. 2.2 & 2.3).
(**b**) Pulling energetics are approximately the same during the concerted pore opening step. Summary plots for pulling energy during NMDAR activation for GluN1 (*white squares*) or GluN2A (*black squares*).
(**c**) The subunit differences in pulling energy parallel differences in pore opening. Plot for the average pulling energy (*squares*) and change in distance between like-subunit M3 helices after activation (*circles*) for GluN1 (*white*) and GluN2A (*black*). Values are normalized to GluN1. The average pulling factor was calculated assuming that the pulling factors for each transition contribute equally.

	Total Events	*i* (pA)	P_o	MCT (ms)	MOT (ms)
GluN1/GluN2A	1,876,000 (8)	-7.9 ± 0.3	0.67 ± 0.06	3.8 ± 0.8	7.9 ± 0.9
GluN1					
G648+1G	1,760,000 (8)	-8.1 ± 0.5	0.36 ± 0.06*	8.5 ± 1.3*	4.2 ± 0.5*
G648+2G	458,000 (5)	-12 ± 1*^	0.15 ± 0.05*^	13.9 ± 3.9*	1.5 ± 0.1*^
G648+4G	598,000 (4)	-12 ± 1*^	0.13 ± 0.02*^	12.4 ± 1.8*	1.7 ± 0.1*^
GluN2A					
G645+1G	237,000 (6)	-8.2 ± 0.4	0.08 ± 0.2*$^{\#}$	76.2 ± 27*$^{\#}$	4.2 ± 0.4*
G645+2G	14,100 (5)	-9.5 ± 1.6	0.008 ± 0.002*^$^{\#}$	620 ± 80*^$^{\#}$	5.1 ± 1.4
G645+4G	12,300 (6)	-11.5 ± 0.8*	0.003 ± 0.001*^$^{\#}$	2300 ± 600*^$^{\#}$	3.7 ± 0.4*$^{\#}$

Table 2.1 Insertions in the GluN1 or GluN2A M3-S2 linker reduce channel open probability

Mean values (± SEM) for single-channel current amplitudes (*i*), equilibrium open probability (P_o), mean closed time (MCT), and mean open time (MOT) for wild type and insertion constructs in GluN1 or GluN2A. Single-channels data was recorded in the cell-attached configuration and analyzed in QuB. Number of patches is in parenthesis to the right of total event numbers. Significant difference is indicated either relative to GluN1/GluN2A (*), to the respective +1G construct for each subunit (^), or between GluN1 and GluN2A for the same mutation ($^{\#}$) ($p < 0.05$, two-tailed Student's t-test, unpaired).

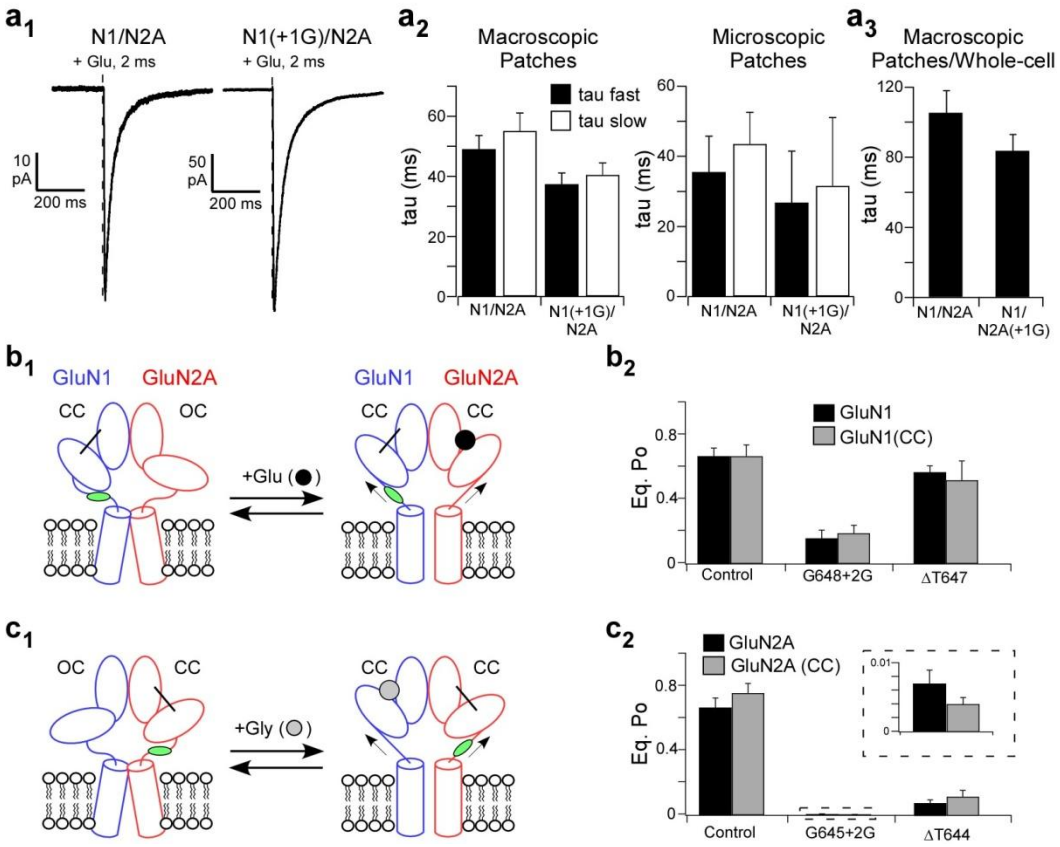

Supplementary Figure 2.1 Manipulations in the M3-S2 linkers exert effects largely independent of LBD dynamics

(**a**) Single glycine insertions in GluN1 or GluN2A have no significant effect on deactivation rates, which for NMDARs are related to ligand unbinding and hence an index of LBD dynamics(Lester and Jahr, 1992; Vance et al., 2011).
(**a_1**) Representative macroscopic currents from outside-out patches in response to a 2 ms application of glutamate (1 mM). For GluN1/GluN2A(G645+1G), macroscopic currents with 2 ms applications could not be measured but could be using 10 ms applications (not shown).
(**a_2**) Mean (± SEM, n ≥ 8) rates of deactivation for macroscopic (*left*) and summed currents of microscopic (1-2 channels, from Fig. 2.1) (*right*) patches for 2 ms applications. Rates were best fit using a biexponential function giving a fast (*black*) and slow (*white*) tau.
(**a_3**) Mean (± SEM, n ≥ 4) rates of deactivation for outside-out patches/whole cell recordings following a 10 ms application of glutamate for GluN1/GluN2A or GluN1/GluN2A(G645+1G). Rates were best fit with a single exponential function
Deactivation rates in **a2** & **a3** were not significantly different.
(**b & c**) Forcing the LBD into a closed clamshell configuration has no effect on open probability for M3-S2 insertion or deletion constructs, indicating that manipulations in the M3-S2 linkers do not affect LBD clamshell closure.
(**b_1 & c_1**) NMDAR LBDs were closed using two engineered cysteines (CC) across the cleft in either GluN1 (**b_1**) or GluN2A (**c_1**) (Blanke and VanDongen, 2008; Kussius and Popescu, 2010). Single-channel activity was recorded in the cell-attached configuration. For GluN1(CC)/GluN2A, the pipette solution contained glutamate (1 mM) with no added glycine.

For GluN1/GluN2A(CC), the pipette solution contained glycine (0.1 mM) with no added glutamate.
(**b_2 & c_2**) Mean (± SEM, n $\geq$ 3) open probability for the control, +2G, and deletion constructs tested in the wild type LBD (*black*) or CC (*grey*) LBD background. Values for like manipulations in different backgrounds were not statistically different.

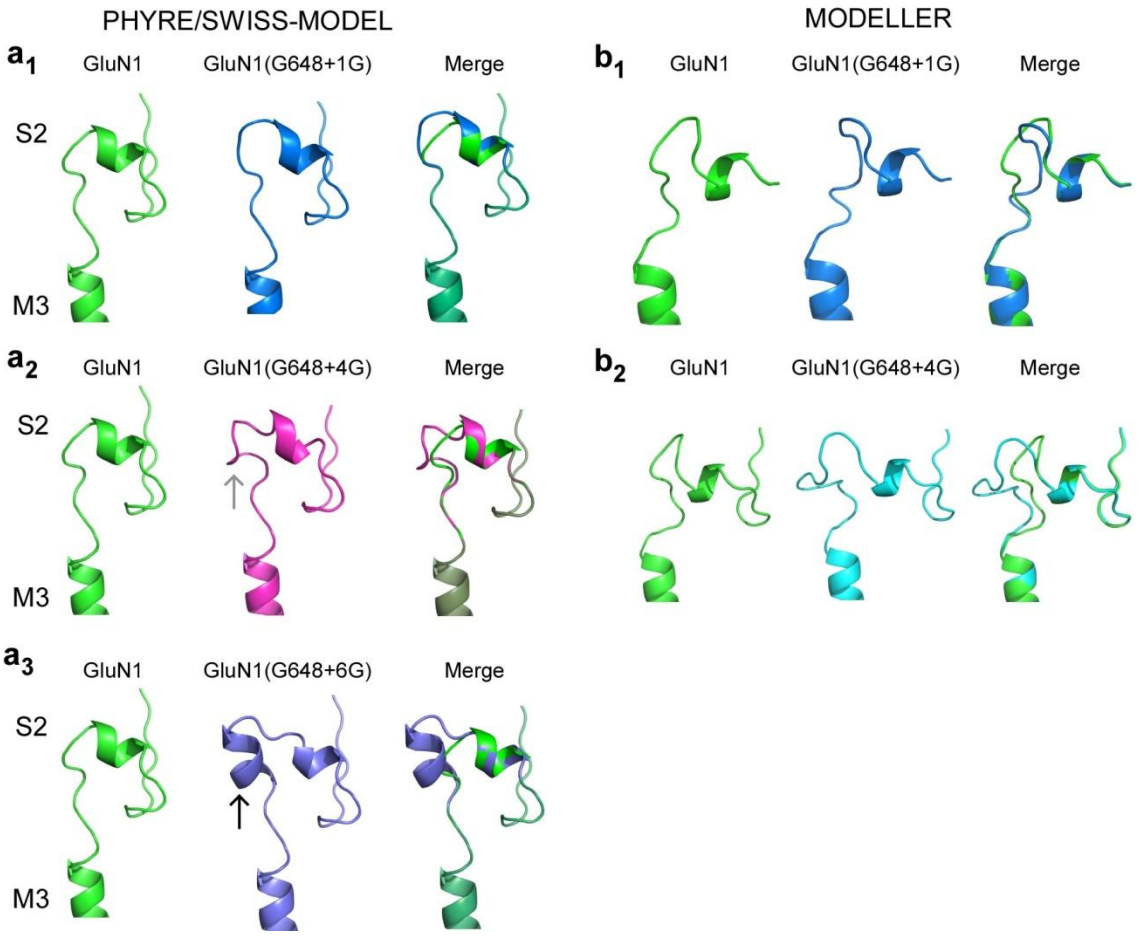

Supplementary Figure 2.2 Insertions ≤ 4 residues in the GluN1 M3-S2 primarily increase linker length (relates to Fig. 2.3).

To characterize the structural effects of insertions on secondary structure, we used homology modeling (PHYRE/SWISS-MODEL) (see Materials and Methods).
(**a & b**) Homology models built using PHYRE/SWISS-MODEL modeling servers (**a**) or MODELLER (**b**) for GluN1(G6458+1G) (**a_1 & b_1**), GluN1(G648+4G) (**a_2 & b_2**), and GluN1(G648+6G) (**a_3**). +1G and +4G insertions predominantly increase the length of M3-S2 while the +6G insertion adds an additional local secondary structure (*black arrow*). The +4G model also shows a potential turn (*grey arrow*).

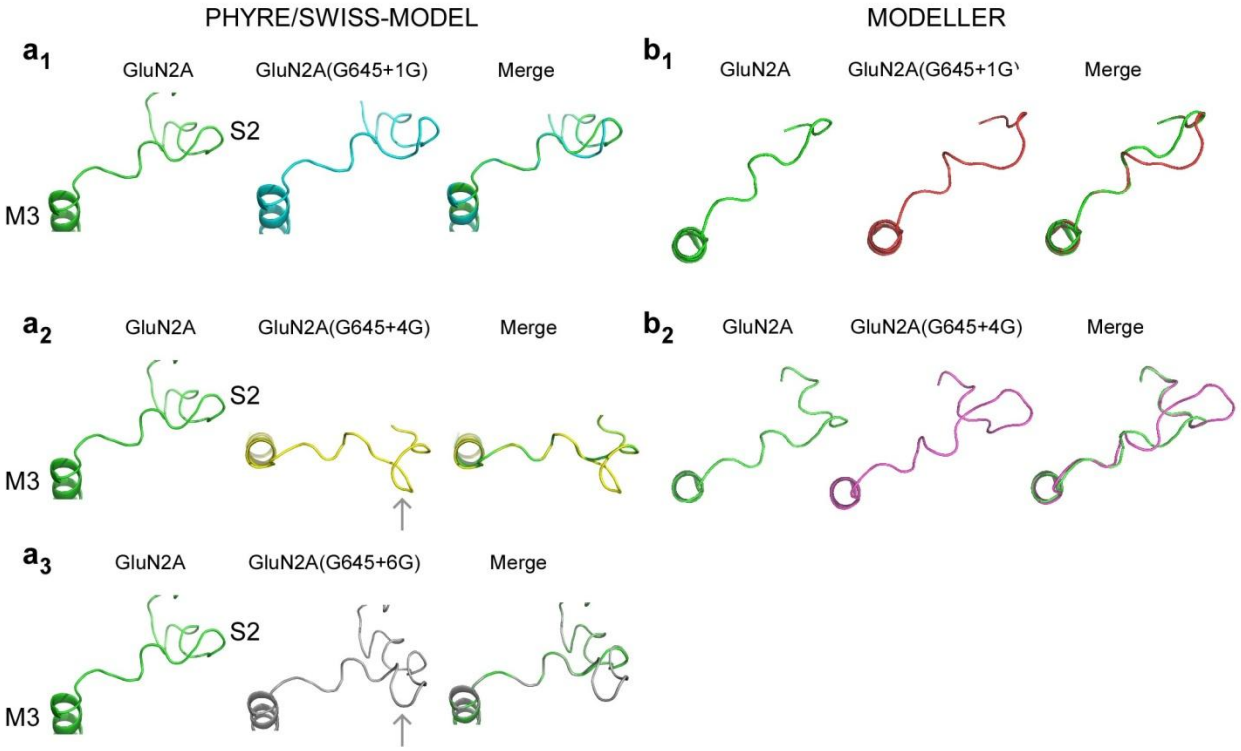

Supplementary Figure 2.3 Insertions in GluN2A M3-S2 increase linker length (relates to Fig. 2.3)

Same legend as Supplementary Fig. 2.3 except that modeling is for the GluN2A subunit. None of the insertions produced notable changes in secondary structures though +4G and +6G show a potential turn (*grey arrows*).

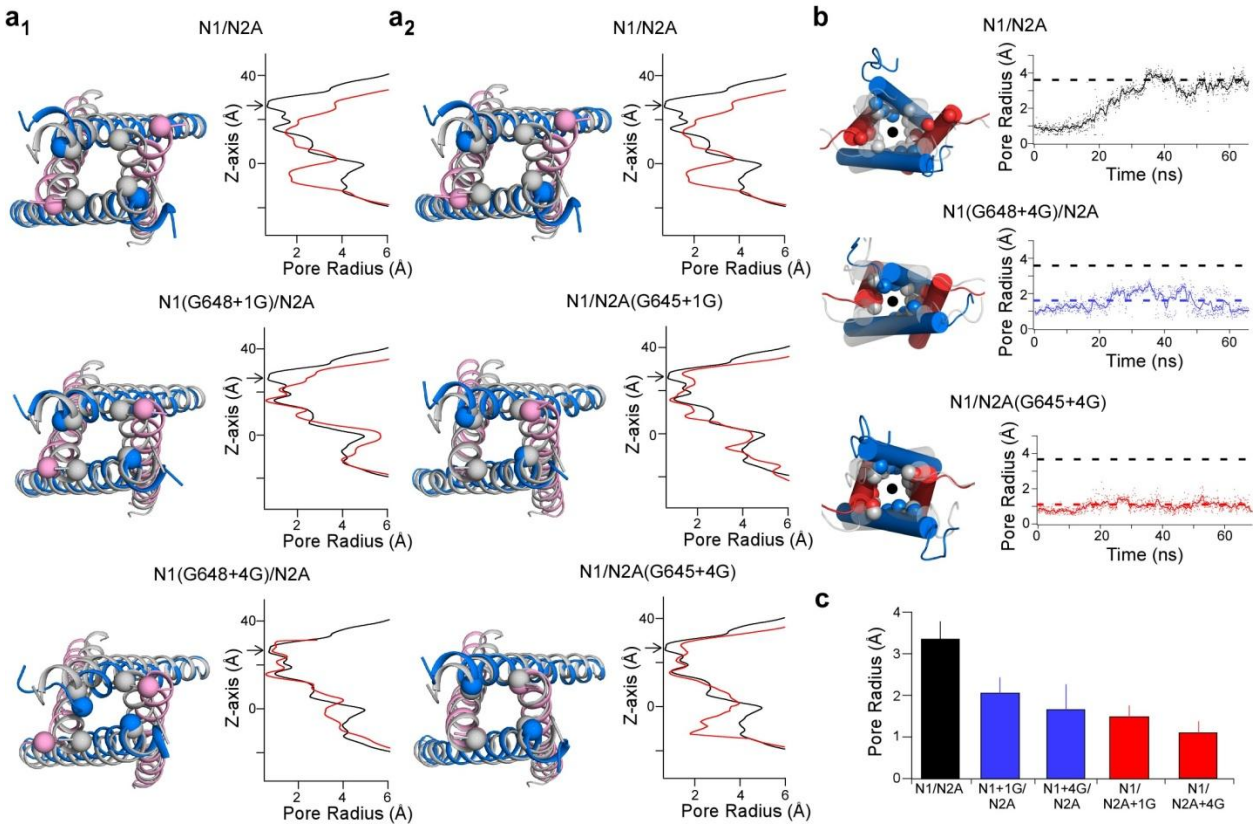

Supplementary Figure 2.4 M3-S2 insertions reduce the efficiency of pore widening (relates to Figs. 2.3 & 2.5)

(**a**) M3-S2 insertions reduce pore widening along the length of the pore. *Left*, Top-down view of the pore at the beginning (*grey*) and end (*colored*) of MD simulations for +1G or +4G insertions in GluN1 (**a**$_1$, *blue*) or GluN2A (**a**$_2$, *pink*). *Right*, Pore radius measurements for representative simulations along the z-axis at the beginning (*black*) and end (*red*) of the simulation. The arrow highlights the outermost ring formed by GluN1(V638) and GluN2A(I635) which was used for pore radius measurements in Figure 2.3c and Supplementary Figures 2.4b & 2.4c.
(**b**) Additional insertions in the M3-S2 linker (+4G) further reduce pore widening compared to +1G insertions. *Left*, Overlaid structural snapshots of the ion channel pore (circle) for GluN1(G648+4G)/GluN2A and GluN1/GluN2A(G645+4G) at 0 ns (*grey*, *faded*) and after 65 ns of simulation (*colored*) with spheres highlighting □-carbons of the three gate-forming rings (Fig. 2.1e). *Right*, Change in pore radius from 0 ns to 65 ns. Shown are the filtered (solid line) and unfiltered (dots) traces for each construct. Pore radius was measured at the outermost ring.
(**c**) Mean (± Standard Deviation) pore radius across the final 700 frames (35 ns) for GluN1/GluN2A (3.3 ± 0.4 Å), GluN1(G648+1G)/GluN2A (2.0 ± 0.4 Å), GluN1(G648+4G)/GluN2A (1.6 ± 0.6 Å), GluN1/GluN2A(G645+1G) (1.5 ± 0.3 Å), and GluN1/GluN2A(G645+4G) (1.1 ± 0.3 Å).

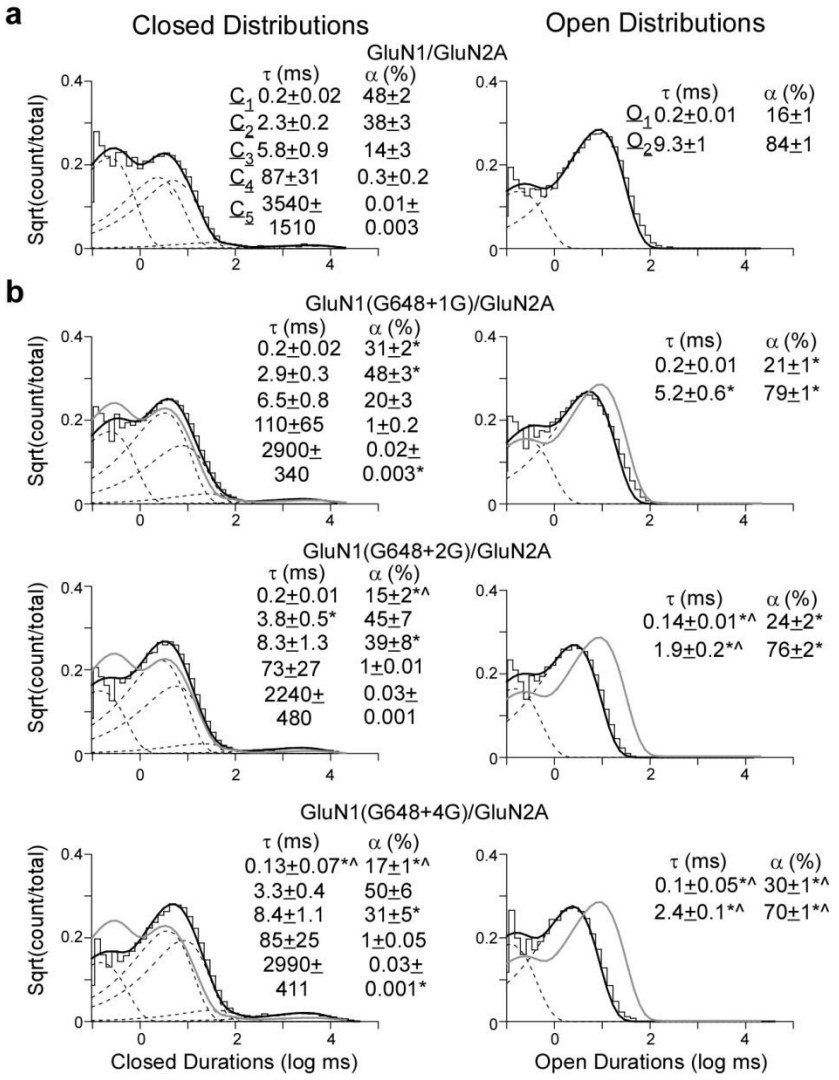

Supplementary Figure 2.5 Equilibrium open and closed time distributions for wild type and GluN1 insertion constructs (relates to Fig. 2.6)

Closed (*left*) and open (*right*) durations for GluN1/GluN2A (**a**) and GluN1(G648+nG)/GluN2A (**b**) where n = 1, 2, or 4. For all constructs, the closed-time distributions were best fit by five exponentials. Although there was considerable variation across patches in terms of the number of open state exponentials (2 to 4), we fitted all open state distributions with 2 exponentials to permit comparisons across different constructs. *Insets*, mean values (±SEM) for closed and open state durations (*left*, τ, ms) and occupancies (*right*, α, %).

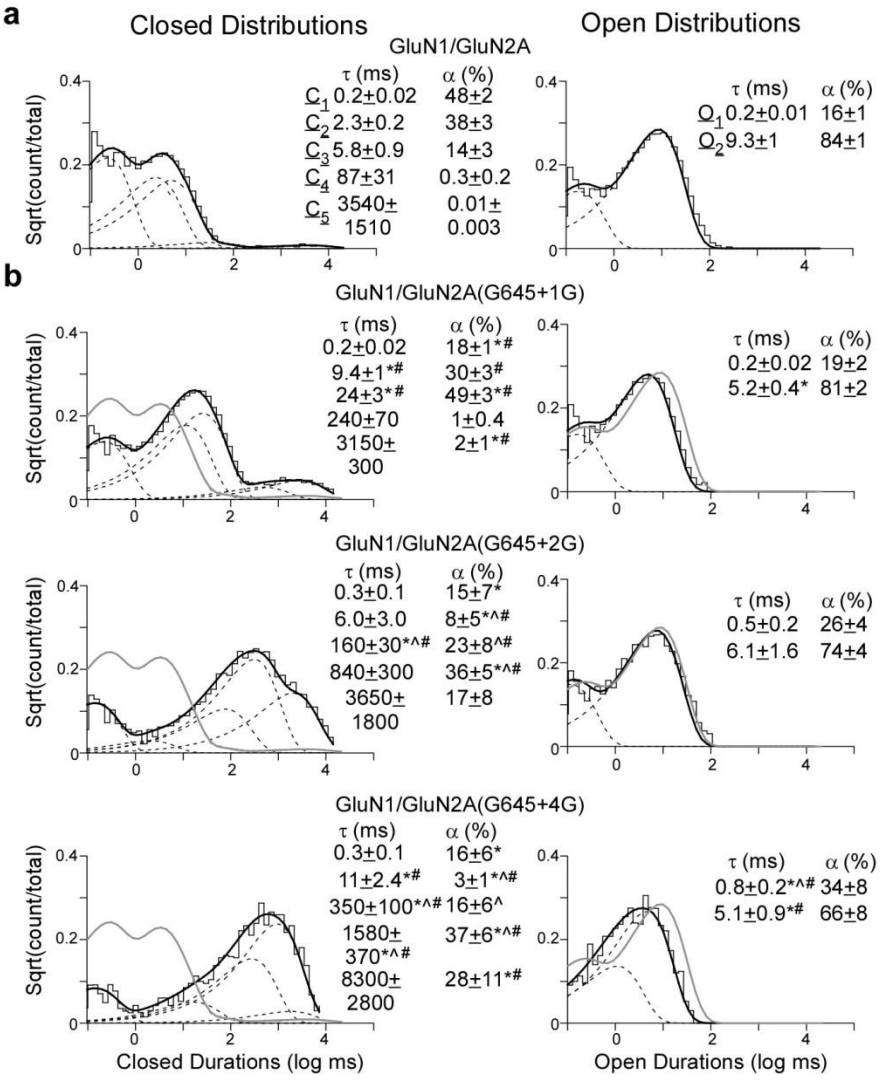

Supplementary Figure 2.6 Equilibrium open and closed time distributions for wild type and GluN2A insertion manipulations (relates to Fig. 2.6)

Figure is same as Supplementary Fig. 2.6 but for insertions in the GluN2A subunit.

	Total Events	*i* (pA)	P_o	MCT (ms)	MOT (ms)
GluN1/GluN2A	1,565,000 (8)	-7.3 ± 0.4	0.67 ± 0.06	4.3 ± 0.8	9.0 ± 0.9
GluN1					
G648+1G	1,515,000 (8)	-7.6 ± 0.4	0.36 ± 0.06*	10 ± 1.5*	4.9 ± 0.6*
I646+1G	870,000 (5)	-7.3 ± 0.2	0.29 ± 0.03*	7.3± 0.8*	2.7 ± 0.2*^
E644+1G	820,000 (4)	-9.9 ± 0.5*^	0.27 ± 0.05*	9.9 ± 1.4*	3.1 ± 0.4*^
GluN2A					
G645+1G	225,000 (6)	-7.8 ± 0.3	0.08 ± 0.02*	86.8 ± 30*	4.5 ± 0.4*
D641+1G	26,600 (3)	-10.6 ± 1.1	0.01 ± 0.009*^	510 ± 310	2.4 ± 0.5*^
F639+1G	54,000 (3)	-10.2 ± 0.2*^	0.02 ± 0.007*^	260 ± 160	2.3 ± 0.1*^
E637+1G	18,900 (3)	-12.7 ± 0.4*^	0.003 ± 0.001*^	470 ± 140	1.2 ± 0.2*^

Supplementary Table 2.1 Insertions at different sites in the GluN1 or GluN2A M3-S2 linkers reduce NMDAR pore opening (relates to Fig. 2.4)

Mean values (± SEM) for single-channel current amplitude (*i*), equilibrium open probability (P_o), mean closed time (MCT), and mean open time (MOT). GluN1 and GluN2A subunits containing insertions (bold) were coexpressed with wild type GluN2A and GluN1, respectively. Single-channel recordings were analyzed in QuB (see Materials and Methods). Number of patches is in parenthesis to the right of total events. P_o is the fractional occupancy of the open states in the MIL fitted single-channel recordings, including long lived closed states. All data was idealized and fit at a dead time of 0.075 ms.

For this and all subsequent Tables and Figures in the Supplementary Information, a significant difference is indicated relative either to GluN1/GluN2A (*); to like manipulations (e.g., single glycine insertions) between subunits [e.g., GluN1(G648+1G)/GluN2A versus GluN1/GluN2A(G645+1G)] ($^{\#}$); or to the single glycine insertions within subunits [e.g., GluN1(G648+1G)/GluN2A versus GluN1(G648+2G)/GluN2A] (^) ($p < 0.05$, two-tailed Student's t-test, unpaired) (see Materials and Methods).

	Total Events	*i* (pA)	P_o	MCT (ms)	MOT (ms)
GluN1/GluN2A	1,494,000 (8)	-7.2 ± 0.4	0.67 ± 0.05	5.5 ± 1.0	11.8 ± 1.3
GluN1					
G648+1G	1,260,000 (8)	-7.7 ± 0.4	0.36 ± 0.06*	11 ± 1.7*	5.7 ± 0.7*
G648+1A	580,000 (6)	-8.8 ± 0.2	0.14 ± 0.02*^	22 ± 2.6*^	3.2 ± 0.3*^
G648+1S	310,000 (3)	-7.7 ± 0.6	0.12 ± 0.06*^	34 ± 12	2.9 ± 0.6*^
GluN2A					
G645+1G	225,000 (6)	-7.8 ± 0.3	0.08 ± 0.02*	86.8 ± 30*	4.5 ± 0.4*
G645+1A	16,000 (4)	-7.8 ± 1.1	0.01 ± 0.001*^	630 ± 70*^	3.6 ± 0.3*^
G645+1S	4,700 (3)	-9.1 ± 0.2*	0.01 ± 0.002*^	260 ± 160*^	5.5 ± 0.7*

Supplementary Table 2.2 Different amino acid insertions reduce open probability (relates to Fig. 2.4)

Table caption is the same as that for Supplementary Table 2.1 except that the dead time for this analysis was 0.15 ms resulting in a reduced number of events for wild type.

	Total Events	*i* (pA)	P_o	MCT (ms)	MOT (ms)
GluN1/GluN2A	1,565,000 (8)	-7.3 ± 0.4	0.67 ± 0.06	4.3 ± 0.8	9.0 ± 0.9
GluN1					
G648+1G	1,515,000 (8)	-7.6 ± 0.4	0.36 ± 0.06*	10 ± 1.5*	4.9 ± 0.6*
G648+2G	376,000 (6)	-11 ± 0.8*^	0.14 ± 0.05*^	16.2 ± 4.4*	1.8 ± 0.8*^
G648+4G	472,000 (4)	-12 ± 0.7*^	0.13 ± 0.02*^	15.7 ± 2.3*	2.1 ± 0.1*^
GluN2A					
G645+1G	225,000 (6)	-7.8 ± 0.3	0.08 ± 0.02*	86.8 ± 30*	4.5 ± 0.4*
G645+2G	13,300 (-5)	-9.0 ± 1.4	0.008 ± 0.002*^	620 ± 80*^	4.9 ± 1.1
G645+4G	13,700 (6)	-11.3 ± 0.9*^	0.003 ± 0.001*^	3050 ± 860*^	3.6 ± 0.3*

Supplementary Table 2.3 Additional insertions in the M3-S2 linker further curtail pore opening (relates to Fig. 2.5)

Table caption is the same as that for Supplementary Table 2.1.

		C_3-C_2	C_2-C_1	C_1-O_1	C_4-C_3	C_5-C_2	O_1-O_2
GluN1/	k_f	230±34	702±36	2930±340	0.5±0.1	35±14	3930±310
GluN2A	k_r	37±7	2020±190	1210±150	4.5±1.1	2.3±0.9	570±47
	k_{eq}	7.1±0.8	0.4±0.03	2.6±0.3	0.1±0.04	15.9±3	7.1±0.7
	ΔG	-1.1±0.06	0.6±0.04	-0.5±0.07	1.3±0.2	-1.5± 0.2	-1.1±0.07
GluN1							
G648+1G	k_f	198±23	820±54	2090±270	0.4±0.05	36±11	3440±420
	k_r	32±3.7	2740±230*	1530±220	6.5±1.1	1.8±0.6	810±80*
	k_{eq}	6.5±0.8	0.3±0.03	1.4±0.2*	0.07±0.01	20.4± 5.0	4.5±0.6*
	ΔG	-1.1±0.06	0.7±0.05	-0.2±0.08*	1.6±0.09	-1.6± 0.2	-0.8±0.09*
G648+2G	k_f	170±24	1050±60*^	1440±280*	0.6±0.2	20±10	3940±580
	k_r	30±4.5	4420±320*^	2660±350*	6±1.1	1.1±0.3	1680±230*^
	k_{eq}	6±0.6	0.2±0.02*	0.5±0.09*^	0.07±0.01	14.0± 4.5	2.7±0.7*^
	ΔG	-1.0±0.06	0.8±0.06*	0.4±0.09*^	1.4±0.2	-1.4± 0.2	-0.5±0.2*
G648+4G	k_f	170±31	1030±25*^	1940±82*	0.4±0.06	22±12	4780±270^
	k_r	40±9.8	5380±360*^	3480±105*^	2.6±0.8^	2.0±0.9	1140±85*^
	k_{eq}	4.3±0.4*^	0.2±0.01*^	0.6±0.03*^	0.2±0.08	13.2± 3.6	4.2±0.2*
	ΔG	-0.8±0.1*^	1±0.03*^	0.3±0.03*^	1.1±0.3	-1.4± 0.2	-0.8±0.02*
GluN2A							
G645+1G	k_f	52±13*#	320±20*#	900±50*#	0.4±0.05	21±14	3590±370
	k_r	14.3±3*#	3170±300*	1440±230	6.1±1.4	4.6±3.6	830±67*
	k_{eq}	3.5±0.4*#	0.1±0.02*#	0.7±0.1*#	0.09±0.02	9.3±5.3	4.4±0.6*
	ΔG	-0.7±0.06*#	1.3±0.1*#	0.2±0.1*#	1.5±0.1	-1.0 ±0.2	-0.9±0.08*
G645+2G	k_f	93±45	140±40*^#	630±190*#	0.6±0.2	3.7±1.5	2400±1300
	k_r	210±87	4330±1420	1040±360#	0.8±0.3*^#	36±32	620±120#
	k_{eq}	0.6±0.2*^#	0.1±0.06*	0.8±0.3*	3.6±2.5	1.0± 0.5*#	3.9±1.8
	ΔG	0.5±0.3*^#	1.9±0.4*#	0.3±0.2*	-0.2± 0.4*^#	0.6±0.6*#	-0.4±0.4
G645+4G	k_f	34±8.0*#	36±7.7*^#	530±100*^#	0.4±0.1	3.3±1.4	1010±580*^#
	k_r	120±63	3800±980	750±210#^	0.4±0.2*^	6.4±3.9	570±100#
	k_{eq}	1.2±0.8*^#	0.01± 0.003*^#	1.0±0.3*	7.9±7.2	0.2± 0.04*#	1.5±0.6*^#
	ΔG	0.5±0.4*^#	2.7±0.2*^#	0.2±0.2*	-0.1± 0.4*#	1.4± 0.4*^#	0.1±0.3*^#

Supplementary Table 2.4 Insertions alter activation kinetic rate constants (relates to Fig. 2.6)

Mean values (± SEM) for forward (k_f) and reverse (k_r) equilibrium kinetic rate constants (s^{-1}) for a 5C-2O kinetic scheme (Fig. 2.6).ΔG is in units of kcal/mol. Kinetics models were constructed as C_3-C_2-C_1-O_1-O_2 while C_4 and C_5 branched from C_3 and C_2, respectively (see Materials and Methods). C_4 and C_5 reflect the desensitized states.

CHAPTER 3: ASYNCHRONOUS MOVEMENTS PRIOR TO PORE OPENING IN NMDA RECEPTORS

INTRODUCTION

In iGluR subunits, the extracellular ligand-binding domain (LBD) is comprised of two discontinuous polypeptides (S1 and S2) (Armstrong and Gouaux, 2000; Furukawa et al., 2005; Mayer, 2006). The transmembrane domain (TMD), which forms the ion channel, is composed of three transmembrane helices (M1, M3, & M4) and a re-entrant pore-loop (M2) (Sobolevsky et al., 2009). In iGluRs, opening of the ion channel entails shifting of the major pore-lining M3 helices away from the central axis of the pore (Fig. 3.1) (Jones et al., 2002; Sobolevsky et al., 2002; Chang and Kuo, 2008; Sobolevsky et al., 2009), presumably driven by the M3-S2 linkers, the short polypeptide linkers that connect the M3 helices to the LBD (Sun et al., 2002; Hansen et al., 2007). In the GluA2 structure, where the ion channel is closed, the centrally-located M3 helices and M3-S2 linkers are surrounded by the M1 and M4 helices and the linkers, S1-M1 and S2-M4, that connect them to the LBD (Fig. 3.1) (Sobolevsky et al., 2009). Functional experiments have shown that these peripheral structural elements can modulate gating (Krupp et al., 1998; Balannik et al., 2005; Schmid et al., 2007; Talukder et al., 2010; Ren et al., 2012). Given the tight physical association between the peripheral helices and linkers and the central gating structures, these peripheral elements presumably must reposition for efficient channel gating to occur (Sobolevsky et al., 2009). This idea remains untested. Further, the temporal relationship between the dynamics of these peripheral elements and pore opening remains unknown.

To address the dynamics of these peripheral structural elements in NMDA receptors, we constrained the relative movement of the S1-M1 and S2-M4 linkers, either in an intra- (within

GluN1 or GluN2A) or inter- (between GluN1 and GluN2A) subunit fashion using disulfide cross-links. For either intra- or inter-subunit constraints, gating was significantly impaired, highlighting the requirement for a rearrangement of these peripheral structural elements for efficient gating to occur. Surprisingly, however, we also find that the relative movements between different pairs of peripheral linkers are not temporally equivalent, indicating an asynchrony in the sequence of events from agonist binding to pore opening. Hence, although the overall gating process is largely concerted across the four subunits, elementary events occur in a step-wise fashion. Targeting these events may represent a means to modulate NMDA receptors clinically.

MATERIALS AND METHODS

Mutagenesis and Expression

Cysteine substitutions in rat GluN1a (NCBI Protein database accession no. P35439) and GluN2A (accession no. Q00959) subunits were generated using QuickChange site-directed mutagenesis kit (Stratagene, La Jolla, CA.) (Yelshansky et al., 2004). *Xenopus laevis* oocytes were prepared, co-injected with cRNA encoding GluN1a and GluN2A, and maintained as previously described (Sobolevsky et al., 2002). Macroscopic current recordings were made 3-4 days after the injection. For mammalian cell expression, human embryonic kidney (HEK) 293 cells were co-transfected with cDNA encoding GluN1 and GluN2A, as well as a vector for enhanced green fluorescent protein (pEGFP-Cl; Clonetech) at a ratio of 1:1:1 using Fugene 6 (Roche). Single-channel recordings were made 24-48 hours following transfection.

Macroscopic current recordings and analysis

Macroscopic currents from *Xenopus* oocytes were recorded using two-electrode voltage clamp (TEVC-200A; Dagan Corporation) with Cell Works software (npi electronic GmbH) at room temperature (20-23 °C). Microelectrodes were filled with 3M KCl and had resistances of 1-4 MΩ. The external solution ("Bath Solution") consisted of (in mM): 115 NaCl, 2.5 KCl, 0.18 $BaCl_2$, 5 HEPES and 100 µM EDTA (pH 7.2, NaOH). All reagents including glycine (20 µM) and glutamate (200 µM), competitive antagonists 5,7-dichlorokynurenic acid (DCKA, 10 µM) and DL-2-amino-5-phosphonopentanoic acid (APV, 100 µM), as well as the reducing agent dithiothreitol (DTT, 4 mM) were applied with the bath solution. All reagents were obtained from Roche or Sigma-Aldrich.

To assay the effects of DTT on macroscopic currents in oocytes, we calculated the percent potentiation (*% potentiation*) in agonist-activated current amplitude, $(I_{post} - I_{pre})/I_{pre}$ x

100, measured before (I_{pre}) and either during or after (I_{post}) a DTT application. I_{pre} and I_{post} were averages of amplitudes of currents elicited by three to five 15 s applications of glutamate and glycine separated by 45-60 s washes in agonist-free solution. Corrections for current run-down over time were calculated by fitting a single-exponential curve to at least three pre-DTT agonist-activated current amplitudes. All analysis was performed using Igor Pro (WaveMetrics) with in lab written programs as previously published (Sobolevsky et al., 2002; Talukder et al., 2010).

DTT was applied in one of two ways. For screening proximal positions using pairs of introduced cysteines, we applied DTT continuously for approximately five minutes while measuring I_{post}. The advantage of this protocol is the lack of possible bias due to state-dependent action of DTT since receptors visited both the open and closed states when exposed to DTT. Alternatively, for experiments to assay properties of DTT-induced current potentiation, we applied DTT for 120 s in an agonist-free solution containing competitive antagonists DCKA and APV, and measured I_{post} after removal of DTT and antagonists. This latter protocol greatly improved oocyte health (as evidenced by reduced changes in the baseline current amplitude and increased survivability during recordings).

Protein chemistry

Whole cell membrane proteins were isolated as described previously (Salussolia et al., 2011b). Briefly, ten to twelve healthy oocytes expressing wild-type GluN1/GluN2A receptors or cysteine-substituted subunits were fixed in PBS containing 58 mM N-ethylmaleimide (NEM, Pierce), lysed (20 mM Tris, 0.58 mM NEM) and centrifuged. The supernatant was recovered and ultracentrifuged at 40,000 RPM (Beckman TLA 120.2 rotor) for 10 min. The pellet was resuspended in PBS and ultracentrifuged again at 40,000 RPM. The resultant pellet was re-suspended in solubilization buffer (20 mM Tris, 50 mM NaCl, 1/1000 protease inhibitor cocktail

(Sigma), and 0.58 mM NEM) without detergent and then incubated with detergents (0.03% Na-deoxycholate, 1% Triton X-100) at 4°C for 1 hr. Solubilized proteins were ultracentrifuged for 20 min at 40,000 RPM and membrane proteins contained in the supernatant were separated by SDS-PAGE under non-reducing or reducing (100 mM DTT) conditions.

Proteins were transferred from the gel to 0.45 mm nitrocellulose membranes by semi-dry transfer (BioRad) using Bjerrum-Schaffer-Nielsen buffer. Blots were blocked and incubated with either mouse anti-GluN1 (1:500; Millipore MAB363) or rabbit anti-GluN2A (1:300; Millipore AB1555P) overnight at 4°C. Blots were washed prior to incubation with HRP-conjugated goat anti-mouse (sc-2302) or HRP-conjugated goat anti-rabbit (sc-2030) and developed with Western Blot Luminol Reagent (sc-2048, all Santa Cruz Biotechnology reagents) and exposed to chemiluminescence film (Crystalgen, Blue Sensitive Film, CGFB-507).

Single-channel recordings and analysis

All single-channel recordings were performed in the "on-cell" configuration at steady state using transfected HEK 293 cells. The pipette solution used (mimicking extracellular agonist conditions) contained (in mM): 150 NaCl, 10 HEPES, 1 EDTA, 1 glutamate, and 0.1 glycine, pH 8.0 (NaOH). The high pH and EDTA were used to minimize proton and divalent mediated inhibitory effects, respectively (Popescu and Auerbach, 2003; Kussius and Popescu, 2009; Talukder et al., 2011). Recording pipettes were pulled from thick-wall borosilicate capillary glass (Sutter Instruments) and fire-polished to final pipette resistances ranging from 5-50 MΩ when measured in the bath solution (with an applied positive pipette pressure of approximately 200 mbar). Cells were identified by GFP fluorescence and patched to resistances exceeding 1.5 GΩ. To elicit distinct inward current amplitudes, we held the electrode voltage at +100 mV. Currents were recorded using a patch clamp amplifier (Axopatch 200B; Molecular

Devices), filtered at 10 kHz (four-pole Bessel filter), and digitized at 40 kHz (ITC-16 interfaced with PatchMaster). Experiments ran for approximately 15-20 min to ensure a significant number of events for analysis. To assay the effects of DTT on single-channel activity, we applied 4 mM DTT in both the bath (prior to forming the gigaseal) and pipette solutions (Talukder et al., 2011).

Analysis of single-channel records was comparable to Talukder and Wollmuth, 2011. Briefly, after recordings were complete, data was exported from PatchMaster to QuB (http://www.qub.buffalo.edu) for analysis. Recordings of GluN1/GluN2A receptors without DTT and all receptors with DTT consisted of long clusters of activity separated by seconds-long periods of inactivity, simplifying detection of several channels in the patch. For these recordings, the relatively high open probability (P_o) and duration of recordings (~ 90,000-1,000,000 events) indicated that we were recording from single-channel patches.

For several cross-linked constructs, the P_o without DTT was extremely low which made single-channel patches detection difficult. First, many patches were recorded but excluded during analysis because of obvious simultaneous openings of multiple channels. Of the remaining patches, only minutes-long recordings (with 13,000-100,000 events) without any apparent simultaneous openings were further analyzed. Of the single-channel P_o values tabulated, the lowest was 0.002 for GluN1(F540C)/GluN2A(S791C). If the patch contained two active channels of equivalent open probability, then a double-channel opening would be expected approximately once every 500 events (Colquhoun and Hawkes, 1990b; Dravid et al., 2008). On average, enough events were recorded to be approximately 99% confident that activity was from a single channel (analysis not shown). For GluN1(F540C)/GluN2A(S791C), two patches contained too few events to be completely confident that there was only a single channel but

these two records had open probabilities less than the average P_o observed for this receptor. Hence, we assume that there was not more than one channel in these patches.

Processed data was idealized using the segmental k-means (SKM) algorithm . Kinetic analysis was performed using the maximum interval likelihood (MIL) algorithm in QuB with a dead time of 150 μs. Kinetic models of NMDA receptor gating activation have been proposed to contain approximately 5 closed states and more than one open state (Banke and Traynelis, 2003; Popescu and Auerbach, 2003; Auerbach and Zhou, 2005; Schorge et al., 2005; Erreger and Traynelis, 2008). We used a linear, fully-liganded state model containing 3 closed states, 2 desensitized states and 2-4 open states (Auerbach and Zhou, 2005; Kussius and Popescu, 2009).

In the present study, we investigated five receptor types, wild type and 4 receptors containing double cysteine-substitutions, using single channel analysis. Each receptor was studied either in the absence or presence of DTT. For each individual record, state models with increasing closed (3 to 6) and open (2 to 4) states were constructed and fitted to the recordings until log-likelihood (LL) values improved by less than 10 LL units/added state or if the next added state showed 0% occupancy (Kussius and Popescu, 2009; Talukder and Wollmuth, 2011). For closed-time distribution, all receptors except for one [GluN1(S531C-F792C)/GluN2A] was best fit by 5 closed states. For GluN1(S531C-F792C)/GluN2A in the absence of DTT, 4 out of 5 recordings were best fit by 6 closed states, but the 6^{th} component displayed an occupancy of <0.01%, suggesting that it was a minor component of gating.

The open-time components, comprising one common short duration (O_1) and up to three long duration (O_2-O_4) intervals arise from modal gating of NMDA receptors (Kussius and Popescu, 2009). For each individual record, we initially fit open time distributions with 2-4 open states. In the presence of DTT, the open time distributions were best fit by 4 open states for all

receptors studied. In the absence of DTT, where the probability of being open was extremely low for certain cysteine-substituted receptors, some individual records were best fit by only 2 or 3 open states though for each receptor there were examples of best fits with 4 open states (typically those with very long recording times where many events were present). As such, we could not confidently perform statistical analysis regarding modal gating (4 open states). We therefore fit all open-time distributions with only two open components, a short-duration open state (O_1) and a single "long-duration" open state (O_2) (Kussius and Popescu, 2009; Kussius et al., 2010; Borschel et al., 2011; Talukder and Wollmuth, 2011). Time constants and the relative areas of each component, the transition rate constants, as well as mean closed time (MCT) and mean open time (MOT) were averaged for each receptor without and with DTT and compared with each other.

Thermodynamic effect of constraining linker mobility

We quantified the Gibbs free energy of each transition using:

Eq. 3.1

$$\Delta G = -RT\ln(\frac{K_f}{K_r})$$

where K_f and K_r refer to the forward and reverse rates of that transition, R is the empirical gas constant ($1.987x10^{-3}$ kcal/mol), and T is the recording temperature (295 Kelvin). To assay the thermodynamic effect of constraining linker mobility via cross-linking, we quantified differences in energy for each kinetic transition between the DTT (ΔG_{+DTT}) and non-DTT (ΔG_{-DTT}) conditions:

Eq. 3.2

$$\Delta\Delta G = \Delta G_{+DTT} - \Delta G_{-DTT}$$

Statistics

Data analysis and statistics was performed using IgorPro (WaveMetrics), QuB, Excel (Microsoft) and SAS 9.3 (SAS). Whole-cell and single-channel current amplitudes and single-channel properties are presented as mean ± SEM. We used a two-tailed Student's t-tests to test if the degree of DTT-induced potentiation was greater than that for wild-type (for macroscopic currents) and to test significant differences between single-channel properties for cysteine-substituted receptors and wild-type under the various conditions (+/- DTT). Student's t-test was also used to test for a significant difference in ΔG values between +DTT and –DTT conditions for GluN1/GluN2A. Statistical significance was set at $p < 0.05$.

Statistical differences for thermodynamic effects of cross-linking were defined as follows (Stony Brook Biostatistics Core Facility): A three way ANOVA model was used to model experimental data with receptor, kinetic transition, and DTT condition. Their two- and three-way interactions were also included in the model. Normality assumption was confirmed. This model allows us to test different linear contrasts and t-test was used to test if any linear contrast is statistically different from 0. The hypothesis being tested here is whether the $\Delta\Delta G$ value differ between two different kinetic transitions for a specific construct (e.g. between the C3-C2 transition and the C2-C1 transition of GluN1(S531C-F792C)/GluN2A) or between two different constructs for a particular kinetic transition (e.g. between GluN1(S531C-F792C)/GluN2A and GluN1/GluN2A for the C3-C2 transition). Because we were interested in the significance level of each hypothesis (comparison), we did not use a multiple comparison adjustment. Statistical significance was set at $p < 0.05$ and performed using SAS 9.3, Cary, NC.

RESULTS

To study the dynamics of the peripheral linkers, S1-M1 and S2-M4, during NMDA receptor gating, we constrained their mobility using spontaneously formed disulfide bonds between pairs of introduced cysteines. Initially, we designed experiments to identify intra- and inter-subunit pairs of positions between S1-M1 and S2-M4 that form disulfide bonds when substituted with cysteine. Identification of intra- and inter-subunit cross-linking between S1-M1 and S2-M4 linkers in NMDA receptor subunits

To identify intra-subunit proximal pairs between S1-M1 and S2-M4, we chose S531 in the S1-M1 of GluN1 (Fig. 3.2A) and V525 in the S1-M1 of GluN2A (Fig. 3.2B) as reference points (Talukder et al., 2010) and screened multiple positions for potential cross-linking partners in the S2-M4 linker of the same subunit (T789 to M795 in GluN1, Fig. 3.2A and Q792 to M798 in GluN2A, Fig. 3.2B). Proximal positions to the reference points were selected based on homologous residues in the AMPA receptor GluA2 structure (Sobolevsky et al., 2009). Nevertheless, using the LBD-TMD linkers of AMPA receptors as a model for those in NMDA receptor subunits has limitations since they differ in length (note dashes in alignments in Figs. 3.2A & 3.2B) (Sobolevsky et al., 2009; Talukder et al., 2010; Traynelis et al., 2010).

For the reference point GluN1(S531), only GluN1(S531C-F792C)/GluN2A showed a significantly greater potentiation of agonist-activated current amplitudes during DTT exposure (660 ± 360%, n = 8, mean ± SEM, number of recordings) than wild-type GluN1/GluN2A (27 ± 4%, n = 11) (Figs. 3.2C & 3.2E). For the reference point GluN2A(V525), receptors containing cysteine substitutions at three S2-M4 positions (Q792, D794 or D796) showed significantly greater DTT-induced current potentiation (63 ± 6.7%, n = 4; 390000 ± 150000%, n = 4; 320 ± 16%, n = 4; respectively) than wild-type (Figs. 3.2D & 3.2F).

To identify inter-subunit proximal pairs, we used S791 in S2-M4 of GluN2A and P787 in S2-M4 of GluN1 as reference points and screened for proximal positions in the S1-M1 of the opposite subunit (M537 to T543 in GluN1, Fig. 3.3A and F534 to S537 in GluN2A, Fig. 3.3B, respectively). For the reference point GluN2A(S791), the only pair of cysteines showing a significantly greater DTT-induced current potentiation than wild-type was GluN1(F540C)/GluN2A(S791C) (290 ± 6%, n = 3) (Figs. 3.3C & 3.3E). For the reference point GluN1(P787), receptors containing cysteine substitutions at three positions in the S1-M1 of GluN2A (F534, S535 and A536) showed significantly greater DTT-induced current potentiation (440 ± 47%, n = 4; 730 ± 190%, n = 4; 21000 ± 1500%, n = 4; respectively) than wild-type (Figs. 3.3D & 3.3F). DTT-induced current potentiation is due to breakage of a disulfide bond between introduced cysteines

For subsequent experiments, we focused on four pairs of positions ('focal pairs'): two intra-subunit, GluN1(S531C-F792C) and GluN2A(V525C-D796C) and two inter-subunit, GluN1(P787C)/GluN2A(S535C) and GluN1(F540C)/GluN2A(S791C). In some instances to refer to the focal pairs and to emphasize the location of the cross-linked pairs, we used abbreviations with the number indicating the most proximally connected transmembrane segment (1 for M1, 4 for M4): GluN1(1C-4C) for GluN1(S531C-F792C); GluN2A(1C-4C) for GluN2A(V525C-D796C); GluN1(1C)/GluN2A(4C) for GluN1(F540C)/GluN2A(S791C); and GluN1(4C)/GluN2A(1C) for GluN1(P787C)/GluN2A(S535C) (Fig. 3.4A). For these more focused experiments using macroscopic currents, we applied DTT for 120 s in the presence of competitive antagonists (DCKA and APV) (see Materials & Methods).

As illustrated in Figs 3.4B & 3.4C, DTT when applied in the presence of competitive antagonists significantly potentiated current amplitudes for GluN1(1C-4C)/GluN2A (640 ± 190

%, n = 6), GluN1/GluN2A(1C-4C) (350 ± 34 %, n = 6), GluN1(1C)/GluN2A(4C) (110 ± 4 %, n = 6) and GluN1(4C)/GluN2A(1C) (360 ± 49 %, n = 5) when compared to wild-type (6 ± 7 %, n = 5). In contrast, none of the receptors with only a single cysteine substitution showed significant DTT-induced current potentiation (Figs. 3.4B & 3.4C). These results are consistent with the idea that the DTT-induced current potentiation arises from breakage of cross-links between pairs of introduced cysteines in two different subunits rather than in two subunits of the same type (e.g., between S531C in two GluN1 subunits) or between introduced and endogenous cysteines (Fig. 3.4A).

To further test the idea that DTT-induced current potentiation reflects breakage of introduced disulfide bonds, we used immunoblots to analyze the focal pairs under either non-reducing (Fig. 3.4D) or reducing (Fig. 3.4E) conditions. Consistent with inter-subunit cross-linking, both GluN1(4C)/GluN2A(1C) and GluN1(1C)/GluN2A(4C) showed dimer bands when probed with either anti-GluN1 (Fig. 3.4D, left panel) or anti-GluN2A (Fig. 3.4D, right panel) antibodies. These heterodimers bands were absent under reducing conditions (Fig. 3.4E). On the other hand, GluN1(1C-4C)/GluN2A and GluN1/GluN2A(1C-4C) only showed monomer bands under non-reducing conditions, consistent with cross-linking occurring within an individual subunit rather than between like subunits.

Cross-links could have arisen during biogenesis but may not occur in the intact, functional receptor. Therefore, we tested the rate of spontaneous reformation of broken disulfide bonds using the decrease in whole-cell current amplitudes after removing DTT from the bath solution as an index of bond reformation (data not shown). For the four focal pairs, current amplitudes decreased after removing DTT with a time constant varying between 200 to 400 seconds depending on the constructs (data not shown). Hence the disulfide bonds broken by

DTT spontaneously reform in intact, functional receptors, suggesting that the receptor conformation(s) in which the introduced cysteines cross-link are visited in a surface-expressed functional receptor.

To quantify the effects of cross-linking on gating, we used single channel recordings in HEK 293 cells as presented in subsequent sections. For these recordings, we used a solution that was at pH 8.0 and contained EDTA (1 mM) (see Materials and Methods). In contrast, the oocyte solution was at pH 7.2, contained a small amount of Ca^{2+} (0.18 mM) and did not contain EDTA. These factors, pH and divalent composition, can have significant effects on NMDA receptor gating (Traynelis et al., 2010). Hence, we did not study the quantitative differences within the oocyte results nor did we compare these results to those in HEK 293 cells. Rather, we used the oocyte results only as a screen to identify cross-linking pairs of positions that would be further studied at the single channel level.

Constraining the peripheral linkers impedes NMDA receptor opening

To address the dynamics of the peripheral linkers during NMDA receptor gating, we measured single-channel activity for wild-type receptors and the receptors with focal pairs of introduced cysteines (Fig. 3.4A). Figure 3.5 illustrates single-channel activity for wild-type (A), as well as intra- (B & C) or inter- (D & E) subunit focal pairs. All recordings were from patches containing exactly one channel measured in the on-cell configuration and were recorded in either the absence (-DTT) (*left panels*) or presence (+DTT) (*right panels*) of DTT (see Materials & Methods). In the absence of DTT (Fig. 3.5, *left*), the intra- and inter-subunit cross-linked receptors showed dramatic reductions in single-channel activity compared to wild-type while maintaining its general gating properties (burst activity, a single conductance level, and variability in channel open time) (Popescu and Auerbach, 2003; Schorge et al., 2005). Under

reducing conditions (Fig. 3.5, *right*), all constructs, including wild-type, showed significant increases in channel activity, albeit to varying degrees.

Table 3.1 summarizes the single-channel results including current amplitude (*i*), equilibrium open probability (P_o), mean closed time (MCT), and mean open time (MOT) for wild-type and the four focal pairs. In the absence of DTT, both intra- and inter-subunit cross-linked constructs showed significant decreases in P_o relative to wild-type ($P_o = 0.71 \pm 0.04$, n = 7). The most dramatic reduction in P_o occurred for the receptors with inter-subunit focal pairs, where it was reduced to ~0.002 for GluN1(1C)/GluN2A(4C) and ~0.007 for GluN1(4C)/GluN2A(1C) (Table 3.1). Reductions in P_o were less dramatic for the receptors with intra-subunit focal pairs and the effects were highly subunit-specific with P_o being reduced to ~0.46 in GluN1(1C-4C)/GluN2A and to ~0.014 in GluN1/GluN2A(1C-4C). For all constructs, the drop in P_o could be largely accounted for by significant increases in MCT and decreases in MOT (Table 3.1).

Under reducing conditions (+DTT), wild-type as well as all focal pair receptors showed significant increases in P_o (relative to -DTT) with single-channel activity for most focal pair receptors approaching that of wild-type. A notable exception was GluN1(1C)/GluN2A(4C) where DTT cause a significant increase in P_o (~0.002 to ~0.04) but the +DTT P_o was 22-fold less than wild-type +DTT (~0.88). The reduced P_o in the +DTT condition for GluN1(1C)/GluN2A(4C) is likely due to one or both of the introduced cysteines themselves altering gating, an effect we do not explore further here. Nevertheless, our analysis of energetics will depend on the relative difference between the -DTT and +DTT conditions rather than the absolute gating properties in any one condition (see below). In this regard, focal pair receptors showed greater relative increases in P_o in the presence of DTT [increased 1.80-fold for N1(1C-

4C)/N2A; 62-fold for N1/N2A(1C-4C); 20-fold for N1(1C)/N2A(4C); and 92-fold for N1(4C)/N2A(1C)] than wild-type (1.14-fold) suggesting that a major effect of DTT is the removal of constraints caused by the introduced cross-links. In summary, these results suggest that constraining the peripheral linkers, either in an intra- or inter-subunit fashion, strongly impedes NMDA receptor gating indicating that a repositioning of these linkers is required for efficient gating. Further, the reduced *P*o values shown by the constrained receptors were the result of both increases in MCT and decreases in MOT (Table 3.1). Hence, regions outside of the central pore axis can affect the relative stability of the closed and open states (Schmid et al., 2007; Talukder et al., 2010; Ren et al., 2012)

Kinetic analysis of single-channel recordings

To address how the intra- and inter-subunit constraints alter the energetics of gating, we performed kinetic and thermodynamic analyses on our single-channel results. Figure 3.6A shows closed (*upper panel*) and open (*lower panel*) duration histograms and associated exponential fits (smooth lines) for wild-type GluN1/GluN2A either in the absence either in the absence (black) or presence (gray) of DTT. For wild-type, 5 closed states best fit the data, as has been found previously (Wyllie et al., 1998; Auerbach and Zhou, 2005; Kussius and Popescu, 2009). Wild-type GluN1/GluN2A shows modal gating consisting of a brief open state and three longer lived open states (referred to as O_2, O_3, and O_4) (Popescu and Auerbach, 2003). For our recordings, open distributions of wild-type were also best fit with four open states as were those for many individual records for the focal cysteine pairs (see Materials and Methods). However, in the absence of DTT, long duration openings were not always observed for receptors with focal cysteine pairs. We therefore fit open time histograms with just two open states, a brief open state

(O_1) and a longer duration open state (O_2). Closed and open state occupancies (α) and time constants (τ) are shown in Tables 3.2 and 3.3, respectively.

Figure 3.6B illustrates kinetic schemes (*upper panels*) and the resultant energy landscapes (*lower panels*) for wild-type GluN1/GluN2A recorded either in the absence (*left panels*) or presence (*right panels*) of DTT. For wild-type, as well as all four focal pairs, we used a kinetic model consisting of 5 closed and 2 open states (Kussius and Popescu, 2009; Talukder et al., 2011) which consists of a linear, "intraburst" C_3-C_2-C_1 activation sequence with two off-pathway states (C_5 and C_4, connected to C_3 and C_2, respectively) presumably representing desensitized states. In series with the C_1 closed state is the brief O_1 open state from which an additional, long duration O_2 state arises (Popescu and Auerbach, 2003; Auerbach and Zhou, 2005) (see Discussion in terms of kinetic model used).

Kinetic effects of constraining the GluN1 or GluN2A peripheral linkers on receptor gating

Figure 3.7 illustrates closed and open duration fits (A & C), kinetic schemes (B & D, *upper panels*) and the resultant energy landscapes (*lower panels*) for the two intra-subunit focal pairs, GluN1(1C-4C)/GluN2A (A & B) and GluN1/GluN2A(1C-4C) (C &D). Receptors were recorded either in the absence (*left panels*) or presence (*right panels*) of DTT. The kinetic rate constants for receptors containing the intra-subunit focal pairs in the absence of DTT showed widespread differences from wild-type (Fig. 3.7B & 3.7D, *left column*). In general, the most notable difference was a significant reduction in the rates approaching the O_1 state with these effects consistently stronger in GluN2A(1C-4C). The reverse transition (O_1-C_1) was also significantly faster for receptors with intra-subunit focal pairs, suggesting that the separation of these peripheral linkers may stabilize the open state. In the presence of DTT, these forward rates

were increased and were generally comparable to those for wild-type + DTT (Fig. 3.7B & 3.7D, *right column*).

Intra-subunit constraints of the peripheral linkers restrict late gating transitions.

We initially constructed energy landscapes for each receptor under the different conditions (Figs. 3.7B-3.7D, *lower panels*). In parallel with the kinetic rates, the difference in energy levels and barriers is greater for GluN1/GluN2A(1C-4C) (Fig. 3.7D, *lower panel*) than for GluN1(1C-4C)/N2A (Fig. 3.7B, *lower panel*) when compared with the wild-type landscape (Figs. 3.7B-3.7D, *lower panels*, thick lines). On the other hand, in the presence of DTT (Figs. 3.7B & 3.7D, *right panels*), the landscapes have a generally similar profile, agreeing with the kinetic analysis.

The results presented so far highlight the effects of the intra-subunit constraints on reducing the efficacy of NMDA receptor gating. However, they do not quantify the energetic effects of constraints on specific kinetic transitions which depend on the difference in transition energy between the -DTT and +DTT conditions and must also consider the endogenous effects of DTT on GluN1/GluN2A receptors [e.g.,(Talukder et al., 2011)](Fig. 3.6B). We therefore compared the free energy difference, referred to as ΔΔG, between the –DTT (ΔG_{-DTT}) and +DTT (ΔG_{+DTT}) conditions for each cysteine-substituted receptor to that of GluN1/GluN2A for each kinetic transition (significant differences highlighted by a '$' in each subsequent figure). To distinguish temporal effects on gating by the constraints, we compared ΔΔG values across different transitions for each individual receptor (highlighted by a '‡' in each subsequent figure). Lastly, as presented in a subsequent section, we directly compared ΔΔG values between individual pairs of cysteine-substituted receptors to determine construct-specific differences. An advantage of this approach of comparing the difference between +DTT to -DTT in terms of

energetic effects is that it compensates for any effect an individual cysteine substitution might have on receptor gating. For all of the above analyses, we focused on the direct pathway leading to channel opening (C_3-C_2-C_1-O_1) and not on O_1-O_2 or off pathways (C_3-C_5 & C_2-C_4) because of the limited number of events for these transitions, obscuring accurate analysis.

Previous studies have shown that the major endogenous effect of DTT on GluN1/GluN2A receptors is to increase the occupancy of long-lived open states (Talukder et al., 2011). In terms of energetic effects (Fig. 3.7E), this increase in occupancy is manifested as a significant difference in energy between the –DTT and +DTT conditions for only the O_1-O_2 transition (highlighted by a '*'). Because this reaction became more energetically favorable in the presence of DTT, it is manifested as a negative $\Delta\Delta G$.

Intra-subunit constraints of the peripheral linkers in either GluN1 or GluN2A showed no energetic effect on the early C_3-C_2 gating transition (Fig. 3.7E). However, for GluN1/GluN2A(1C-4C), $\Delta\Delta G$ values were significantly different from wild type for the C_2-C_1 and C_1-O_1 transitions. Further, for GluN1/GluN2A(1C-4C), the C_2-C_1 and C_1-O_1 $\Delta\Delta G$ values were significantly different from that of the C_3-C_2 transition, highlighting a potential temporal dependence for movements of the GluN2A peripheral linkers. The constraint in the GluN1 subunit [GluN1(1C-4C)/GluN2A] also restricted gating transitions approaching channel opening, but the $\Delta\Delta G$ values were only significantly different from wild-type for the C_1-O_1 transition. Hence, the physical constraint between the peripheral linkers in the GluN1 and GluN2A subunits significantly restrict gating transitions nearing the open state but they do not appear to be equivalent in their actions.

Inter-subunit constraints of the peripheral linkers have widespread effects on gating transitions.

Figure 3.8 illustrates closed and open duration fits (A & C), kinetic schemes (B & D, *upper panels*) and energetic landscapes (*lower panels*) for receptors with inter-subunit focal pairs of cysteines, GluN1(1C)/GluN2A(4C) (A & B) and GluN1(1C)/GluN2A(4C) (C & D). Similar to the intra-subunit focal pairs, the forward rate constants approaching channel opening for the inter-subunit focal pairs were significantly reduced and the reverse O_1-C_1 rate constant was significantly increased relative to wild type. All of the forward rates significantly increased in the +DTT condition, except for the forward C_1-O_1 transition for GluN1(1C)/GluN2A(4C). This GluN1(1C)/GluN2A(4C) construct showed a low P_o even in the presence of DTT (Table 3.1) which presumably reflects an effect of the cysteine substitutions themselves. The most notable feature of this construct is the large decrease in the reverse O_1-C_1 transition suggesting a potential role of these linkers in stabilizing the open state.

The energy landscapes (Figs. 3.8B & 3.8D, lower panels) highlight the strong energetic effects of the inter-subunit constraints across all gating transitions. Superficially, because they are scaled the same, these landscapes highlight the differences between the intra- and inter-subunit constraints of the peripheral linkers (cf., Figs. 3.7B & 3.7D). Not surprisingly, DTT only weakly altered the energy landscape for GluN1(1C)/GluN2A(4C).

Figure 3.8E summarizes the energetic effects on gating arising from inter-subunit constraints of the peripheral linkers. For GluN1(1C)/GluN2A(4C), there was a significant difference in $\Delta\Delta G$ relative to wild-type only during the C_3-C_2 transition. On the other hand, for GluN1(4C)/GluN2A(1C), the $\Delta\Delta G$ values were significantly different relative to wild-type for each transition prior to opening. In addition, $\Delta\Delta G$ values were significantly different between the C_1-O_1 and C_3-C_2 transitions. Overall, both constructs showed major effects relative to wild type

during the early C_3-C_2 transition while only GluN1(4C)/GluN2A(1C) significantly affected later gating transitions.

Asynchronous dynamics of the peripheral linkers during NMDA receptor activation

NMDA receptor gating was significantly dependent on the conformational freedom of the peripheral linkers both within (Fig. 3.7) and between (Fig. 3.8) subunits when compared to wild-type. To determine if there were construct-specific gating effects, we contrasted the ΔΔG values between pairs of constructs (Fig. 3.9A). During the C_3-C_2 transition, the inter-subunit GluN1(1C)/GluN2A(4C) construct showed a significant difference in ΔΔG compared to both the intra-GluN1 and intra-GluN2A constrained constructs. On the other hand, during the C_2-C_1 transition, the intra-subunit GluN1/GluN2A(1C-4C) construct had a significantly different ΔΔG value compared to the inter-subunit GluN1(1C)/GluN2A(4C) construct. Lastly, for the C_1-O_1 transition, the GluN1/GluN2A(1C-4C) and GluN1(4C)/GluN2A(1C) receptors showed greater differences in ΔΔG than that of the GluN1(1C)/GluN2A(4C) construct. Thus, the ΔΔG values between constructs are not equivalent during the different receptor activation steps, indicating specific peripheral linker rearrangements occur asynchronously relative to one another.

DISCUSSION

Pore opening is the key step in NMDA receptor gating that allows the flux of ions including Ca^{2+} across the membrane. This step occurs in a largely concerted fashion within the current limits of resolution (Schorge et al., 2005; Kussius and Popescu, 2009; Traynelis et al., 2010). In contrast, the highly homologous AMPA receptor subtypes gates in a subunit-specific manner (Rosenmund et al., 1998; Smith and Howe, 2000). For NMDA receptors, concerted pore opening could arise by the conformational change induced by agonist binding in the four subunits (Regalado et al., 2001) propagating in a synchronous manner to the ion channel gate, which is presumably located near the extracellular end of the M3 helices (Chang and Kuo, 2008; Sobolevsky et al., 2009). We find that the peripheral linkers that tightly surround the centrally located gating elements must rearrange for efficient gating to occur in NMDA receptors but that these rearrangements are not equivalent within and between different subunits (Fig. 3.9A). Thus, our results demonstrate that elementary steps prior to pore opening in NMDA receptors occur in a step-wise and asynchronous manner.

Constraining the mobility of the NMDA receptor peripheral linkers.

Based on structural homology to K+ channels (Wo and Oswald, 1995; Sobolevsky et al., 2009) and functional studies (Jones et al., 2002; Sobolevsky et al., 2002), pore opening in iGluRs is mediated by displacement of the pore-lining M3 helices away from the central axis of the pore (Traynelis et al., 2010). The peripheral transmembrane helices and their associated linkers closely surround these central gating elements and presumably must reposition to allow for pore opening (Sobolevsky et al., 2009). To study the dynamics of the peripheral elements during gating, we constrained the mobility of the peripheral linkers using pairs of introduced cysteines that spontaneously cross-linked (Figs. 3.2-3.4). We started with select positions in the linkers

that had previously been shown to affect gating (Talukder et al., 2010). We then searched for potential proximal positions around each of the reference points using the GluA2 structure as a guide (Sobolevsky et al., 2009). We identified numerous pairs of proximal positions that spontaneously cross-link (Figs. 3.2-3.4) and focused on four of them: two intra-subunit, GluN1(S531C-F792C) and GluN2A(V525C-D796C) [referred to as GluN1(1C-4C) and GluN2A(1C-4C), respectively]; and two inter-subunit, GluN1(P787C)/GluN2A(S535C) and GluN1(F540C)/GluN2A(S791C) [referred to as GluN1(4C)/GluN2A(1C) and GluN1(1C)/GluN2A(4C), respectively]. We then performed single channel studies and thermodynamic analysis on these cysteine-substituted receptors as well as wild type to address how constraining the peripheral linkers affected the dynamics of NMDA receptor gating. We assume that cross-linked receptors are not greatly distorted in their structure: the cross-links were introduced in the LBD-TMD peripheral linkers, which are extended peptides and hence presumably have some degree of structural flexibility; the cross-linked receptors had gating properties (closed and open state distributions) comparable to wild type; and cross-links will reform in functional, membrane expressed receptors.

Efficiency of NMDA receptor gating depends on the conformational freedom of the peripheral linkers.

Receptors containing introduced constraints of the peripheral linkers, either intra- or inter-subunit, showed dramatic reductions in single-channel P_o (Table 3.1). This effect was mainly due to the introduced constraints since all cysteine-substituted receptors showed a much greater DTT-induced potentiation in P_o than wild-type (Fig. 3.5 & Table 3.1). These results directly support the idea that the peripheral linkers must undergo conformational rearrangements for efficient gating to occur (Balannik et al., 2005; Sobolevsky et al., 2009).

The reduced P_os shown by the constrained receptors were the result of both increases in mean closed time and decreases in mean open time (Table 3.1). Hence, regions outside of the central pore axis can affect the relative stability of the closed and open states (Schmid et al., 2007; Talukder et al., 2010; Ren et al., 2012).

Although all constrained receptors showed a significantly reduced P_o, the degree of this reduction was highly variable. Most notable is the distinction between the intra-GluN1 cross-links, which reduced P_o by only 2-fold, and intra-GluN2A cross-links, which reduced P_o by 62-fold. The two intra-subunit constraints are positioned similarly between the N-terminal end of the presumed pre-M1 helix and the N-terminal end of M4 (Figs. 3.2A & B, *left panels*). Therefore the differing effects observed are unlikely to be due to drastic differences in the positioning of the constraints. One possible explanation is that the GluN1 and GluN2A subunits adopt different conformations paralleling those shown in the GluA2 crystal structure (Salussolia et al., 2011a; Riou et al., 2012), and therefore go through differential internal movements during gating (Banke and Traynelis, 2003; Sobolevsky et al., 2009; Dong and Zhou, 2011).

Elementary events prior to pore opening are asynchronous.

One of the hallmarks of the GluA2 structure was that the M1 and M4 helices and associated LBD-TMD linkers, S1-M1 and S2-M4, were positioned around the central gating elements, the M3 helices and associated M3-S2 linkers (Sobolevsky et al., 2009). The displacements of these peripheral elements could be synchronized across all four subunits immediately following ligand binding, or could alternatively be out-of-phase with each other until shortly before pore opening. The analysis shown in Figure 3.9A highlights that the different constraints between the peripheral linkers affect gating energetics at different points in the progression to pore opening, suggesting that their displacements are asynchronous. For example, the inter-subunit constraint

between GluN1 S2-M4 and GluN2A S1-M1 [N1(4C)/N2A(1C)] significantly affects the energetics of all three major gating transitions while the constraint within GluN2A [N1/N2A(1C-4C)] only significantly affects the C_2-C_1 and C_1-O_1 transitions (Fig. 3.9A).

We incorporated these different energetic effects into a model describing the dynamics of the peripheral linkers during gating (Fig. 3.9B). During the early gating transition (C_3-C_2), major repositioning occurs between, rather than within, subunits particularly between GluN1 S1-M1 and GluN2A S2-M4. During the C_2-C_1 transition, however, a dramatic repositioning occurs within GluN2A. During the opening transition (C_1-O_1), the predominant rearrangements occurred again among the GluN2A peripheral linkers, although the GluN1 S2-M4 and N2A S1-M1 linkers also repositioned relative to each other. Therefore, compared to the GluN1 subunits, the GluN2A subunits show a greater degree of internal rearrangements at the linker level. This distinction is consistent with prior findings in AMPA receptors that subunits occupying the B/D conformation (approximated by GluN2A in NMDA receptors) go through more extensive movements during gating relative to subunits in the A/C conformation (approximated by GluN1) (Dong and Zhou, 2011).

Without an open-state structure to define the endpoint of gating, specific structural changes occurring during gating cannot be absolutely defined. Further, our approach cannot delineate the nature and degree of the movements between the linkers. Relative 'movements' within a pair of positions could entail displacements of one or both of them in multiple directions. Also, we are unable to specify which peripheral linker predominates during gating movements. Finally, for the kinetic modeling, we assumed that the slow and fast events occurred in an obligate order (Fig. 3.9B), but they may occur in a random order as exemplified by cyclic NMDA receptor gating models (Banke and Traynelis, 2003). Forcing events into a linear

sequence might blur underlying kinetic rates. Still, given the robustness of effects on the slow and fast gating transitions (Fig. 3.9A), we assume that parallel effects would occur in the cyclic model (Erreger et al., 2005b). In such a scenario, the molecular rearrangements underlying the slow and fast transitions would still be asynchronous, although they would occur in any order.

Implications to the mechanisms underlying NMDA receptor gating

In NMDA receptors, the activation gate where concerted pore opening presumably occurs is located at the external end of the M3 helices, adjacent to the M3-S2 linkers (Chang and Kuo, 2008; Murthy et al., 2012). The peripheral linkers are positioned around and proximal to these central gating elements, yet our results suggest that they undergo asynchronous rearrangements prior to pore opening. One possibility is that these asynchronous rearrangements converge on a subsequent pre-open state that is permissive to the concerted movements of the M3 helices (Banke and Traynelis, 2003). Such a pre-open converged state might be akin to the short-lived 'flip' states observed in nicotinic and glycine receptors (Burzomato et al., 2004; Colquhoun and Lape, 2012). Alternatively, the displacements of the M3 helices may also occur asynchronously, with measurable currents only arising after all subunits have been displaced.

The mechanism of NMDA receptor partial agonism remains unknown. While altered LBD cleft closure contributes to partial activation in non-NMDA receptors (Hansen et al., 2007; Birdsey-Benson et al., 2010; Ahmed et al., 2011; Lau and Roux, 2011; Ramaswamy et al., 2012a), this mechanism appears less significant to NMDA receptors as several partial agonists of the GluN1 subunit show near complete LBD cleft closure yet variable degrees of receptor activity (Inanobe et al., 2005; Kaye et al., 2006; Rambhadran et al., 2011; Ylilauri and Pentikainen, 2012). Interestingly, partial agonists impede the kinetic mechanisms of NMDA receptor gating (Erreger et al., 2005b; Kussius and Popescu, 2009) but do not alter inherent

single-channel properties. Moreover, the relative kinetic aberrations we report for GluN1(1C-4C)/GluN2A are remarkably comparable to the kinetics of GluN1/GluN2A receptor activation by GluN1 partial agonists (Kussius and Popescu, 2009). Hence, while partial agonists may induce full LBD cleft-closure, the events subsequent to binding may not permit complete peripheral linker rearrangements, similar to what we have presented, and thus dampen gating. Further elucidating how the dynamics of peripheral elements contribute to NMDA receptor partial agonism might lead to the development of novel pharmacological agents for potential clinical applications.

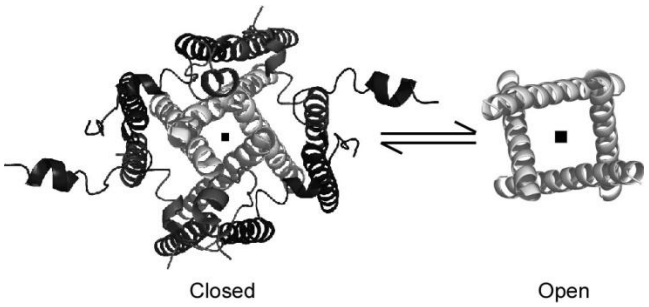

Figure 3.1 Pore opening in iGluRs involves displacement of the M3 transmembrane helix.

Left, a top-down view of the transmembrane domain (helices M1, M3, & M4) in the antagonist-bound (channel pore closed) GluA2 structure (PDB ID 3KG2) (Sobolevsky et al., 2009). The M3 helices (light gray) directly line the ion channel pore (square indicates central axis of the pore), while the M1 and M4 helices along with their associated linkers (dark gray) are located peripherally. *Right*, in an open-channel structure of Shaker Kv1.2 (2A79) (Long et al., 2005), the M3 helices (homologous to TM2 or S6 in K^+ channels (Wo and Oswald, 1995)) are splayed out compared to the close state. For iGluRs, the positioning of the peripheral structural elements as well as the specific details for the M3 helices in the open state is unknown.

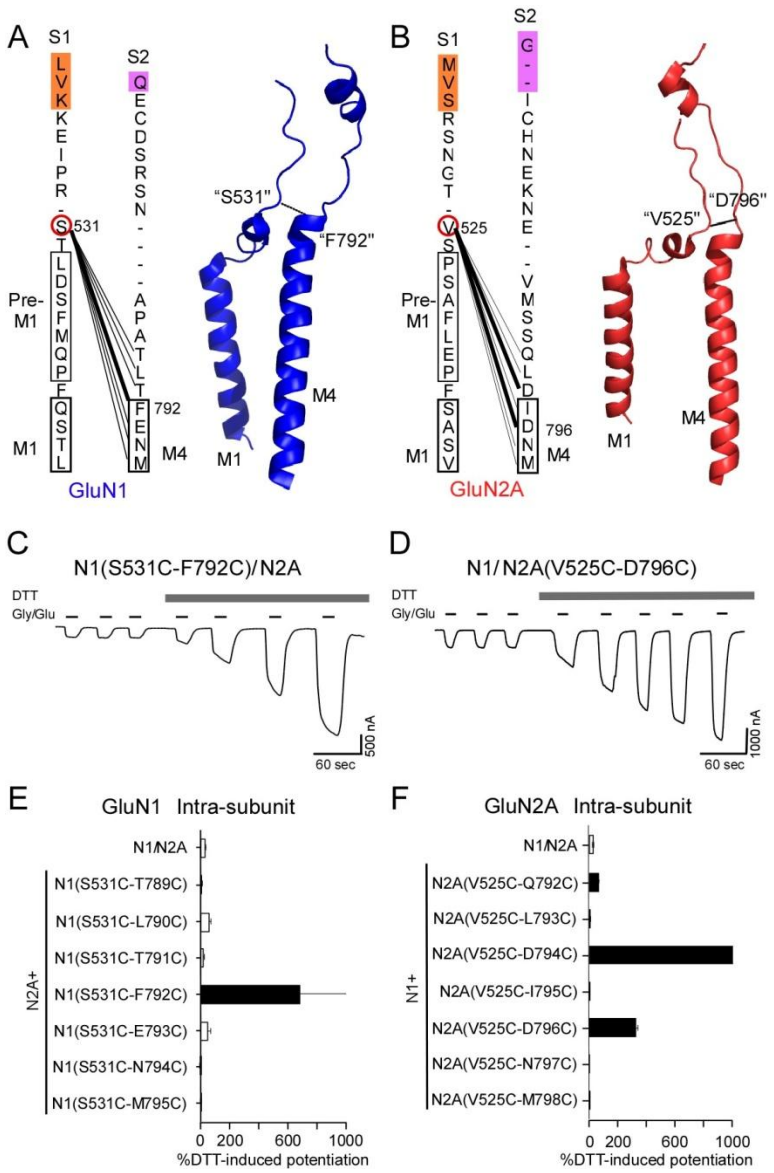

Figure 3.2 Intra-subunit cross-linking between S1-M1 and S2-M4 linkers of NMDA receptor subunits.

(A & B) *Left panels*, sequences of the S1-M1 and S2-M4 linkers of GluN1 (A) and GluN2A (B) with boxes indicating regions assumed to be helical based on sequence alignment with GluA2. Short dashes in the sequences indicate gaps in the alignment. *Right panels*, structures of these linkers along with the transmembrane segments they are connected to in GluA2 (Sobolevsky et al. 2009). Subunits in the A/C (approximating GluN1) and in the B/D (approximating GluN2A) conformation (Salussolia et al. 2011) are colored blue and red, respectively. The S1-M1 positions GluN1(S531) and GluN2A(V525) (red circles) were chosen as reference points. Multiple cysteine substitutions in the S2-M4 linker of the same subunit were screened in combination with S531C or V525C. Pairs of substitutions showed either no difference (thin lines) or significantly greater DTT-induced current potentiation (thick lines) compared to wild-

type when exposed to DTT. GluN1(S531C-F792C) and GluN2A(V525C-D796C), whose homologous residues in GluA2 are shown in the structure, were selected as "focal pairs" of cysteine substituted receptors for subsequent experiments.

(C & D) Representative membrane currents (holding potential V_h = – 60 mV) in *Xenopus* oocytes injected with GluN1(S531C-F792C)/GluN2A (C) or GluN1/GluN2A(V525C-D796C) (D). Currents were elicited by co-application of 20 μM glycine and 200 μM glutamate (black lines). Agonist-activated current amplitudes were potentiated when 4 mM DTT (gray bar) was applied.

(E & F) Mean percent potentiation of current amplitudes (± SEM; n ≥ 3) during DTT exposure. Solid bars represent cysteine-substituted receptors showing significantly greater potentiation ($p < 0.05$, Student's t-test) than wild-type GluN1/GluN2A (27 ± 4.0%, n = 11). For GluN1(S531C-F792C) (E), the error bar is not fully shown, whereas for GluN1/GluN2A(V525C-D794C) the mean value is not fully shown (390000 ± 150000%,)

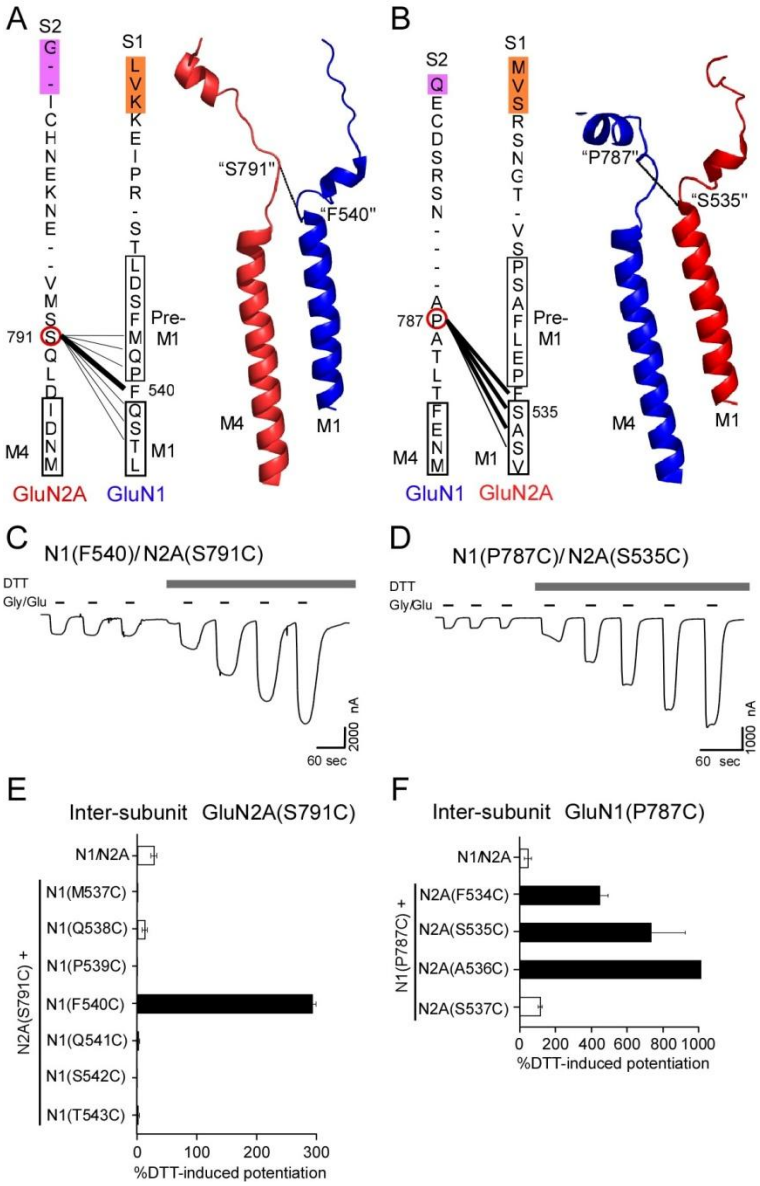

Figure 3.3 Inter-subunit cross-linking between S1-M1 and S2-M4 linkers of NMDA receptor subunits.

(A & B) The sequences of the S1-M1 and S2-M4 linkers of GluN1 and GluN2A as well as related structural elements in the GluA2 crystal structure are shown as in Figure 3.2, but paired in an inter-subunit manner. The S2-M4 positions GluN2A(S791) and GluN1(P787) (red circles) were chosen as reference points for screening introduced cysteines in the S1-M1 linkers of the other subunits. GluN1(F540C)/GluN2A(S791C) and GluN1(P787C)/GluN2A(S535C) whose homologous residues are shown in the structure, were selected as "focal pairs" of cysteine substituted receptors used for further studies.

(C & D) Membrane currents in oocytes injected with GluN1(F540C)/GluN2A(S791C) (C) or GluN1(P787C)/GluN2A(S535C) (D) and displayed as in Figs. 3.2C & 3.2D.

(E & F) Mean percent potentiation of current amplitudes (± SEM; $n \geq 3$) during DTT exposure is displayed as in Figs. 3.2E & 3.2F. The potentiation for GluN1(P787C)/GluN2A(A536C) (F) (21000 ± 1500%, $n = 4$) is not fully displayed.

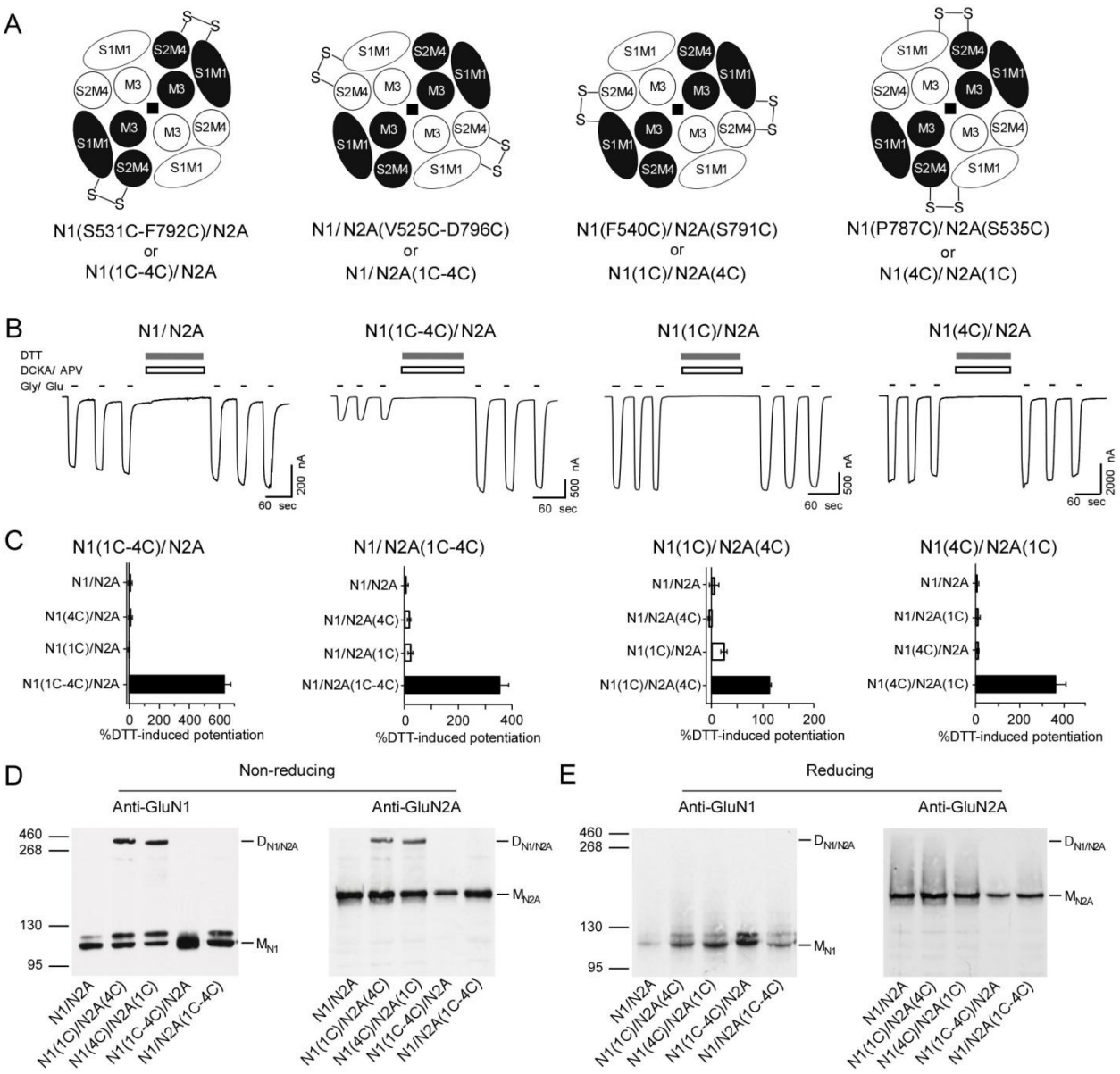

Figure 3.4 DTT-induced potentiation of agonist-activated currents is due to breakage of introduced disulfide cross-link.

(A) Schematics of cross-linking arrangements in cysteine-substituted receptors are shown in top-down view. In each receptor GuN1 subunits are black while GluN2A subunits are white. M3 helices and S2-M4 linkers are shown as circles while S1-M1 linkers are shown as ellipses, with disulfide bonds between different linkers indicated on the outside of the receptor. The selected focal pair for each cross-linking arrangement is listed below along with their abbreviated names (see text).

(B) Membrane currents in oocytes injected with GluN1/GluN2A, GluN1(1C-4C)/GluN2A, GluN1(1C)/GluN2A or GluN1(4C)/GluN2A. DTT (4 mM, gray bars) was applied for 120 sec in the presence of competitive antagonists DCKA (10 μM) and APV (100 μM) (open boxes). In contrast to GluN1(1C-4C), receptors containing the individual cysteine substitutions,

GluN1(1C)/GluN2A or GluN1(4C)/GluN2A, showed no significant DTT-induced current potentiation.

(C) Mean percent potentiation in current amplitudes (± SEM; $n \geq 5$) after DTT exposure for wild-type, the four focal pairs and receptors containing only one of the two substitutions in each pair. All experiments were done as in (A). Solid bars indicate constructs showing significantly greater potentiation ($p < 0.05$, Student's t-test) than GluN1/GluN2A (6.0 ± 7.0 %, n = 5).

(D, E) Immunoblots of membrane-purified proteins isolated from *Xenopus* oocytes injected with GluN1/GluN2A or the four focal pairs, assayed using antibodies against the N-terminal domain of GluN1 or GluN2A. Under non-reducing conditions (C), GluN1(1C)/GluN2A(4C) and GluN1(4C)/GluN2A(1C) formed a GluN1/GluN2A heterodimer ($D_{N1/N2A}$) . GluN1(1C-4C)/GluN2A and GluN1/GluN2A(1C-4C) showed only monomers (M_{N1} or M_{N2A}). Under reducing conditions (D), all constructs existed only as GluN1 (M_{N1}) or GluN2A (M_{N2A}) monomers.

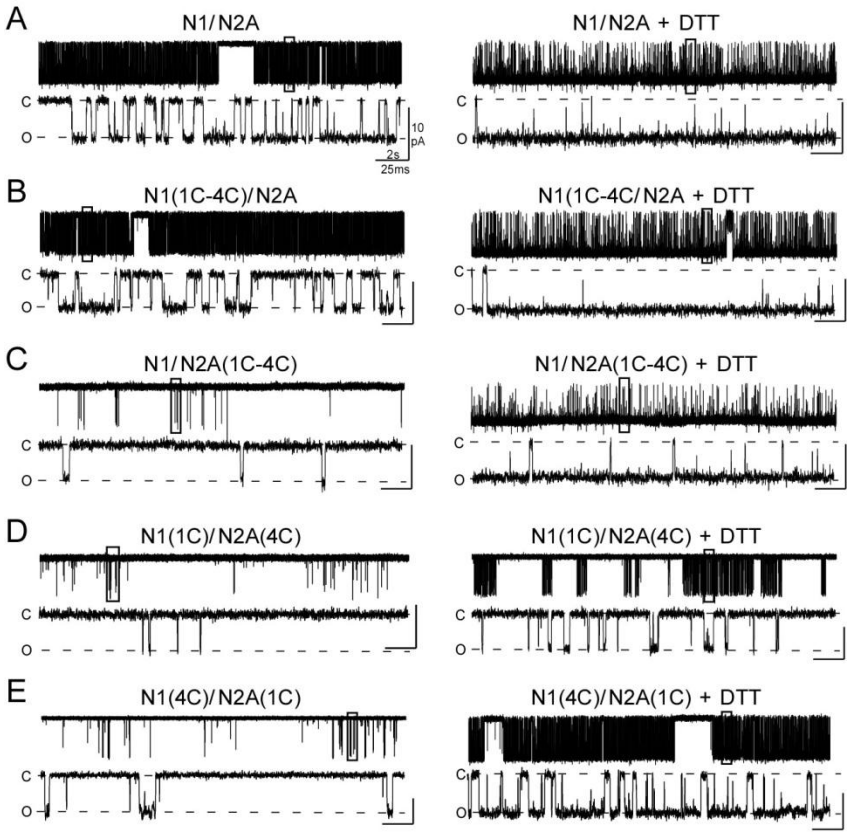

Figure 3.5 Cross-linking S1-M1 and S2-M4 linkers impedes NMDA receptor gating.

Representative single-channel traces from GluN1/GluN2A (A), GluN1(1C-4C)/GluN2A (B), GluN1/GluN2A(1C-4C) (C), GluN1(1C)/GluN2A(4C) (D), or GluN1(4C)/GluN2A(1C) (E) recorded either in the absence (-DTT, *left column*) or presence (+DTT, *right column*) of DTT. Single-channel recordings were done in the cell-attached mode under steady-state conditions at pH 8 and in 1 mM EDTA. For +DTT recordings, 4 mM DTT was included in the patch-pipette (in addition to agonists). In each panel, upper traces are lower resolution (digitized at 40 kHz, filtered at 1 kHz) segments of approximately 26 s of continuous activity while lower traces are at a higher resolution (filtered at 3 kHz) of approximately 250 ms of activity (box in upper trace).

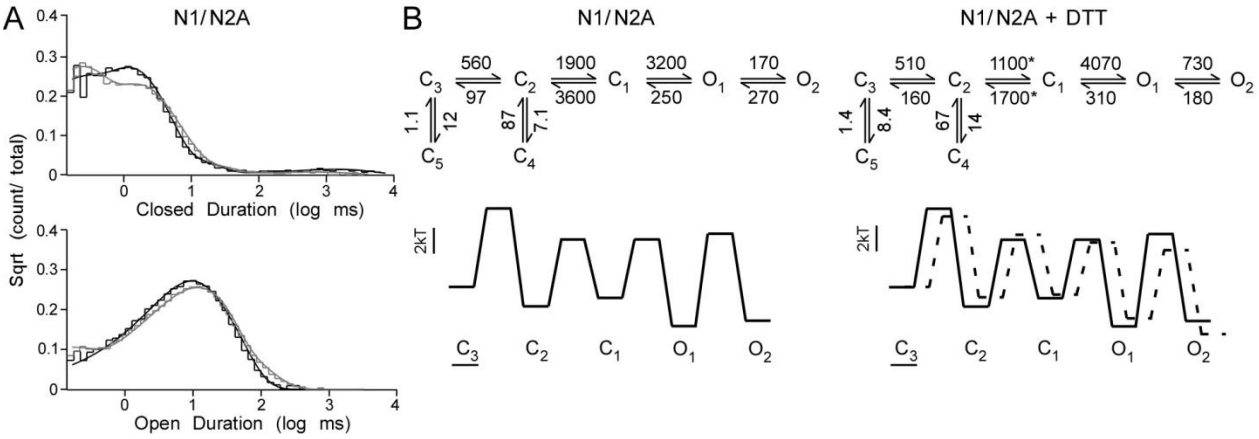

Figure 3.6 Kinetic modeling of GluN1/GluN2A in the absence and presence of DTT.

(A) Closed- (*upper panel*) and open- (*lower panel*) time durations for GluN1/GluN2A in the absence (*black lines*) or presence (*dashed lines*) of DTT. The closed-time distributions were both best fit with 5 closed states. The open-distributions were best fit with 4 open states, but are fitted here with 2 open states to permit comparisons across all tested constructs (see Materials and Methods).

(B) *Upper panel*, kinetic schemes for GluN1/GluN2A for the -DTT (*left column*) and +DTT (*right column*) conditions. Rate constants (s^{-1}) are average values for a kinetic scheme with 5 closed and 2 open states (Table 3.4). * indicates rates significantly different from the -DTT conditions ($p < 0.05$, Student's t-test). Number of patches: 8 (-DTT); 7 (+DTT).

(B) *Lower panels*, corresponding energetic landscapes for indicated kinetic schemes. The energy landscapes are shown as black continuous lines (wild-type, -DTT) or as black dashed lines (wild-type, +DTT). All landscapes were arbitrarily normalized to the C_3 state (underlined). The x-axis solely represents the gating states and does not carry a physical value. All plots have a unit scale of 2kT.

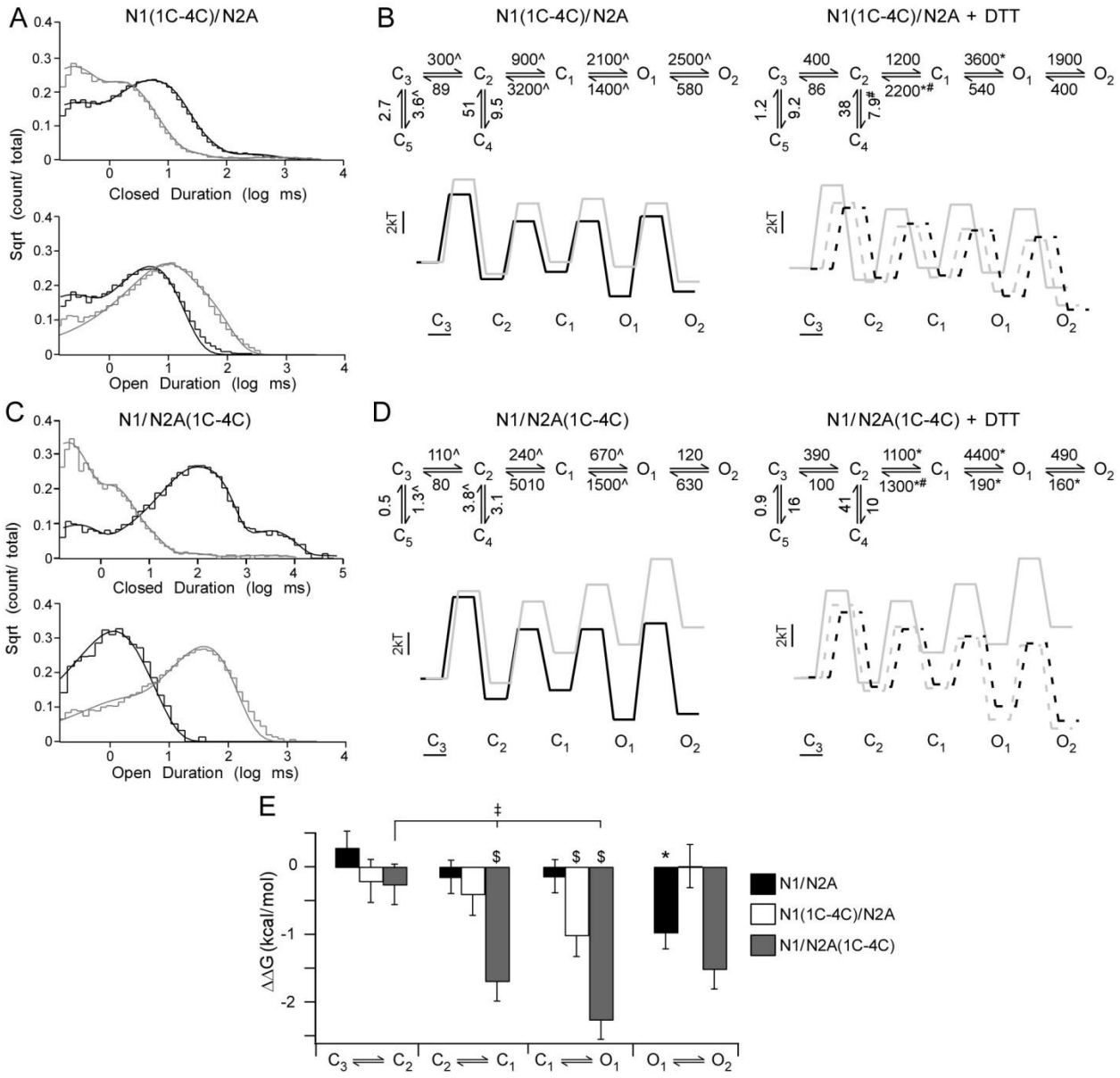

Figure 3.7 Intra-subunit cross-linking of S1-M1 and S2-M4 disrupts late gating transitions.

(A & C) Closed- (*upper panel*) and open- (*lower panel*) time durations for GluN1(1C-4C)/GluN2A (A) and GluN1/GluN2A(1C-4C) /GluN2A (C) in the absence (*gray lines*) or presence (*dashed lines*) of DTT. Fits are as described in Fig. 3.6A.

(B & D) *Upper panels*, kinetic schemes for GluN1(1C-4C)/GluN2A (B) and GluN1/GluN2A(1C-4C) (D) for the -DTT (*left column*) and +DTT (*right column*) conditions. Rate constants (s^{-1}) are average values for a kinetic scheme with 5 closed and 2 open states (Table 3.4). For the left column, ^ indicates rates significantly different from GluN1/GluN2A; for the right column, # indicates rates significantly different from GluN1/GluN2A + DTT while * indicates rates significantly different from the respective -DTT conditions ($p < 0.05$, Student's t-

test). Number of patches: GluN1(1C-4C)/GluN2A, 5 (-DTT), 4 (+DTT); GluN1/GluN2A(1C-4C), 7 (-DTT), 4 (+DTT).

(B & D) *Lower panels*, corresponding energetic landscapes for indicated kinetic schemes (see Materials & Methods). The energy landscapes are shown as black continuous lines (wild-type, -DTT), gray continuous lines (focal pairs, -DTT), black dashed lines (wild-type, +DTT), and gray dashed lines (focal pairs, +DTT). All landscapes are displayed as described in Fig. 3.6B.

(E) Mean ΔΔG (± SEM) between the +DTT (ΔG_{+DTT}) and -DTT (ΔG_{-DTT}) conditions for GluN1/GluN2A, GluN1(1C-4C)/GluN2A, and GluN1/GluN2A(1C-4C) for each gating transition (see Materials and Methods). * indicates significant differences between ΔG_{+DTT} and ΔG_{-DTT} for GluN1/GluN2A during the O_1-O_2 transition ($p < 0.05$, Student's t-test). $ indicates significant differences between a cysteine-substituted receptor and wild-type ($p < 0.05$, Student's t-test) for a specific transition. ‡ indicates significant differences between a pair of transitions within a construct, with the longer vertical line indicating the reference value ($p < 0.05$, Student's t-test).

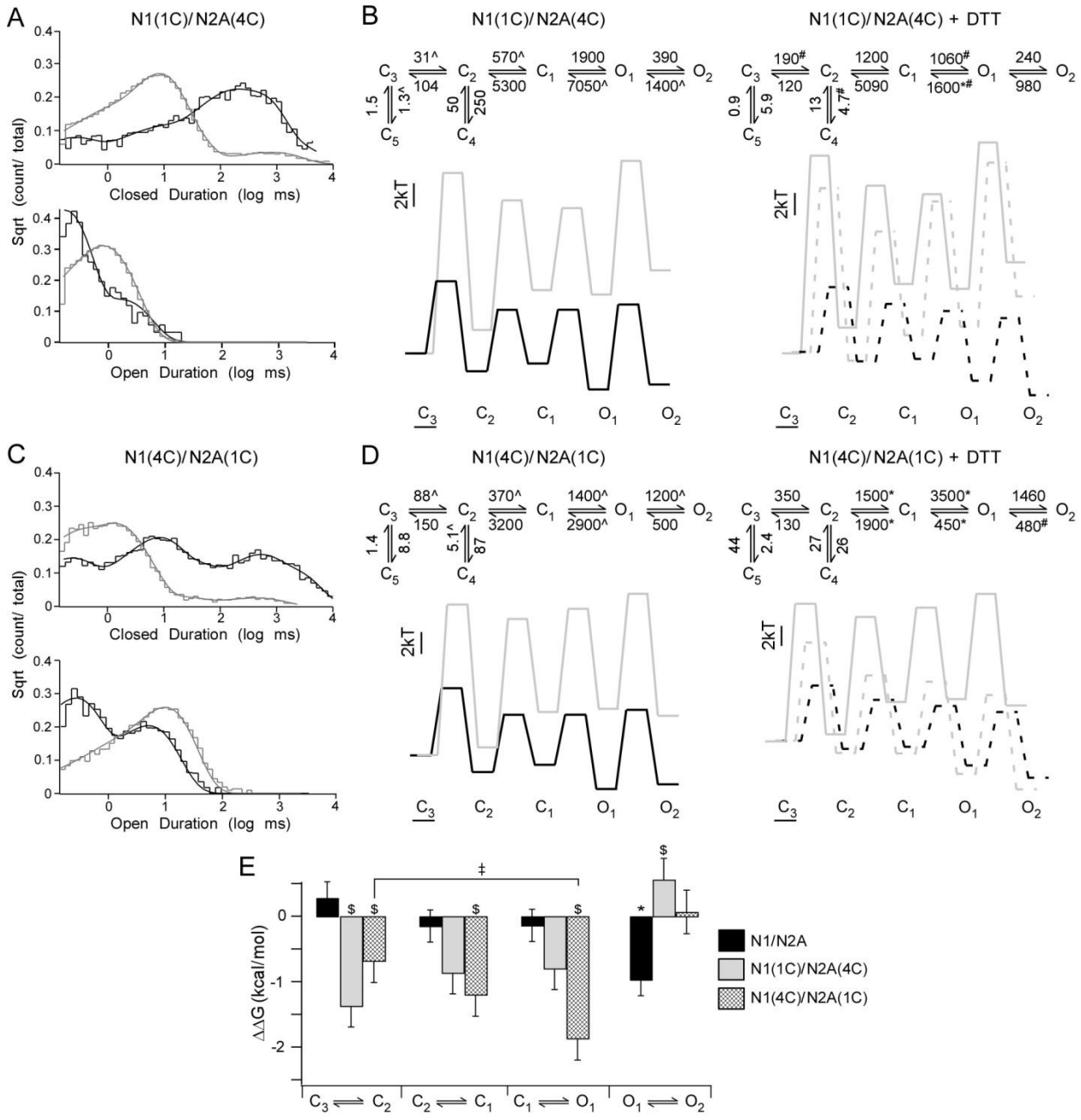

Figure 3.8 Inter-subunit cross-linking of S1-M1 and S2-M4 disrupts early and late gating transitions.

(A & C) Closed- (*upper panel*) and open- (*lower panel*) time durations for GluN1(1C)/GluN2A(4C) (A) and GluN1(4C)/GluN2A(1C) (C) in the absence (*gray lines*) or presence (*dashed lines*) of DTT. Fits are as described in Fig. 3.6A.

(B & D) Kinetic schemes (*upper panels*) and energy landscapes *(lower panels)* for GluN1(1C)/GluN2A(4C) (B) and GluN1(4C)/GluN2A(1C) (D) for the -DTT (*left column*) and +DTT (*right column*) conditions. Results are displayed as in Figs 3.6B. For the left column, ^

indicates rates significantly different from GluN1/GluN2A; for the right column, # indicates rates significantly different from GluN1/GluN2A +DTT while * indicates rates significantly different from the respective -DTT conditions ($p < 0.05$, Student's t-test). Number of patches: GluN1(1C)/GluN2A(4C), 7 (-DTT), 4 (+DTT); GluN1(4C)/GluN2A(1C), 6 (-DTT), 4 (+DTT).

(B & D) *Bottom panel*, energetic landscapes for tested constructs displayed as in Fig. 3.7.

(E) Mean $\Delta\Delta G$ (± SEM) between the +DTT and -DTT conditions for GluN1/GluN2A, GluN1(1C)/GluN2A(4C), and GluN1(4C)/GluN2A(1C). Results are shown and analyzed as in Fig. 3.7E.

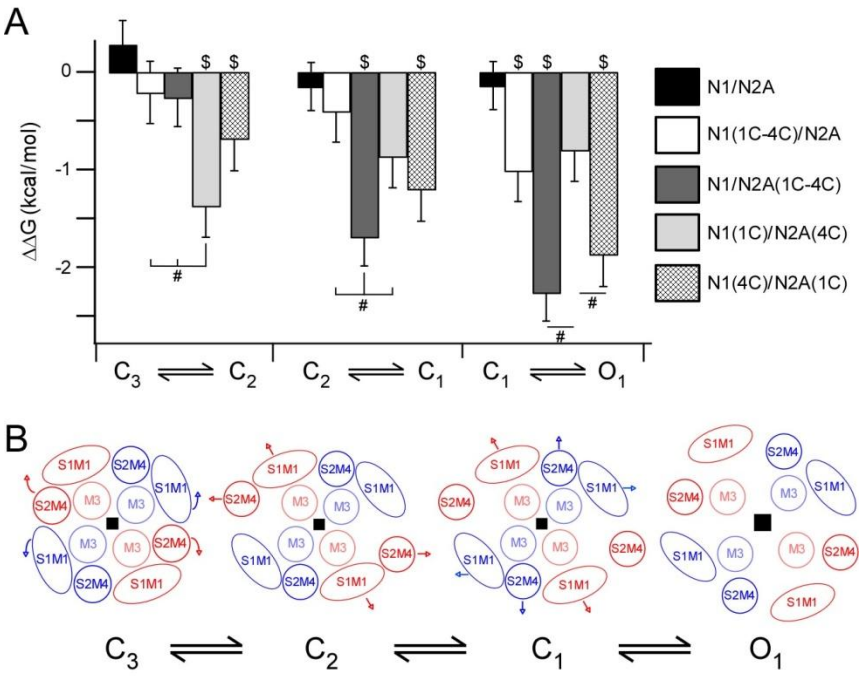

Figure 3.9 Thermodynamic progression of the peripheral linkers during NMDA receptor gating.

(A) ΔΔG plots for gating transitions (C_3-C_2, C_2-C_1, and C_1-O_1) for wild-type and the four receptors with focal pairs of introduced cysteines. Values shown are from Figs. 3.7E & 3.8E. # indicates significant differences between a specific transition for the indicated pair of constructs ($p < 0.05$, Student's t-test). $ indicates significant differences between a cysteine-substituted receptor and wild-type ($p < 0.05$, Student's t-test) for a specific transition.

(B) Schematic of relative peripheral linker movements during NMDA receptor activation. GluN1 subunit is labeled in blue, GluN2A is in red. Relative subunit positioning incorporates previous structural and functional information (Sobolevsky et al., 2009; Salussolia et al., 2011a; Riou et al., 2012). Peripheral linkers and M3 are labeled accordingly. S1-M1 presumably occupies a larger volume due to its oblique orientation (Sobolevsky et al., 2009). Each model represents hypothesized positions for the specified state while arrows indicate the major peripheral linker rearrangements occurring as the channel approaches the O_1 state. Arrow magnitudes are arbitrary and carry no physical meaning.

	Total Events (# of patches)	*i* (pA)	P_o	MCT (ms)	MOT (ms)
N1/N2A					
-DTT	500,200 (8)	-7.6 ± 0.3	0.71 ± 0.04	3.0 ± 0.4	8.1 ± 0.9
+DTT	890,000 (7)	-7.6 ± 0.2	0.88 ± 0.04*	2.6 ± 0.9	21 ± 4.4*
N1(1C-4C)/N2A					
-DTT	990,000 (5)	-7.6 ± 0.3	0.46 ± 0.05^	5.7 ± 0.7^	4.8 ± 0.4^
+DTT	890,000 (4)	-9.4 ± 0.9	0.83 ± 0.05*	3.2 ± 0.9	17.7 ± 3.3*
N1/N2A(1C-4C)					
-DTT	91,000 (7)	-11.7 ± 0.7^	0.014 ± 0.006^	270 ± 70^	1.2 ± 0.2^
+DTT	200,000 (4)	-7.4 ± 0.3*	0.87 ± 0.06*	4.0 ± 1.1*	40.7 ± 10.1*
N1(1C)/N2A(4C)					
-DTT	13,300 (7)	-6.9 ± 0.5	0.002 ± 0.0005^	620 ± 280^	0.38 ± 0.06^
+DTT	204,000 (4)	-10.9 ± 0.5*	0.04 ± 0.005*	25.1 ± 2.1*	0.90 ± 0.09*
N1(4C)/N2A(1C)					
-DTT	23,300 (6)	-10.9 ± 0.9^	0.007 ± 0.0008^	400 ± 150^	2.5 ± 0.8^
+DTT	96,000 (4)	-9.1 ± 0.6	0.65 ± 0.08*	9.1 ± 3.5*	16.5 ± 3.4*

Table 3.1 Intra- or inter-subunit cross-linking of S1-M1 and S2-M4 linkers reduces NMDA receptor activation

Mean values (± SEM) for single-channel current amplitudes (*i*), equilibrium open probability (P_o), mean closed time (MCT) and mean open time (MOT). Single-channels recordings were analyzed in QuB (see Materials & Methods). P_o is the fractional occupancy of the open states in the MIL fitted single-channel recordings. Significance is shown either relative to GluN1/GluN2A (^) or to their respective non-DTT condition (*) ($p < 0.05$, Student's t-test). For numbering of residues see Fig. 3.4A.

		C_1	C_2	C_3	C_4	C_5
N1/N2A						
τ (ms)	-DTT	0.13 ± 0.002	1.1 ± 0.1	2.5 ± 0.36	15.7 ± 3.2	1060 ± 140
	+DTT	0.7 ± 0.01*	1.0 ± 0.07	2.7 ± 0.2	17.8 ± 3.4	880 ± 150
α (%)	-DTT	14.3 ± 1.2	53.7 ±5.9	30.9 ±6.4	0.85 ±0.2	0.15 ± 0.02
	+DTT	39.9 ± 2.7*	35.4 ± 2.4*	23.4 ± 3.4	1.1 ± 0.31	0.13 ± 0.05
N1(1C-4C)/N2A						
τ (ms)	-DTT	0.18 ± 0.01^	2.1 ± 0.21^	6.0 ± 0.76^	27.1 ± 6.7	450 ± 70^
	+DTT	0.16 ± 0.01	1.2 ± 0.1*	3.2 ± 0.3*	29.1 ± 5.5	1180 ± 348
α (%)	-DTT	15.1 ± 1.4	33.2 ± 4.3^	47.0 ± 3.6	4.4 ± 1.52	0.26 ± 0.05
	+DTT	30.3 ± 3.7*	46.2 ± 3.0*	22.6 ± 6.1*	0.73 ± 0.04	0.13 ± 0.03
N1/N2A(1C-4C)						
τ (ms)	-DTT	0.2 ± 0.02^	39.4 ± 14^	130 ± 37^	1200 ± 430^	16000 ± 8900
	+DTT	0.15 ± 0.01	1.1 ± 0.2*	3.8 ± 0.85*	65 ± 39.4*	1490 ± 360
α (%)	-DTT	3.9 ± 0.9^	22.9 ± 6.2^	60.7 ± 4.6^	10.2 ± 1.7^	2.2 ± 0.9^
	+DTT	47.4 ± 4.2*	37.9 ± 2.7	13.6 ± 4.9*	0.84 ± 0.5*	0.20 ± 0.05
N1(1C)/N2A(4C)						
τ (ms)	-DTT	0.33 ± 0.08	6.6 ± 2.3^	96 ± 26^	400 ± 90^	1700 ± 740
	+DTT	0.19 ± 0.07	3.8 ± 1.1	12.5 ± 2.3*	91.2 ± 23.3*	1140 ± 90
α (%)	-DTT	5.6 ± 1.8^	9.1 ± 2.3^	23.9 ± 5.8^	39.6 ± 6.5^	21.8 ± 7.4^
	+DTT	4.1 ± 1.2	34.1 ± 8.9	57.5 ± 9.0*	3.1 ± 0.86*	1.3 ± 0.10*
N1(4C)/N2A(1C)						
τ (ms)	-DTT	0.24 ± 0.03^	4.9 ± 1.2^	25.2 ± 5.8^	470 ± 95^	2380 ± 570
	+DTT	0.17 ± 0.01	1.0 ± 0.15*	4.0 ± 1.2*	150 ± 94*	2100 ± 1500
α (%)	-DTT	10.9 ± 1.9^	25.5 ± 6.0^	26.1 ± 6.1^	21.7 ± 3.1^	15.8 ± 5.9^
	+DTT	31.5 ± 6.8	48.6 ± 3.2*	17.4 ± 8.8	1.6 ± 0.28*	0.98 ± 0.62

Table 3.2 Closed state durations and occupancies for wild-type and receptors with focal cysteine pairs.

Mean values (± SEM) for closed state durations (τ, ms) and occupancies (α, %). Values were derived after fitting idealized single-channel records to a five-closed and two-open state kinetic scheme (see Materials & Methods). Significance is shown either relative to GluN1/GluN2A (^) or to their respective non-DTT condition (*) ($p < 0.05$, Student's t-test).

	τ_{O1}, ms	α_{O1}, %	τ_{O2}, ms	α_{O2}, %
N1/N2A				
-DTT	4.4 ± 0.87	47.9 ± 7.9	11.3 ± 1.3	52.1 ± 7.9
+ DTT	4.2 ± 1.4	31.4 ± 9.8*	26.4 ± 3.7*	68.6 ± 9.8
N1(1C-4C)-N2A				
-DTT	0.7 ± 0.5^	20.5 ± 7.0^	5.7 ± 0.4^	79.6 ± 7.0^
+ DTT	2.1 ± 1.7	19.1 ± 13.5	21.1 ± 3.5*	80.7 ± 13.4
N1/N2A(1C-4C)				
-DTT	0.7 ± 0.1^	70.7 ± 10.9	3.2 ± 1.2^	29.3 ± 10.9
+ DTT	2.2 ± 1.1	14.9 ± 7.1*	45.2 ± 9.9*	85.11 ± 7.12*
N1(1C)/N2A(4C)				
-DTT	0.15 ± 0.01^	81 ± 3.1^	1.5 ± 0.3^	18.9 ± 3.1^
+ DTT	0.57 ± 0.14*	58.4 ± 13.7	1.8 ± 0.5	41.6 ± 13.7
N1(4C)/N2A(1C)				
-DTT	0.3 ± 0.08^	47.1 ± 3.6^	4.5 ± 1.4^	52.9 ± 3.6^
+DTT	0.7 ± 0.3	7.5 ± 1.24*	17.7 ± 3.6*	92.5 ± 1.2*

Table 3.3 Open state durations and occupancies for wild-type and receptors with focal cysteine pairs.

Mean values (± SEM) for open state durations and occupancies. Significance is shown either relative to GluN1/GluN2A (^) or to their respective non-DTT condition (*) ($p < 0.05$, Student's t-test).

		C_3-C_2	C_2-C_1	C_1-O_1	C_3-C_5	C_2-C_4	O_1-O_2
N1/N2A							
Forward	-DTT	560 ±100	1900 ± 140	3200 ± 190	12 ± 2.8	7.1 ±2.1	170 ± 140
	+DTT	510 ± 42	1100 ± 62*	4070 ± 280	8.4 ± 3.2	14 ± 3.7	730 ± 450
Reverse	-DTT	97 ± 20	3600 ±140	250 ± 34	1.1 ±0.2	87 ± 18	270 ± 140
	+DTT	160 ± 40	1700 ± 120*	310 ± 130	1.4 ± 0.3	67 ± 9.2	180 ± 50
N1(1C-4C)/N2A							
Forward	-DTT	300 ± 50^	900 ± 140^	2100 ± 140^	3.6 ± 1.0^	9.5 ±1.4	2500 ± 680^
	+DTT	400 ± 50	1200 ± 56	3600 ± 350*	9.2 ± 3.6	7.9 ±1.8#	1900 ± 1040
Reverse	-DTT	89 ± 13	3200 ±130^	1400 ± 290^	2.7 ±0.6	51 ± 14	580 ± 90
	+DTT	86 ± 9.9	2200 ±170*#	540 ± 270	1.2 ± 0.4	38 ± 7.1	400 ± 120
N1/N2A(1C-4C)							
Forward	-DTT	100 ±63^	240 ± 46^	670 ± 190^	1.3 ± 0.7^	3.1 ±1.8	120 ± 47
	+DTT	390 ±120	1100 ± 140*	4400 ± 1200*	16 ± 6.9	10 ± 2.7	490 ± 160
Reverse	-DTT	80 ± 56	5010 ±730	1500 ± 310	0.5 ±0.3	3.8 ±1.6^	630 ± 140
	+DTT	100 ± 30	1300 ± 60*#	190 ± 14*	0.9 ± 0.2	41 ± 16	160 ± 30*
N1(1C)/N2A(4C)							
Forward	-DTT	31 ± 15^	570 ± 210^	1900 ± 830	1.3 ± 0.5	250 ± 170	390 ± 56
	+DTT	190 ± 60#	1200 ± 200	1060 ± 240#	5.9 ± 1.6	4.7 ±1.3#	240 ± 120
Reverse	-DTT	104 ± 74	5300 ±1800	7050 ± 800^	1.5 ± 0.3	50 ± 18	1400 ± 470^
	+DTT	120 ± 66	5090 ± 1450	1600 ± 250*#	0.9 ±0.05	13 ± 2.8	980 ± 280
N1(4C)/N2A(1C)							
Forward	-DTT	88 ± 22^	370 ± 27^	1400 ± 250^	8.8 ± 2.6	87 ± 58	1200 ± 200^
	+DTT	350 ±110	1500 ± 230*	3500 ± 460*	44 ± 25	26 ± 4.9	1460 ± 580
Reverse	-DTT	145 ± 70	3200 ±300	2900 ± 410^	1.4 ±0.8	5.1 ±1.9^	510 ± 120
	+DTT	130 ± 32	1900 ± 210*	450 ± 160*	2.3 ± 1.2	27 ± 14	480 ± 90#

Table 3.4 Kinetic Rate Constants for Wild-type and receptors with focal cysteine pairs.

Mean values (± SEM) for kinetic rate constants (s^{-1}) for a 5C-2O gating model. Significance is shown either relative to GluN1/GluN2A (^) or to their respective non-DTT condition (*) ($p < 0.05$, Student's t-test).

CHAPTER 4: CHARACTERIZING THE THERMODYNAMICS OF NMDA RECEPTOR PORE OPENING

INTRODUCTION

In this chapter, we will address approaches to characterize the linkage between the neurotransmitter-binding site and the ion channel during pore opening in a glutamate-gated ion channel, the N-methyl-*D*-aspartate receptor (NMDAR). The approach we describe is rooted in a combination of high-resolution single channel recordings of NMDARs (Banke and Traynelis, 2003; Popescu and Auerbach, 2003; Schorge et al., 2005) and chemical transition state theory (Φ-value or REFER analysis) (Matouschek et al., 1989; Fersht and Sato, 2004; Zhou et al., 2005; Purohit et al., 2007). NMDARs are tetrameric complexes typically composed of two glycine-binding GluN1 subunits and two glutamate-binding GluN2 subunits. A common subunit combination throughout the nervous system is GluN1/GluN2A (Traynelis et al., 2010). GluN1/GluN2A NMDARs also represent a powerful system to address the thermodynamics of ion channel opening because under certain conditions (see below), their single channel activity is robust and displays a single conductance level, thus simplifying kinetic analysis (Popescu and Auerbach, 2003; Traynelis et al., 2010). Understanding the thermodynamic principles of pore opening in GluN1/GluN2A NMDARs will guide our understanding of pore opening in other NMDAR subunit combinations, other types of ionotropic glutamate receptors (iGluRs), and ligand-gated ion channels in general.

iGluRs, including NMDARs are composed of several highly modular domains (Dingledine et al., 1999). The ligand-binding domain (LBD) is located extracellularly and is linked to the pore-forming transmembrane domain (TMD) (membrane spanning segments M1, M3 & M4) by a set of short polypeptide linkers, termed the LBD-TMD linkers. Crystallographic

data from isolated LBDs has shown that the LBD exists largely as a two-lobe structure, akin to a Venus fly trap or clamshell, and that agonist binding induces an upward translation of the lower lobe (clamshell closure) (Armstrong and Gouaux, 2000; Mayer et al., 2001; Sun et al., 2002; Furukawa et al., 2005; Yao et al., 2013). This movement generates several kilocalories of energy (Dong and Zhou, 2011; Lau and Roux, 2011; Yao et al., 2013), which is then transferred, in a largely unknown manner, from the LBD to the TMD, driving TMD rearrangement and facilitating pore opening.

The allosterics of NMDAR ion channel opening is dependent on understanding several key features: (i) how, mechanistically, is the energy of the agonist-bound LBD transferred to the TMD; (ii) the relative timing and displacement of transmembrane helices leading to synchronous pore opening; and (iii) local interactions that impact the energetics of the closed and open states as well as the transition states between them. A variety of approaches have been implemented to address these questions. For example, functional assays such as substituted cysteines (Sobolevsky et al., 2007; Chang and Kuo, 2008; Talukder et al., 2010) and FRET-based measurements (Landes et al., 2011; Ramaswamy et al., 2012b) have yielded valuable insight into the general mechanisms underlying the allosteric transition process. On the other hand, structural studies of stable (Sobolevsky et al., 2009; Mayer, 2011) and unstable (Lau et al., 2013; Schauder et al., 2013) states of the ligand-binding domain provided detailed and quantitative information concerning specific stages of the transition.

A complimentary approach to addressing the dynamics of pore opening is ϕ-value or rate equilibrium-free energy (REFER) analysis (Matouschek et al., 1989; Ozkan et al., 2001; Auerbach, 2007). While initially used to describe the dynamics of folding in small proteins (Fersht and Sato, 2004; Merlo et al., 2005; Raleigh and Plaxco, 2005), it has been successfully

applied to channel opening in nAChR (Purohit et al., 2007; Purohit et al., 2013) and K^+ channels (Wang et al., 2011). Our approach encompasses concepts of Φ-value analysis along with unique features of the NMDAR gating process to quantify the energetic landscape of pore opening in NMDARs.

Thermodynamics of pore opening

From a thermodynamic perspective, ion channels are allosteric proteins transitioning between two end states, a closed (C) and open (O) state (Fig. 4.1A). For ligand-gated ion channels, these states can be populated in either the agonist-unbound or agonist-bound form (Jackson, 1986; Grosman and Auerbach, 2000; Purohit and Auerbach, 2009). According to Monod-Wyman-Changeux allosteric theory, agonist binding alters the likelihood of the channel being observed in a given state (Monod et al., 1965; Auerbach, 2012) and provides the energy necessary to populate the open state in a rapid, physiologically relevant timescale.

In the presence of agonist, the ion channel will transition between the closed and open states based on the energy of the activation barrier ($\Delta G^{\ddagger}$) as well as the difference in energy between the end states (ΔG^0) (Fig. 4.1A). Kinetically, these transitions are defined by the forward (k_f) and reverse (k_b) rates. As the channel transitions between these states, it adopts transient, intermediate conformations (χ) (Figs. 4.1B & 4.1C) that are cumulatively referred to as the transition state ensemble (TSE) (Matouschek et al., 1989). While generally irresolvable, the TSE defines the transition frequency between the end states. Alterations of NMDARs, either artificial site-directed mutations or naturally-occurring missense mutations that induce neurodevelopmental disorders (gain- or loss-of-function), may shift the distribution of state occupancies by changing the energetics of the closed state, of the TSE, and/or of the open state.

Φ-value analysis can provide information about the TSE as well as (under certain conditions) the relative timing of the events (Auerbach, 2007). The energetic features of the TSE within a given transition are reflected in the relationship between the forward rate constant k_f, which correlates to $\Delta G^{\ddagger}$, and the equilibrium constant K_{eq}, which correlates to ΔG^0 (Fig. 4.1C). The analysis plots k_f [$\log(k_f)$] against K_{eq} [$\log(K_{eq})$] for a variety of mutations at a single point of perturbation (Fig. 4.2A). The slope of the line fit to the plot is termed Φ. Because $\log(k_f)$ is a function of the energy between the closed state and the transition energy barrier and $\log(K_{eq})$ is a function of the energy difference between the end states (Fig. 4.1C), the Φ-value can be interpreted to reflect variations in the TSE (Matouschek et al., 1989). The Φ-value of a given point of perturbation depends on which subset of the TSE is being affected by these perturbations. Therefore it is often interpreted to reflect the relative timing of the displacement of that position between the two end states (Auerbach, 2007) (Figs. 4.2B & 4.2C).

Application of Φ-value analysis to GluN1/GluN2A NMDARs

Kinetic analysis of single GluN1/GluN2A NMDARs has resolved five closed and two to four open states following ligand binding. A subset of the closed states can be connected linearly (C_3-C_2-C_1-O) and presumably reflect the transition from the agonist-bound closed state (C_3) and the open state (O), independent of desensitization (**Fig. 4.3A**). Based on transition state theory, these closed states likely reflect resolvable χ states, largely due to their relatively long lifetimes (**Fig. 4.3C**). Therefore, for NMDARs, Φ analysis on the overall C-O transition would not yield new information. Rather, timing information is presumably contained in the various transitions to the open state: C_3-C_2, C_2-C_1, and C_1-O. Thus, defining variations in the energetics of each of the transitions will provide information about the transfer of energy from the agonist-bound LBD to pore opening. .

During a two-state transition, a specific residue may isomerize to a certain degree. Correspondingly, its side chain experiences a different local environment, resulting in a change in its internal energy[1], which ultimately contributes to ΔG. To sample the energy of isomerization for a specific point of perturbation, one can substitute the residue with a diverse range of amino acids and monitor the effects on ΔG. Given that energy and structure are related, the maximum range of the change in ΔG produced by the mutations ($\Delta\Delta G$) indexes the extent of displacement or rearrangement an individual residues experiences during the transition (**Fig. 4.2A**). One can use $\Delta\Delta G$ as an index of the isomerization energy and hence the extent of displacement of that position during gating. Larger $\Delta\Delta G$ values suggest that the specific position dramatically isomerizes during channel opening while values nearing zero suggest that the position does not make a net isomerization. Critically, a comparison of the different isomerization energies for each transition would reveal which step undergoes the most displacement. Further, from Φ-value analysis, one can extract the relative time point at which the residue isomerizes within the tested transition.

For isomerization energy and Φ-value analysis, it is critical that a diverse range of side chains are tested[2]. An underlying assumption of these approaches is that the family of mutations tested alters local energetics without affecting the overall dynamics of channel opening. However, certain mutations could dramatically alter protein structure, which might change the natural dynamics of channel opening. Such mutations would not provide useful information regarding endogenous energetics. In Φ-value analysis, the plot of $\log(k_f)$ versus $\log(K_{eq})$ is generally linear, reflecting that the mutations produce parallel changes in the TSE energy relative

[1] It is equally as possible that energy changes are a result of perturbations in the local environment and not isomerizations of the amino acid side-chain per se.

[2] Too few or alike mutations may not adequately assay the conformational landscape of the position, thus resulting in underestimation of energetics and false negatives.

to those of the end-states. Hence, strong deviations from linearity would suggest that the mutation disrupts the natural pattern of channel opening. Thus, one can use the distribution of points on the Φ-value plot to assay the 'quality' of a mutation. There are several general outcomes here (a quantitative analysis is presented in Methods section): (i) All of the single-site mutations fall largely on the same line, suggesting that they alter only the local energetics. If this is the case, all of the mutations are included in subsequent analysis. (ii) Most of the mutations fall on the same line. Those that fall outside are assumed to disrupt the natural pattern of channel opening and are removed from analysis. (iii) A single line cannot be defined for any of the mutations. This would suggest that any mutation radically alters channel opening. The energetics of this position cannot be reliably assayed but this outcome could reflect that the position and/or its local environment are fundamental to NMDAR gating.

Although the dynamics of an individual position – and its local interactions – are important to pore opening, the types of analysis described here relate to broader issues: how is the energy of the LBD transferred to TMD and the relative timing of displacements in the TMD. To address these questions requires application of the above approach to a variety of positions in different parts of the protein. Therefore, by applying these analyses to different protein regions, one can generate a detailed energetic map of the dynamic conformational landscape during ion channel opening.

MATERIALS AND METHODS

Φ-value and isomerization energy analysis of ion channel opening encompasses two limiting considerations: First, for a position of interest (point of perturbation), a number of different manipulations must be made and tested to ensure that as broad as possible range of gating energetics for that position is sampled, without radically disrupting the normal process of channel opening. This generally involves substituting anywhere between 8-10 different amino acids with varying side-chain properties. The aim is to test the energetic/conformational landscape the native residue samples during channel opening. For this reason, it is best to avoid introducing amino acids with comparable side chains as well as glycine and proline because of their potential effects on secondary structures. For example, at a native serine, one would substitute arginine (positive charge), glutamate (negative charge), glutamine (bulky hydrophilic), tryptophan (bulky hydrophobic), leucine (bulky hydrophobic), threonine (bulky hydrophilic), and alanine (hydrophobic). For broader analysis, multiple positions must be tested. Hence, the total number of constructs tested can be extensive.

Second, for each of these constructs, one must generate high quality kinetic models of activation from which thermodynamic parameters are ultimately derived. Kinetic models must be based on activity from a single channel. Although single NMDAR channels can be recorded in a variety of configurations, the most advantageous for thermodynamic analysis is the cell-attached or on-cell configuration, with the inhibitory effects of pH and divalents minimized (Popescu and Auerbach, 2003). First, the signal-to-noise for cell-attached patches is high, even without time consuming manipulations to reduce noise such as Sylgard coating, increasing the rate of obtaining recordings. Second, in the cell-attached mode, recordings can be made for a long time – 60 minutes of high quality recordings is not unusual – greatly increasing the number

of events that are recorded. A large number of events are critical for generating high quality kinetic models and for identifying patches with a single channel, which can be challenging for a receptor with a low open probability.

NMDAR expression and single channel electrophysiology

1. HEK 293 cells or other mammalian cell line transfected with desired construct(s).
2. NMDAR inhibitors (AP5, DCKA, Mg^{+2}).
3. Standard electrophysiology setup.
4. Thick wall borosilicate capillary glass (Sutter)[3].
5. Micropipette puller (Sutter Instrument Model P-97).
6. Recording Solutions (in mM): Bath – 150 NaCl, 2.5 KCl, 10 Hepes, pH = 8.0; External (pipette) – 150 NaCl, 2.5 KCl, 1 EDTA, 1 Glutamate, 0.1 Glycine, 10 Hepes, pH = 8.0.
7. NMDAR activity is inhibited by protons and divalents, such as Zn^{+2}. High pH and EDTA remove these inhibitory mechanisms, maximizing single channel activity and yielding a single conductance level (Popescu and Auerbach, 2003). For more physiological external (pipette) solutions, incorporate calcium (0.5 mM) and less EDTA (0.01 mM).

Single channel analysis

1. QuB (University of Buffalo) (alternatives include DCProgs Suite)[4]
2. Microsoft Excel
3. MATLAB

Cell-attached single channel recordings

Plate HEK 293 cells on glass coverslips at a concentration of ~$0.4x10^5$cells/mL. Coverslips should be ~75% confluent at the time of transfection. Cells are co-transfected with eGFP for

[3] Sutter capillary glass gives consistent seals and high signal-to-noise compared to glass from other companies.
[4] QuB uses an automated SKM algorithm for data idealization while DCProgs uses a manual time course fitting approach. As such, QuB is better suited for high-throughput analysis such as required for thermodynamic analyses.

identification. A significant obstacle in single-channel recordings is the presence of multiple-channels in the patch. To minimize this, use 0.5 μg total cDNA/3 mL incubation media to express NMDARs at a low density.

NMDARs are caustic to cells, even in low numbers. Therefore, to increase cell survivability, switch to fresh media (containing inhibitors – APV [0.5 mM] or DCKA [0.5 mM], and Mg^{+2} [1 mM]) 4-5 hours after transfection. For cost considerations, inhibitors can be added only after switching media and not during the original transfection.

Experiments are generally performed 24-48 hours post transfection. Agonist-containing external (pipette) solutions are prepared fresh daily. Pipette solutions should be kept on ice to prevent degradation throughout the day and made again after ~8 hours. GFP positive cells are patched in the on-cell configuration[5]. Elicit inward currents by holding at a positive pipette potential. In our cases we use a pipette potential of +100 mV.

Analog data is filtered with a four pole low pass Bessel filter at 10 kHz (Axopatch 200B). We interface to the amplifier using PatchMaster (HEKA) software and an ITC-16 AD-DA board. Data should be sampled sufficiently to avoid aliasing, generally 4-5x the cutoff frequency. We typically sample at 50 kHz.

Data Processing and Idealization

Data is first visually inspected within the acquisition software and if sufficiently noise free is transferred to a single channel processing and analysis program. For our purposes, we use QuB software (www.qub.buffalo.edu, University at Buffalo) because it provides acquisition, idealization, and kinetic analysis methods in a single program with an easy to use, point-and-

[5] Mammalian cells expressing NMDARs are generally less healthy than non-expressing cells. Therefore, we patch cells that show sub-optimal morphology (uneven shape, slightly vacuolated).

click interface. This is vital when analyzing a large number of records, many of which contain thousands of events.

Visually inspected data with regions of high noise was omitted. A continuous baseline was set to normalize the record. Idealize data with the digital filter off. The user should try to minimize the difference between the dead time and the filter rise time (with a final cutoff frequency of 10 kHz, the filter rise time is ~ 33 μs).[6]If the user further filters the data, the final cascade frequency must be calculated.

Eq. 4.1

$$\frac{1}{f_c^2} = \sum_{i=1}^{n} \frac{1}{f_i^2}$$

Where f_c is the final cutoff frequency and n is the total number of filters used. For example, a 10 kHz analog filter followed by a 10 kHz digital filter will result in a final cutoff frequency of ~7.07 kHz.

Idealization of single-channel data involves unavoidable false event classifications. This is especially problematic for less filtered and low conductance data. Idealized data can be visually inspected to manually correct falsely classified events, but this is subject to operator bias. One can also calculate the false-event rate (λ)[7] with the following:

Eq. 4.2

$$\lambda \approx f_c^2 * e^{-0.5(A_{max}\ \sigma_n)^2}$$

Where λ is the false event rate (s^{-1}), f_c is the cutoff frequency, A_{max} is the amplitude at the given event duration and filtering, and σ_n is the RMS noise.

Current amplitudes may be underestimated for brief, heavily filtered events that have a

[6] Please refer to Howe JR, Cull-Candy SG, Colquhoun D (1991) Currents through single glutamate receptor channels in outside-out patches from rat cerebellar granule cells. The Journal of physiology 432:143-202. for further detail

[7] False event rate and amplitude calculations are most accurately applied to data idealized using the half-amplitude threshold method.

low conductance. The underestimated amplitude (A_{max}) can be solved with:

Eq. 4.3

$$A_{max} = A_0 * \text{erf}(0.886 * d \;\; T_r)$$

Where A_0 is the measured amplitude, d is the duration of the open event, and T_r is the filter rise time.

Following idealization, the full recording is modeled to a best fit kinetic model (Qin et al., 2000b). The best model is generally that which has the highest log-likelihood value or one which increases the log-likelihood value by less than 10 units from the previous model (see (Talukder et al., 2011; Kazi et al., 2013) for additional details)[8]. The resulting model is a kinetic model of activation at equilibrium (Fig. 4.3).

Determining single channel activity

For accurate kinetic analysis, it is critical that activity arises from exactly one channel. For receptors with a high open probability (e.g., $P_o > 0.10$), multiple channels will simultaneously open often enough for visual detection. For these channels, equilibrium kinetic modeling is preferred. However, if multiple channels are detected, one can isolate single channel activity by performing burst analysis and removing bursts which contain activity from more than one channel (Section 3.3.1). This analysis will work accurately for receptors which show reasonable single-channel activity and burst activity. On the other hand, certain constructs can show low channel activity and cannot confidently be divided into bursts. In these instances, one can statistically correlate the open probability and number of observed events to determine if activity is from one channel (Section 3.3.2). Kinetics rates from burst or equilibrium analysis for

[8] A value of 10 has generally been applied. It can be thought of as analogous to using a p value of < 0.05 (Fred Sachs, personal comm.). Users may also wish to use a Schwarz criterion in which states are added until the increase in log-likelihood score is less than ln(N)/2 where N = total number of events Schwarz G (1978) Estimating Dimension of a Model. Ann Stat 6:461-464..

wild type GluN1/GluN2A are largely indistinguishable (Table 4.1).

Burst analysis

To isolate bursts of activity, one must first identify the t_{crit} value – the time which accurately divides two given closed states. The goal is to divide open events separated by two closed states without misclassification. As such, it is best to cut between states with the most disparate time constants (generally a factor of 10-100x).

While there are multiple ways to solve for t_{crit}, we use the approach which minimizes the fraction of misclassified events (Jackson et al., 1983). Within QuB, t_{crit} values are reported during kinetic modeling. QuB solves for t_{crit} with the following:

Eq. 4.4

$$\alpha_m * e^{-t_{crit}\ \tau_m} = \alpha_n * (1 - e^{-t_{crit}\ \tau_n})$$

Where α and τ are the amplitude and time constant, respectively, from the exponential fits. M and n are the closed state before and after the cut, respectively (Qin et al., 2000a).

We also use an additional t_{crit} solver as suggested by Purohit and Grosman (Purohit and Grosman, 2006) (MATLAB script for this solver is freely available by contacting Rashek Kazi). This calculates t_{crit} with the following:

Eq. 4.5

$$Fraction\ misclassified\ events = \sum_{i=1}^{m} \alpha_i * e^{-t_{crit}\ \tau_i} - \sum_{j=m+1}^{n} \alpha_j * (1 - e^{-t_{crit}\ \tau_j})$$

Where i is the first closed state. M and j are the closed state before and after the cut, respectively. N is the total number of closed states. For example, for five total closed states, cutting between states four and five: i = 1, m = 4, j = 5, and n = 5.

The reported t_{crit} values should be used as a starting point and are refined empirically. Using either initial t_{crit} value, we use the ChopIDL function in QuB which separates consecutive open

events separated by a gap greater than or equal to the t_{crit}. For example, if a t_{crit} of 50 ms is set and two consecutive openings events are separated by a 75 ms closure, they will be divided into two separate bursts. Bursts containing multiple active channels must be removed manually.

We then concatenate the resultant bursts (this is done automatically in QuB) and fit them to a kinetic model. For example, if cutting between the fourth and fifth closed state, the t_{crit} value selected would remove the fifth closed state and therefore, our kinetic model must be best fit by no more than four closed states. We test this by seeing if the model minimally improves (< 10 log-likelihood units) with the addition of a fourth closed state or if the addition of the fifth state has 0% occupancy.

If the model is best fit by more than four closed states, the user must re-Chop the idealization using a shorter t_{crit} value, generally decreasing t_{crit} by approximately 10-30 ms. Due to the exponential fitting of closed event durations, there will be events which are classified as part of multiple closed states (Fig. 4.4B). Solving Eq. 5 with the chosen t_{crit} will calculate % misclassified events (Fig. 4.4C) (Purohit and Grosman, 2006). A generally accepted threshold is a misclassification rate of less than 1% (Schorge et al., 2005).

If the misclassification rate is greater than 1%, it is best not to cut between the chosen closed states. The user may try cutting between a different pair of closed states. If no alternative is possible, burst analysis is not advised.The bursts can now be fit with a 4-closed state kinetic model using the MIL algorithm. The user can add as many open states as necessary, but a minimum of two open states is required[9].

Statistical determination of single-channel patches

[9] NMDARs display modal open state activity, generally requiring between 2-4 open states Popescu G, Auerbach A (2003) Modal gating of NMDA receptors and the shape of their synaptic response. Nat Neurosci 6:476-483, Talukder I, Kazi R, Wollmuth LP (2011) GluN1-specific redox effects on the kinetic mechanism of NMDA receptor activation. Biophysical journal 101:2389-2398.

For receptors with low open probabilities ($P_o < 0.10$), simultaneous multiple-channel openings occur infrequently and if they are missed, multiple-channel patches will be incorrectly classified and analyzed as single-channel patches. For NMDARs constructs with a low open probability, one cannot perform burst analysis as described in Section 3.3.1 because separation between the time constants for the 4th and 5th closed states may not be significantly high enough, leading to a significant fraction of misclassified events. Therefore, for such constructs, it is best to perform equilibrium kinetic analysis and calculate the likelihood that the patch has a single channel (modified largely from (Colquhoun and Hawkes, 1990a) and (Dravid et al., 2008)).

Following kinetic analysis, the user obtains open probability (P_o) and the total number of events. Using the open probability, solve the following:

Eq. 4.6

$$E\ r\ =\ 2 * (1 - 0.5 * P_{o2} - 0.75 * P_{o2}^2)\ \ P_{o2}$$

Where E(r) is the number of events, and $P_{o2} = 2*P_o$.

For a given P_o, the data must contain, at minimum, E(r) number of events to be ~50% confident that the dataset contains no more than one channel. Obtaining greater than 4.6E(r) gives ~99% confidence that there was a single channel in the patch (**Fig. 4.5**).

Thermodynamic analysis

Kinetic modeling of single channel data, yielding k_f and k_b values for each transition (**Fig. 4.6A**), are derived for a wide range of perturbations at a single position. The k_f and k_b values are used for Φ-value analysis for each transition. From the Φ-value plot, we derive the linearity of the data points to identify those mutations that disrupt gating in an unnatural manner, the extent of residue isomerization (ΔΔG), and the timing (Φ) during that specific transition. Figure 6 illustrates such analysis for a single position, R641 of the GluN1 subunit. For broader

considerations of protein thermodynamics, and depending on the specific question to be addressed, multiple positions must be tested.

For a single position and transition (C_3-C_2, C_2-C_1, etc.), plot log(k_f) as a function of log(K_{eq}) where $K_{eq} = k_f/k_b$. The values for all of the tested constructs, including wild type, are plotted **(Fig. 4.6B)**. The values are then fit with a linear function. The linearity of the fit can be used as a quality control tool. Empirically, we define an $R^2 > 0.7$ as a 'good' fit. If $R^2 < 0.7$, we identify those point(s) that cause the poor fit and remove them individually until $R^2 > 0.7$. If more than 50% of total points need to be removed, it suggests that this position cannot be assayed for energetics.

From the remaining points on the Φ-value plot, calculate the energy of isomerization (ΔΔG). ΔΔG is a gauge as to how much displacement (energy change) the position experiences during gating. Using the K_{eq} values from the most extreme points on the x-axis, calculate the Gibbs free energy (ΔG) and then ΔΔG (**Fig. 4.6B**):

Eq. 4.7

$$\Delta G = -RTln(K_{eq})$$

Eq. 4.8

$$\Delta\Delta G = \Delta G_{max} - \Delta G_{min}$$

Where R is the gas constant, T is temperature. Max and min reflect the largest and smallest ΔG based on the Φ-value plot distribution, respectively.

Plot ΔΔG as a function of transition (Fig. 4.6C). We interpret the transition with the largest ΔΔG to indicate when in the transition from the agonist bound closed state (C_3) to the open state that that position undergoes the most significant isomerization. We use a value of 0.6 kcal/mol as a cutoff for a significant isomerization (Fersht and Sato, 2004).

The Φ-value – the slope of the linear fit to the Φ-value plot – is assumed to reflect the time point at which the tested residue isomerizes during the given transition (Zhou et al., 2005). There are multiple interpretations of this slope value[10] but in general, a value near one suggests a rapid isomerization (around the starting state) while a value near zero suggests an isomerization that arises near the end state (Figs. 4.2B & 4.2C).

Multiple tested positions may undergo similar isomerization energy for a specific transition. One can use the Φ-value to discern the relative timing of the various positions during such transitions. For a broader application, a similar type of analysis can be carried out for different points in the receptor. A comparison of isomerization energies and Φ-values can indicate how disparate points in the receptor isomerize during pore opening.

[10] Φ-values may also reflect a fractional structure of the side chain or that the side chain spends a certain fraction of the transition in a given end state. For example, a side-chain with a Φ-value of 0.9 is approximately 90% isomerized or is isomerized 90% of the time.

RESULTS

As an example of the application of free energy analysis in gating allostery, we explored the central linker, M3-S2, which tethers the LBD to the pore-forming helix of the TMD in NMDARs. We hypothesized that if energy traverses through the linker, then we would expect substantial dynamics throughout the linker. To test this, we performed an array of mutations between residue D640 and T647. Mutations ranged from small, hydrophobic to large, hydrophilic residues. This was done to properly assay the conformational spectrum these side chains may adopt during opening.

The mutations showed a diversity of responses, ranging between gained and reduced channel opening. Following proper kinetic and thermodynamic analysis, we found two general trends. The first was that residues showed differences during different kinetic transitions. For example, at position GluN1(R641), there were increasing $\Delta\Delta G$ values (Fig. 4.6) This suggests that following agonist binding, greater amounts of energy are transferred in a temporally progressive manner. This was, however, not always the case. More membrane-distal residues tended to show uniform free energy changes. For example, GluN1(T647) showed that across all kinetic transitions, the energy of movement was consistently less than 1 kcal/mol (Fig. 4.6).

Another trend was that the summed energy change tended to be greater for positions nearest the pore compared to those more distal (data not shown). This suggests that not only are residues more dynamic when approaching the pore opening transition, but they are also more dynamic when structurally nearest the pore. This is consistent with a "conformational wave" of residue rearrangements during pore opening. Similar models have appeared for nAChRs, though with notable regions of variability (Purohit et al., 2007; Purohit et al., 2013).

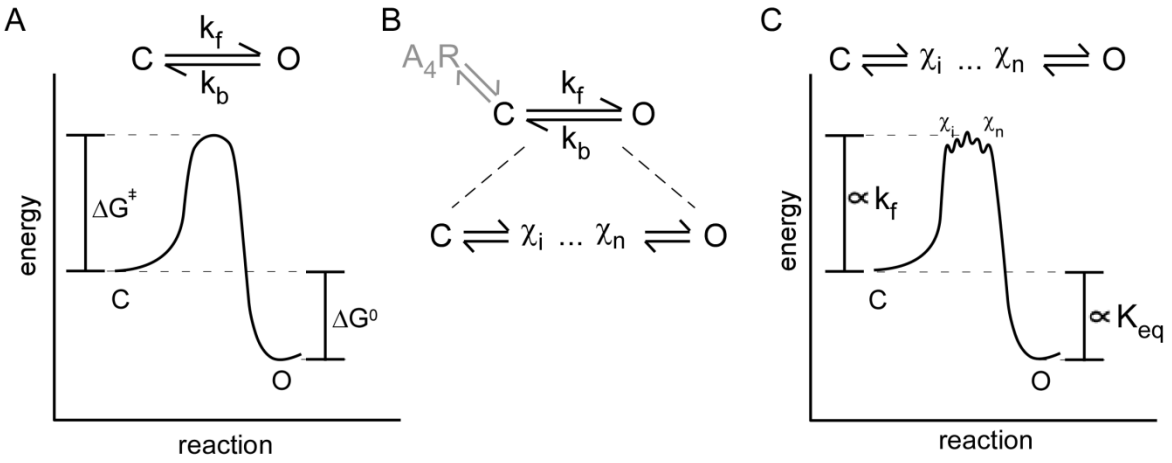

Figure 4.1 Energetics of ion channel opening.

(A) Two state kinetic scheme for ion channel opening. The two states, (C)losed and (O)pen, are separated by a transition energy ($\Delta G^{\ddagger}$). k_f and k_b represent the 'macroscopic' forward and reverse reaction rates, respectively. ΔG^0 is the energy difference between the two end states. **(B)** For ligand-gated ion channels, agonist (A) binding places the receptor in an agonist-bound closed state (C). In the transition to the open state, the ion channel adopts intervening conformations (χ_i) that can be collectively referred to as the transition state ensemble (TSE). **(C)** The forward rate constant, k_f, is correlated with $\Delta G^{\ddagger}$ whereas the equilibrium constant, K_{eq} (= k_f/k_b) is correlated with ΔG^0. Φ-value analysis obtains information about the TSE by considering the relationship between k_f and K_{eq}.

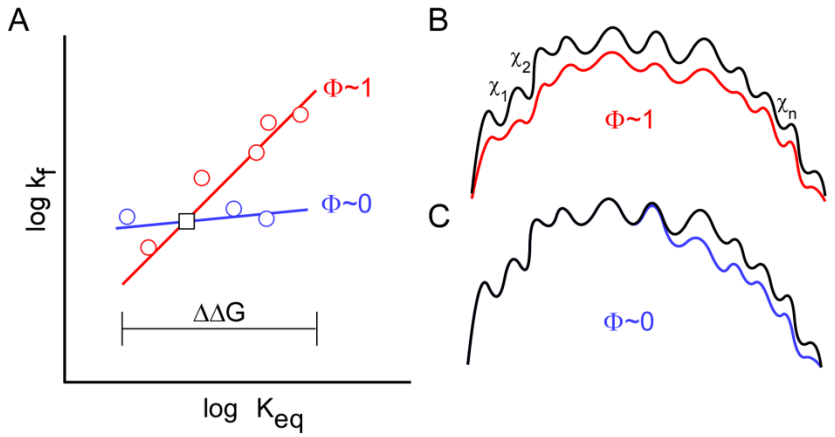

Figure 4.2 Φ-value analysis.

(A) Plot of the k_f versus K_{eq} for a hypothetical set of perturbations (open circles) at two remote locations in a protein. The slope of the line fit to these values is called Φ. The distribution of values on the plot also corresponds to the total energy change associated with this position (ΔΔG).
(B & C) Possible interpretation of differences in the Φ-value. The number of transition states (χ_n) is arbitrary.

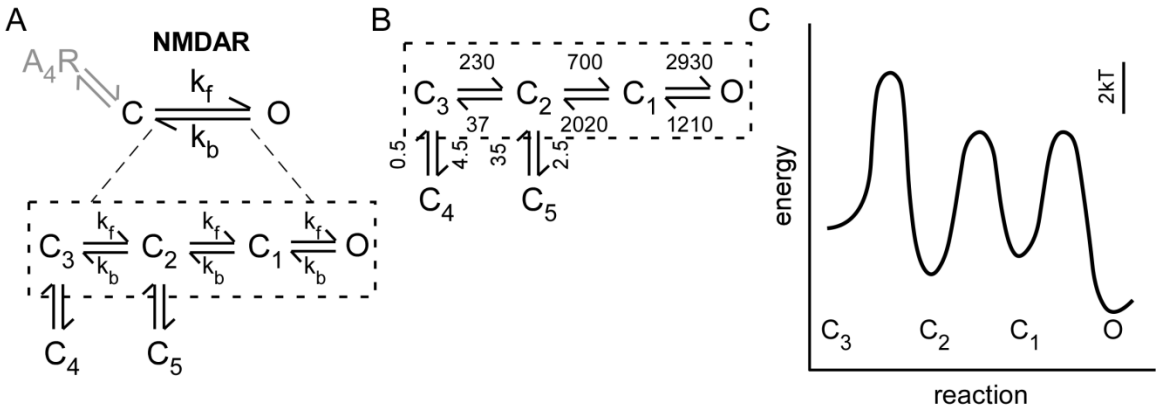

Figure 4.3 NMDAR pore opening.

(A) For NMDARs composed of GluN1/GluN2A, single-channel recordings have resolved multiple agonist-bound closed states (see text). Three of these closed states can be connected in a linear fashion to pore opening (C_3-C_2-C_1-O), and presumably represent relatively stable conformations of the agonist-bound closed state.
(B) Kinetic rates for the various transitions at equilibrium. (A & B) Boxed region highlights transitions independent of desensitization
(C) Energy-reaction plot for NMDAR opening (Talukder et al., 2011; Talukder and Wollmuth, 2011).
In the present context we will consider NMDARs in equilibrium where agonists (glutamate & glycine) are always present and hence, the closed and open states are presumed to be agonist-bound.

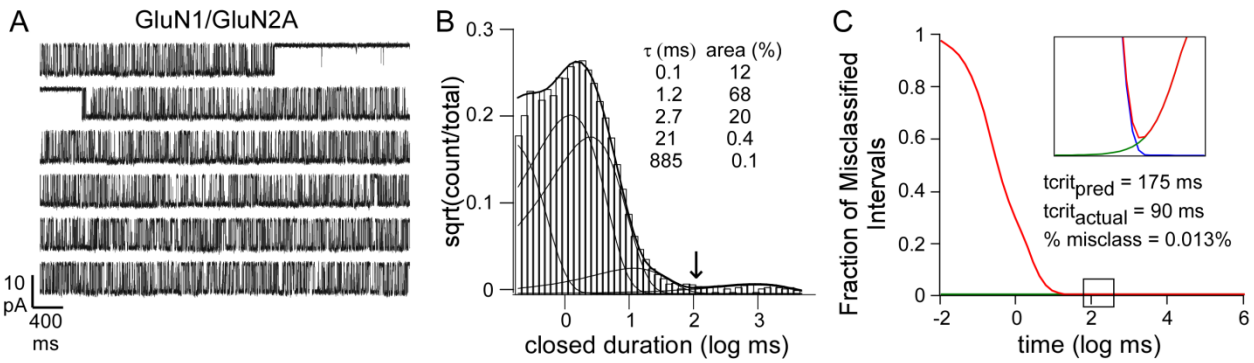

Figure 4.4 GluN1/GluN2A NMDAR burst analysis.

(A) Example low resolution trace of single channel activity from a GluN1/GluN2A NMDAR. Sampled at 40 kHz, shown digitally filtered at 1 kHz.
(B) Example closed state histogram for GluN1/GluN2A. This channel was best fit by five closed states, as is typical for GluN1/GluN2A NMDARs (see text). Also shown are the time constant (τ, ms) and % occupancy (area, %) for each of the states. Arrow highlights the derived t_{crit} between the 4^{th} and 5^{th} closed states.
(C) Plot displaying fraction of misclassified events when solving for t_{crit} between the 4^{th} and 5^{th} closed states. Red curve is the plot from Eq. 5 while the blue and green curves are the two components of the fit. The predicted t_{crit}, the used t_{crit}, and the % of misclassified events for the closed states displayed in B are shown.

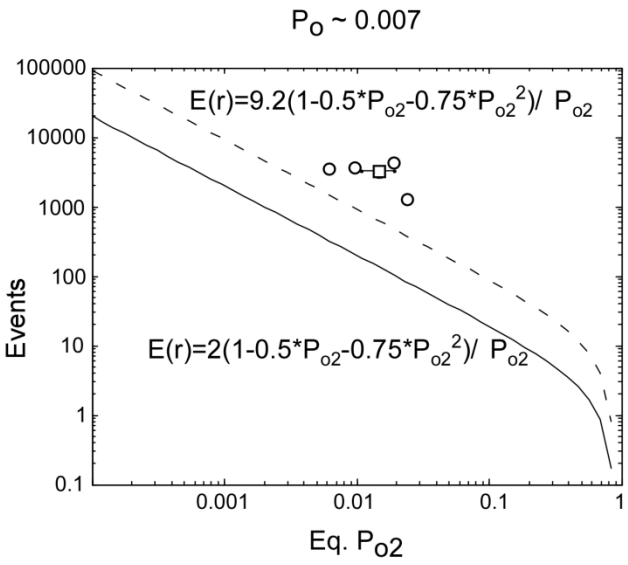

Figure 4.5 Statistical determination of single-channel patches

Plot used to calculate the confidence that there is a single channel in the patch. The black line reflects a ~50% confidence threshold while the dashed line reflects a ~99% confidence threshold. Representative equations are given. Example data points from four records (circles) and the mean (square, ±SEM). Mean P_o (0.007) is shown.

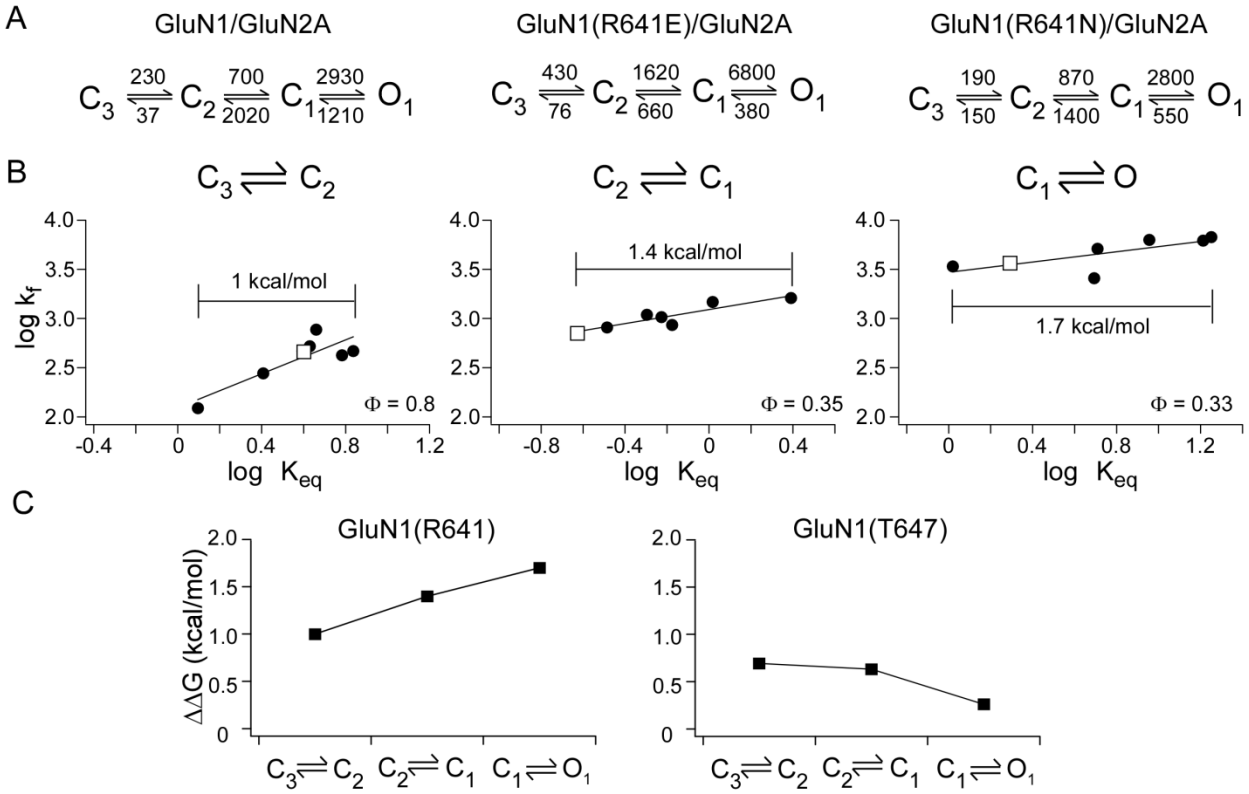

Figure 4.6 Energy of isomerization and ϕ analysis of pore opening.

(A) Manipulations at GluN1(R641) alter channel kinetics. MIL-derived kinetic models for GluN1/GluN2A, GluN1(R641E)/GluN2A, and GluN1(R641N)/GluN2A. Mean rates (s^{-1}) are shown.

(B) Φ-value plots for a series of substituted at GluN1(R641) for each kinetic transition. The energy of isomerization (ΔΔG) and Φ-value is indicated. White square represents values for wild type GluN1/GluN2A.

(C) Plots of isomerization energy for GluN1(R641) (left) and GluN1(T647) (right) during channel activation.

Transition		Burst Rate (s^{-1})	Equilibrium Rate (s^{-1})
C_3-C_2	k_f	290±37	230±30
	k_b	48±8.6	37±7
C_2-C_1	k_f	715±37	700±40
	k_b	2030±200	2020±190
C_1-O_1	k_f	2940±340	2930±340
	k_b	1210±150	1210±150
C_4-C_3	k_f		0.5±0.1
	k_b		4.5±1.0
C_5-C_2	k_f		35±15
	k_b		2.3±0.9
O_1-O_2	k_f	3940±320	3930±310
	k_b	575±47	575±47

Table 4.1 Burst and equilibrium kinetic analysis

Comparable rate constants for GluN1/GluN2A NMDARs (n = 8). Values are reported as mean ± SEM.

CONCLUDING REMARKS

Opening of ion channels on postsynaptic membranes is the key mechanism of neuron-to-neuron signaling. The efficiency of channel opening is determined by the thermodynamic rearrangements of these receptors. The focus of my work was to better understand the mechanisms of NMDAR opening and how this influences synaptic activation. From my work in Chapter 2, I was able to determine that channel opening in NMDARs required an efficient coupling mechanism between the LBD and M3 helix of the TMD. Specifically, the mechanism of energy transfer between the domains required a pulling mechanism. The NMDAR also contains two outer helices that are attached to the LBD and must presumably reposition to allow for pore widening to occur. Indeed, the results shown from Chapter 3 details that if the LBD-TMD linkers of these peripheral elements are physically restrained, then the efficiency of channel opening is significantly hindered. As such, efficient pore-opening requires that coupling mechanisms of both central and peripheral gating elements be preserved.

One of the primary challenges in determining channel opening is lack of resolution. Specifically, neurotransmitter-gated ion channels are too small to see and move too fast to track. To circumvent this, I employed the use of thermodynamic analysis of electrophysiological recordings to quantitatively distinguish the moving parts of the protein. Indeed, this approach, as detailed in Chapter 4, combines exhaustive mutagenesis with kinetic and thermodynamic means to determine “when” and “how much” specific amino acids move during channel opening. For example, my results show that positions proximal to the channel pore are much more dynamic and move close to the channel opening event. However, more distal positions tend to be less dynamic and move at earlier time points. While this analysis has been extremely fruitful in

delineating the movements of nAChRs and potassium channels, further work is necessary in iGluRs (Wang et al., 2011; Chowdhury and Chanda, 2012; Purohit et al., 2013).

A significant shortcoming of these approaches is that they rely heavily upon a specific gating model. Indeed, while kinetic modeling is one such way of describing channel opening, it can also deter one from making physiologically applicable conclusions. To that end, it is worthwhile to determine channel opening movements through techniques independent of a model. One such way is to use a simplified kinetic model. For example, a simple two-state model (closed to open) may be more useful. Indeed, when reanalyzing my data to fit a two-state model, it largely shows the same general trend as seen with the 5-state linear model. Future attempts can also use macroscopic tools such as rates of block or desensitization to understand the energetics of global rearrangements. Such methods have been applied successfully in potassium channels.

Optical tools may help determine real-time ion channel movements during gating. Fluorescence resonance energy transfer (FRET) can be combined with patch clamp electrophysiology to detect the relative movements of the protein (Zheng and Zagotta, 2003). Fluorometric approaches have been used in voltage-gated ion channels to determine relative protein movements as well (Kusch and Zifarelli, 2014). Indeed, the combination of imaging and electrophysiology can allow us to "see" protein movements and is entirely model independent. Novel cross-linking approaches have also shown successful in quantifying the timing of protein movements. We were able to successfully use a cysteine-substitution cross-linking approach to better understand this (see Chapter 3). Recently, artificial amino-acids that can form irreversible covalent cross-links upon light stimulation have been used to understand the movements of previously unexplored regions of the protein (Klippenstein et al., 2014). However, it is possible

that such cross-links lock the protein into unnatural conformations and therefore conclusions should be drawn cautiously.

Structural approaches provide amongst the greatest resolution of ion channels and how they may move. However, 3D atomic reconstruction falls short in that it lacks the fourth dimension: time. Most high-resolution crystal structures cannot detail exactly how a protein moves and therefore much of what is gained from these structures is speculative. Therefore, testing the predictions from protein structures is extremely critical. For example, it has proven beneficial in deciphering how desensitization progresses in AMPARs. Much can be learned from protein structures in different states and thus the crystal structure of an open state iGluR could solve many questions. This has proven technically challenging for x-ray crystallography. However, putative desensitized state structures have been solved, albeit at low-resolution, using NMR spectroscopy (Schauder et al., 2013). Further, FRET from isolated domains has also revealed novel structural changes following agonist binding (Landes et al., 2011; Sirrieh et al., 2013).

One way to utilize protein structures for determining the mechanics of gating is to use computational and theoretical approaches. As I showed in chapter 2, molecular-dynamics simulations were able to recapitulate the effects of M3-S2 mutations in silico. Indeed, molecular dynamics simulations have been able to correctly predict several gating phenomena in many ion channels, including iGluRs (Berneche and Roux, 2001; Lau and Roux, 2011; Ostmeyer et al., 2013). Further, simulations can reveal potential drug and ion binding targets and the mechanics of allostery. However, simulations have several drawbacks. While the theory is largely correct, the issue of environment as well as time resolution is an issue. It is possible that the environment in which simulations are run may not truly recapture the synapse. Indeed, it is the case that many

of the crystal structures used themselves may show structural features that are the result of crystal packing. Furthermore, there is the issue of time resolution. Due to computational limitations, the majority of simulations are only able to be run for a few hundred nanoseconds. Further, relevant pore opening rearrangements likely require hundreds of microseconds to milliseconds which is currently not attainable. This does not discount the predictions made from simulations and improved crystal structures can help guide simulations. Ultimately, the conclusions drawn from these approaches must be tested functionally and applied to the relevant physiology.

REFERENCES

Ahmed AH, Wang S, Chuang HH, Oswald RE (2011) Mechanism of AMPA receptor activation by partial agonists: disulfide trapping of closed lobe conformations. J Biol Chem 286:35257-35266.

Armstrong CM, Bezanilla F (1974) Charge movement associated with the opening and closing of the activation gates of the Na channels. The Journal of general physiology 63:533-552.

Armstrong N, Gouaux E (2000) Mechanisms for activation and antagonism of an AMPA-sensitive glutamate receptor: crystal structures of the GluR2 ligand binding core. Neuron 28:165-181.

Armstrong N, Mayer M, Gouaux E (2003) Tuning activation of the AMPA-sensitive GluR2 ion channel by genetic adjustment of agonist-induced conformational changes. Proc Natl Acad Sci U S A 100:5736-5741.

Auerbach A (2007) How to turn the reaction coordinate into time. The Journal of general physiology 130:543-546.

Auerbach A (2012) Thinking in cycles: MWC is a good model for acetylcholine receptor-channels. The Journal of physiology 590:93-98.

Auerbach A, Zhou Y (2005) Gating reaction mechanisms for NMDA receptor channels. J Neurosci 25:7914-7923.

Bach A, Clausen BH, Moller M, Vestergaard B, Chi CN, Round A, Sorensen PL, Nissen KB, Kastrup JS, Gajhede M, Jemth P, Kristensen AS, Lundstrom P, Lambertsen KL, Stromgaard K (2012) A high-affinity, dimeric inhibitor of PSD-95 bivalently interacts with PDZ1-2 and protects against ischemic brain damage. Proc Natl Acad Sci U S A 109:3317-3322.

Balannik V, Menniti FS, Paternain AV, Lerma J, Stern-Bach Y (2005) Molecular mechanism of AMPA receptor noncompetitive antagonism. Neuron 48:279-288.

Banke TG, Traynelis SF (2003) Activation of NR1/NR2B NMDA receptors. Nat Neurosci 6:144-152.

Benarroch EE (2011) NMDA receptors: recent insights and clinical correlations. Neurology 76:1750-1757.

Benveniste H, Drejer J, Schousboe A, Diemer NH (1984) Elevation of the extracellular concentrations of glutamate and aspartate in rat hippocampus during transient cerebral ischemia monitored by intracerebral microdialysis. J Neurochem 43:1369-1374.

Berneche S, Roux B (2001) Energetics of ion conduction through the K+ channel. Nature 414:73-77.

Bezanilla F, White MM, Taylor RE (1982) Gating currents associated with potassium channel activation. Nature 296:657-659.

Birdsey-Benson A, Gill A, Henderson LP, Madden DR (2010) Enhanced efficacy without further cleft closure: reevaluating twist as a source of agonist efficacy in AMPA receptors. J Neurosci 30:1463-1470.

Blanke ML, VanDongen AM (2008) Constitutive activation of the N-methyl-D-aspartate receptor via cleft-spanning disulfide bonds. J Biol Chem 283:21519-21529.

Bordoli L, Kiefer F, Arnold K, Benkert P, Battey J, Schwede T (2009) Protein structure homology modeling using SWISS-MODEL workspace. Nat Protoc 4:1-13.

Borschel WF, Murthy SE, Kasperek EM, Popescu GK (2011) NMDA receptor activation requires remodelling of intersubunit contacts within ligand-binding heterodimers. Nat Commun 2:498.
Brocher S, Artola A, Singer W (1992) Intracellular injection of Ca2+ chelators blocks induction of long-term depression in rat visual cortex. Proc Natl Acad Sci U S A 89:123-127.
Burnashev N, Zhou Z, Neher E, Sakmann B (1995) Fractional calcium currents through recombinant GluR channels of the NMDA, AMPA and kainate receptor subtypes. The Journal of physiology 485 (Pt 2):403-418.
Burzomato V, Beato M, Groot-Kormelink PJ, Colquhoun D, Sivilotti LG (2004) Single-channel behavior of heteromeric alpha1beta glycine receptors: an attempt to detect a conformational change before the channel opens. J Neurosci 24:10924-10940.
Carvill GL et al. (2013) GRIN2A mutations cause epilepsy-aphasia spectrum disorders. Nat Genet 45:1073-1076.
Chang HR, Kuo CC (2008) The activation gate and gating mechanism of the NMDA receptor. J Neurosci 28:1546-1556.
Chen GQ, Cui C, Mayer ML, Gouaux E (1999) Functional characterization of a potassium-selective prokaryotic glutamate receptor. Nature 402:817-821.
Choi DW, Koh JY, Peters S (1988) Pharmacology of glutamate neurotoxicity in cortical cell culture: attenuation by NMDA antagonists. J Neurosci 8:185-196.
Chowdhury S, Chanda B (2012) Estimating the voltage-dependent free energy change of ion channels using the median voltage for activation. The Journal of general physiology 139:3-17.
Christine CW, Choi DW (1990) Effect of zinc on NMDA receptor-mediated channel currents in cortical neurons. J Neurosci 10:108-116.
Christoffersen CL, Meltzer LT (1995) Evidence for N-methyl-D-aspartate and AMPA subtypes of the glutamate receptor on substantia nigra dopamine neurons: possible preferential role for N-methyl-D-aspartate receptors. Neuroscience 67:373-381.
Citri A, Malenka RC (2008) Synaptic plasticity: multiple forms, functions, and mechanisms. Neuropsychopharmacology 33:18-41.
Clarke RJ, Johnson JW (2008) Voltage-dependent gating of NR1/2B NMDA receptors. The Journal of physiology 586:5727-5741.
Clements JD, Lester RA, Tong G, Jahr CE, Westbrook GL (1992) The time course of glutamate in the synaptic cleft. Science 258:1498-1501.
Collingridge GL, Kehl SJ, McLennan H (1983) Excitatory amino acids in synaptic transmission in the Schaffer collateral-commissural pathway of the rat hippocampus. The Journal of physiology 334:33-46.
Colquhoun D, Hawkes AG (1990a) Stochastic Properties of Ion Channel Openings and Bursts in a Membrane Patch That Contains 2 Channels - Evidence Concerning the Number of Channels Present When a Record Containing Only Single Openings Is Observed. Proc R Soc Ser B-Bio 240:453-477.
Colquhoun D, Hawkes AG (1990b) Stochastic properties of ion channel openings and bursts in a membrane patch that contains two channels: evidence concerning the number of channels present when a record containing only single openings is observed. Proc R Soc Lond B Biol Sci 240:453-477.

Colquhoun D, Lape R (2012) Perspectives on: Conformational coupling in ion channels: Allosteric coupling in ligand-gated ion channels. The Journal of general physiology 140:599-612.
Dacosta CJ, Baenziger JE (2013) Gating of pentameric ligand-gated ion channels: structural insights and ambiguities. Structure 21:1271-1283.
Dai J, Zhou HX (2013) An NMDA receptor gating mechanism developed from MD simulations reveals molecular details underlying subunit-specific contributions. Biophysical journal 104:2170-2181.
Diamond JS, Jahr CE (1995) Asynchronous release of synaptic vesicles determines the time course of the AMPA receptor-mediated EPSC. Neuron 15:1097-1107.
Dingledine R, Borges K, Bowie D, Traynelis SF (1999) The glutamate receptor ion channels. Pharmacol Rev 51:7-61.
Dong H, Zhou HX (2011) Atomistic mechanism for the activation and desensitization of an AMPA-subtype glutamate receptor. Nat Commun 2:354.
Doyle DA, Morais Cabral J, Pfuetzner RA, Kuo A, Gulbis JM, Cohen SL, Chait BT, MacKinnon R (1998) The structure of the potassium channel: molecular basis of K+ conduction and selectivity. Science 280:69-77.
Dravid SM, Prakash A, Traynelis SF (2008) Activation of recombinant NR1/NR2C NMDA receptors. The Journal of physiology 586:4425-4439.
Endele S et al. (2010) Mutations in GRIN2A and GRIN2B encoding regulatory subunits of NMDA receptors cause variable neurodevelopmental phenotypes. Nat Genet 42:1021-1026.
Erreger K, Traynelis SF (2008) Zinc inhibition of rat NR1/NR2A N-methyl-D-aspartate receptors. The Journal of physiology 586:763-778.
Erreger K, Dravid SM, Banke TG, Wyllie DJ, Traynelis SF (2005a) Subunit-specific gating controls rat NR1/NR2A and NR1/NR2B NMDA channel kinetics and synaptic signalling profiles. The Journal of physiology 563:345-358.
Erreger K, Geballe MT, Dravid SM, Snyder JP, Wyllie DJ, Traynelis SF (2005b) Mechanism of partial agonism at NMDA receptors for a conformationally restricted glutamate analog. J Neurosci 25:7858-7866.
Fersht AR, Sato S (2004) Phi-value analysis and the nature of protein-folding transition states. Proc Natl Acad Sci U S A 101:7976-7981.
Forti L, Bossi M, Bergamaschi A, Villa A, Malgaroli A (1997) Loose-patch recordings of single quanta at individual hippocampal synapses. Nature 388:874-878.
Furukawa H (2012) Structure and function of glutamate receptor amino terminal domains. The Journal of physiology 590:63-72.
Furukawa H, Gouaux E (2003) Mechanisms of activation, inhibition and specificity: crystal structures of the NMDA receptor NR1 ligand-binding core. EMBO J 22:2873-2885.
Furukawa H, Singh SK, Mancusso R, Gouaux E (2005) Subunit arrangement and function in NMDA receptors. Nature 438:185-192.
Gardoni F, Sgobio C, Pendolino V, Calabresi P, Di Luca M, Picconi B (2012) Targeting NR2A-containing NMDA receptors reduces L-DOPA-induced dyskinesias. Neurobiol Aging 33:2138-2144.
Ghasemi M, Schachter SC (2011) The NMDA receptor complex as a therapeutic target in epilepsy: a review. Epilepsy Behav 22:617-640.

Gibb AJ, Colquhoun D (1991) Glutamate activation of a single NMDA receptor-channel produces a cluster of channel openings. Proc Biol Sci 243:39-45.
Gibb AJ, Colquhoun D (1992) Activation of N-methyl-D-aspartate receptors by L-glutamate in cells dissociated from adult rat hippocampus. The Journal of physiology 456:143-179.
Gielen M, Siegler Retchless B, Mony L, Johnson JW, Paoletti P (2009) Mechanism of differential control of NMDA receptor activity by NR2 subunits. Nature 459:703-707.
Grosman C, Auerbach A (2000) Kinetic, mechanistic, and structural aspects of unliganded gating of acetylcholine receptor channels: a single-channel study of second transmembrane segment 12' mutants. The Journal of general physiology 115:621-635.
Hamdan FF et al. (2011) Excess of de novo deleterious mutations in genes associated with glutamatergic systems in nonsyndromic intellectual disability. Am J Hum Genet 88:306-316.
Hansen KB, Traynelis SF (2011) Structural and mechanistic determinants of a novel site for noncompetitive inhibition of GluN2D-containing NMDA receptors. J Neurosci 31:3650-3661.
Hansen KB, Yuan H, Traynelis SF (2007) Structural aspects of AMPA receptor activation, desensitization and deactivation. Curr Opin Neurobiol 17:281-288.
Hansen KB, Furukawa H, Traynelis SF (2010) Control of assembly and function of glutamate receptors by the amino-terminal domain. Mol Pharmacol 78:535-549.
Hardingham GE, Bading H (2010) Synaptic versus extrasynaptic NMDA receptor signalling: implications for neurodegenerative disorders. Nat Rev Neurosci 11:682-696.
Harris EW, Ganong AH, Cotman CW (1984) Long-term potentiation in the hippocampus involves activation of N-methyl-D-aspartate receptors. Brain Res 323:132-137.
Hattori M, Gouaux E (2012) Molecular mechanism of ATP binding and ion channel activation in P2X receptors. Nature 485:207-212.
Hebb DO (1949) The organization of behavior; a neuropsychological theory. New York,: Wiley.
Hibbs RE, Gouaux E (2011) Principles of activation and permeation in an anion-selective Cys-loop receptor. Nature 474:54-60.
Hilf RJ, Dutzler R (2008) X-ray structure of a prokaryotic pentameric ligand-gated ion channel. Nature 452:375-379.
Hilf RJ, Dutzler R (2009) Structure of a potentially open state of a proton-activated pentameric ligand-gated ion channel. Nature 457:115-118.
Hille B (2001) Ion channels of excitable membranes, 3rd Edition. Sunderland, Mass.: Sinauer.
Hodgkin AL, Huxley AF (1952) A quantitative description of membrane current and its application to conduction and excitation in nerve. The Journal of physiology 117:500-544.
Howe JR, Cull-Candy SG, Colquhoun D (1991) Currents through single glutamate receptor channels in outside-out patches from rat cerebellar granule cells. The Journal of physiology 432:143-202.
Huggins DJ, Grant GH (2005) The function of the amino terminal domain in NMDA receptor modulation. J Mol Graph Model 23:381-388.
Humphrey W, Dalke A, Schulten K (1996) VMD: visual molecular dynamics. J Mol Graph 14:33-38, 27-38.
Inanobe A, Furukawa H, Gouaux E (2005) Mechanism of partial agonist action at the NR1 subunit of NMDA receptors. Neuron 47:71-84.

Isaacson JS, Walmsley B (1995) Counting quanta: direct measurements of transmitter release at a central synapse. Neuron 15:875-884.
Jackson MB (1986) Kinetics of unliganded acetylcholine receptor channel gating. Biophysical journal 49:663-672.
Jackson MB, Wong BS, Morris CE, Lecar H, Christian CN (1983) Successive openings of the same acetylcholine receptor channel are correlated in open time. Biophysical journal 42:109-114.
Jin R, Banke TG, Mayer ML, Traynelis SF, Gouaux E (2003) Structural basis for partial agonist action at ionotropic glutamate receptors. Nat Neurosci 6:803-810.
Johnson JW, Ascher P (1987) Glycine potentiates the NMDA response in cultured mouse brain neurons. Nature 325:529-531.
Jones KS, VanDongen HM, VanDongen AM (2002) The NMDA receptor M3 segment is a conserved transduction element coupling ligand binding to channel opening. J Neurosci 22:2044-2053.
Jones S, Bonci A (2005) Synaptic plasticity and drug addiction. Curr Opin Pharmacol 5:20-25.
Karakas E, Simorowski N, Furukawa H (2009) Structure of the zinc-bound amino-terminal domain of the NMDA receptor NR2B subunit. EMBO J 28:3910-3920.
Karakas E, Simorowski N, Furukawa H (2011) Subunit arrangement and phenylethanolamine binding in GluN1/GluN2B NMDA receptors. Nature 475:249-253.
Kaye SL, Sansom MS, Biggin PC (2006) Molecular dynamics simulations of the ligand-binding domain of an N-methyl-D-aspartate receptor. J Biol Chem 281:12736-12742.
Kazi R, Gan Q, Talukder I, Markowitz M, Salussolia CL, Wollmuth LP (2013) Asynchronous movements prior to pore opening in NMDA receptors. J Neurosci 33:12052-12066.
Kelley LA, Sternberg MJ (2009) Protein structure prediction on the Web: a case study using the Phyre server. Nat Protoc 4:363-371.
Kleckner NW, Dingledine R (1988) Requirement for glycine in activation of NMDA-receptors expressed in Xenopus oocytes. Science 241:835-837.
Klippenstein V, Ghisi V, Wietstruk M, Plested AJ (2014) Photoinactivation of glutamate receptors by genetically encoded unnatural amino acids. J Neurosci 34:980-991.
Kristensen AS, Jenkins MA, Banke TG, Schousboe A, Makino Y, Johnson RC, Huganir R, Traynelis SF (2011) Mechanism of Ca2+/calmodulin-dependent kinase II regulation of AMPA receptor gating. Nat Neurosci 14:727-735.
Krupp JJ, Vissel B, Heinemann SF, Westbrook GL (1996) Calcium-dependent inactivation of recombinant N-methyl-D-aspartate receptors is NR2 subunit specific. Mol Pharmacol 50:1680-1688.
Krupp JJ, Vissel B, Heinemann SF, Westbrook GL (1998) N-terminal domains in the NR2 subunit control desensitization of NMDA receptors. Neuron 20:317-327.
Kuner T, Schoepfer R (1996) Multiple structural elements determine subunit specificity of Mg2+ block in NMDA receptor channels. J Neurosci 16:3549-3558.
Kuner T, Seeburg PH, Guy HR (2003) A common architecture for K+ channels and ionotropic glutamate receptors? Trends Neurosci 26:27-32.
Kuner T, Beck C, Sakmann B, Seeburg PH (2001) Channel-lining residues of the AMPA receptor M2 segment: structural environment of the Q/R site and identification of the selectivity filter. J Neurosci 21:4162-4172.
Kusch J, Zifarelli G (2014) Patch-Clamp Fluorometry: Electrophysiology meets Fluorescence. Biophysical journal 106:1250-1257.

Kussius CL, Popescu GK (2009) Kinetic basis of partial agonism at NMDA receptors. Nat Neurosci 12:1114-1120.
Kussius CL, Popescu GK (2010) NMDA receptors with locked glutamate-binding clefts open with high efficacy. J Neurosci 30:12474-12479.
Kussius CL, Popescu AM, Popescu GK (2010) Agonist-specific gating of NMDA receptors. Channels (Austin) 4:78-82.
Lai TW, Shyu WC, Wang YT (2011) Stroke intervention pathways: NMDA receptors and beyond. Trends Mol Med 17:266-275.
Landes CF, Rambhadran A, Taylor JN, Salatan F, Jayaraman V (2011) Structural landscape of isolated agonist-binding domains from single AMPA receptors. Nat Chem Biol 7:168-173.
Lau AY, Roux B (2011) The hidden energetics of ligand binding and activation in a glutamate receptor. Nat Struct Mol Biol 18:283-287.
Lau AY, Salazar H, Blachowicz L, Ghisi V, Plested AJ, Roux B (2013) A conformational intermediate in glutamate receptor activation. Neuron 79:492-503.
Lee CH, Gouaux E (2011) Amino terminal domains of the NMDA receptor are organized as local heterodimers. PLoS One 6:e19180.
Lee WY, Sine SM (2005) Principal pathway coupling agonist binding to channel gating in nicotinic receptors. Nature 438:243-247.
Lemke JR, Hendrickx R, Geider K, Laube B, Schwake M, Harvey RJ, James VM, Pepler A, Steiner I, Hortnagel K, Neidhardt J, Ruf S, Wolff M, Bartholdi D, Caraballo R, Platzer K, Suls A, De Jonghe P, Biskup S, Weckhuysen S (2014) GRIN2B mutations in West syndrome and intellectual disability with focal epilepsy. Ann Neurol 75:147-154.
Lemke JR et al. (2013) Mutations in GRIN2A cause idiopathic focal epilepsy with rolandic spikes. Nat Genet 45:1067-1072.
Lerma J, Zukin RS, Bennett MV (1990) Glycine decreases desensitization of N-methyl-D-aspartate (NMDA) receptors expressed in Xenopus oocytes and is required for NMDA responses. Proc Natl Acad Sci U S A 87:2354-2358.
Lesca G et al. (2013) GRIN2A mutations in acquired epileptic aphasia and related childhood focal epilepsies and encephalopathies with speech and language dysfunction. Nat Genet 45:1061-1066.
Lester RA, Jahr CE (1992) NMDA channel behavior depends on agonist affinity. J Neurosci 12:635-643.
Lester RA, Clements JD, Westbrook GL, Jahr CE (1990) Channel kinetics determine the time course of NMDA receptor-mediated synaptic currents. Nature 346:565-567.
Liu X, Xu Y, Li H, Wang X, Jiang H, Barrantes FJ (2008) Mechanics of channel gating of the nicotinic acetylcholine receptor. PLoS Comput Biol 4:e19.
Long SB, Campbell EB, Mackinnon R (2005) Crystal structure of a mammalian voltage-dependent Shaker family K+ channel. Science 309:897-903.
Luscher C, Malenka RC (2011) Drug-evoked synaptic plasticity in addiction: from molecular changes to circuit remodeling. Neuron 69:650-663.
Mackerell AD, Jr., Feig M, Brooks CL, 3rd (2004) Extending the treatment of backbone energetics in protein force fields: limitations of gas-phase quantum mechanics in reproducing protein conformational distributions in molecular dynamics simulations. J Comput Chem 25:1400-1415.

Malenka RC, Kauer JA, Zucker RS, Nicoll RA (1988) Postsynaptic calcium is sufficient for potentiation of hippocampal synaptic transmission. Science 242:81-84.
Martel MA, Ryan TJ, Bell KF, Fowler JH, McMahon A, Al-Mubarak B, Komiyama NH, Horsburgh K, Kind PC, Grant SG, Wyllie DJ, Hardingham GE (2012) The subtype of GluN2 C-terminal domain determines the response to excitotoxic insults. Neuron 74:543-556.
Matouschek A, Kellis JT, Jr., Serrano L, Fersht AR (1989) Mapping the transition state and pathway of protein folding by protein engineering. Nature 340:122-126.
Mayer ML (2006) Glutamate receptors at atomic resolution. Nature 440:456-462.
Mayer ML (2011) Structure and mechanism of glutamate receptor ion channel assembly, activation and modulation. Curr Opin Neurobiol.
Mayer ML, Westbrook GL, Guthrie PB (1984) Voltage-dependent block by Mg2+ of NMDA responses in spinal cord neurones. Nature 309:261-263.
Mayer ML, Olson R, Gouaux E (2001) Mechanisms for ligand binding to GluR0 ion channels: crystal structures of the glutamate and serine complexes and a closed apo state. J Mol Biol 311:815-836.
Merlo C, Dill KA, Weikl TR (2005) Phi values in protein-folding kinetics have energetic and structural components. Proc Natl Acad Sci U S A 102:10171-10175.
Miyazawa A, Fujiyoshi Y, Unwin N (2003) Structure and gating mechanism of the acetylcholine receptor pore. Nature 423:949-955.
Monod J, Wyman J, Changeux JP (1965) On the Nature of Allosteric Transitions: A Plausible Model. J Mol Biol 12:88-118.
Monyer H, Burnashev N, Laurie DJ, Sakmann B, Seeburg PH (1994) Developmental and regional expression in the rat brain and functional properties of four NMDA receptors. Neuron 12:529-540.
Mothet JP, Parent AT, Wolosker H, Brady RO, Jr., Linden DJ, Ferris CD, Rogawski MA, Snyder SH (2000) D-serine is an endogenous ligand for the glycine site of the N-methyl-D-aspartate receptor. Proc Natl Acad Sci U S A 97:4926-4931.
Mulkey RM, Malenka RC (1992) Mechanisms underlying induction of homosynaptic long-term depression in area CA1 of the hippocampus. Neuron 9:967-975.
Murthy SE, Shogan T, Page JC, Kasperek EM, Popescu GK (2012) Probing the activation sequence of NMDA receptors with lurcher mutations. The Journal of general physiology 140:267-277.
Niu X, Qian X, Magleby KL (2004) Linker-gating ring complex as passive spring and Ca(2+)-dependent machine for a voltage- and Ca(2+)-activated potassium channel. Neuron 42:745-756.
Nowak L, Bregestovski P, Ascher P, Herbet A, Prochiantz A (1984) Magnesium gates glutamate-activated channels in mouse central neurones. Nature 307:462-465.
Ogden KK, Traynelis SF (2013) Contribution of the M1 transmembrane helix and pre-M1 region to positive allosteric modulation and gating of N-methyl-D-aspartate receptors. Mol Pharmacol 83:1045-1056.
Olney JW, Sharpe LG, Feigin RD (1972) Glutamate-induced brain damage in infant primates. J Neuropathol Exp Neurol 31:464-488.
Ostmeyer J, Chakrapani S, Pan AC, Perozo E, Roux B (2013) Recovery from slow inactivation in K+ channels is controlled by water molecules. Nature 501:121-124.

Ozkan SB, Bahar I, Dill KA (2001) Transition states and the meaning of Phi-values in protein folding kinetics. Nat Struct Biol 8:765-769.
Pallotta BS (1985) Calcium-activated potassium channels in rat muscle inactivate from a short-duration open state. The Journal of physiology 363:501-516.
Panatier A, Theodosis DT, Mothet JP, Touquet B, Pollegioni L, Poulain DA, Oliet SH (2006) Glia-derived D-serine controls NMDA receptor activity and synaptic memory. Cell 125:775-784.
Panchenko VA, Glasser CR, Mayer ML (2001) Structural similarities between glutamate receptor channels and K(+) channels examined by scanning mutagenesis. The Journal of general physiology 117:345-360.
Paoletti P, Ascher P, Neyton J (1997) High-affinity zinc inhibition of NMDA NR1-NR2A receptors. J Neurosci 17:5711-5725.
Paoletti P, Bellone C, Zhou Q (2013) NMDA receptor subunit diversity: impact on receptor properties, synaptic plasticity and disease. Nat Rev Neurosci 14:383-400.
Phillips JC, Braun R, Wang W, Gumbart J, Tajkhorshid E, Villa E, Chipot C, Skeel RD, Kale L, Schulten K (2005) Scalable molecular dynamics with NAMD. J Comput Chem 26:1781-1802.
Popescu G, Auerbach A (2003) Modal gating of NMDA receptors and the shape of their synaptic response. Nat Neurosci 6:476-483.
Prieto ML, Wollmuth LP (2010) Gating modes in AMPA receptors. J Neurosci 30:4449-4459.
Purohit P, Auerbach A (2009) Unliganded gating of acetylcholine receptor channels. Proc Natl Acad Sci U S A 106:115-120.
Purohit P, Mitra A, Auerbach A (2007) A stepwise mechanism for acetylcholine receptor channel gating. Nature 446:930-933.
Purohit P, Gupta S, Jadey S, Auerbach A (2013) Functional anatomy of an allosteric protein. Nat Commun 4:2984.
Purohit Y, Grosman C (2006) Estimating binding affinities of the nicotinic receptor for low-efficacy ligands using mixtures of agonists and two-dimensional concentration-response relationships. The Journal of general physiology 127:719-735.
Qian A, Johnson JW (2002) Channel gating of NMDA receptors. Physiol Behav 77:577-582.
Qin F, Auerbach A, Sachs F (2000a) A direct optimization approach to hidden Markov modeling for single channel kinetics. Biophysical journal 79:1915-1927.
Qin F, Auerbach A, Sachs F (2000b) Hidden Markov modeling for single channel kinetics with filtering and correlated noise. Biophysical journal 79:1928-1944.
Raghavachari S, Lisman JE (2004) Properties of quantal transmission at CA1 synapses. J Neurophysiol 92:2456-2467.
Raleigh DP, Plaxco KW (2005) The protein folding transition state: what are Phi-values really telling us? Protein Pept Lett 12:117-122.
Ramaswamy S, Cooper D, Poddar N, Maclean DM, Rambhadran A, Taylor JN, Uhm H, Landes C, Jayaraman V (2012a) Role of conformational dynamics in alpha-amino-3-hydroxy-5-methylisoxazole-4-propionic acid (AMPA) receptor partial agonism. J Biol Chem.
Ramaswamy S, Cooper D, Poddar N, MacLean DM, Rambhadran A, Taylor JN, Uhm H, Landes CF, Jayaraman V (2012b) Role of conformational dynamics in alpha-amino-3-hydroxy-5-methylisoxazole-4-propionic acid (AMPA) receptor partial agonism. J Biol Chem 287:43557-43564.

Rambhadran A, Gonzalez J, Jayaraman V (2011) Conformational changes at the agonist binding domain of the N-methyl-D-aspartic acid receptor. J Biol Chem 286:16953-16957.
Regalado MP, Villarroel A, Lerma J (2001) Intersubunit cooperativity in the NMDA receptor. Neuron 32:1085-1096.
Ren H, Zhao Y, Dwyer DS, Peoples RW (2012) Interactions among Positions in the Third and Fourth Membrane-associated Domains at the Intersubunit Interface of the N-Methyl-D-aspartate Receptor Forming Sites of Alcohol Action. J Biol Chem 287:27302-27312.
Riou M, Stroebel D, Edwardson JM, Paoletti P (2012) An alternating GluN1-2-1-2 subunit arrangement in mature NMDA receptors. PLoS One 7:e35134.
Robert A, Armstrong N, Gouaux JE, Howe JR (2005) AMPA receptor binding cleft mutations that alter affinity, efficacy, and recovery from desensitization. J Neurosci 25:3752-3762.
Rosenmund C, Feltz A, Westbrook GL (1995) Calcium-dependent inactivation of synaptic NMDA receptors in hippocampal neurons. J Neurophysiol 73:427-430.
Rosenmund C, Stern-Bach Y, Stevens CF (1998) The tetrameric structure of a glutamate receptor channel. Science 280:1596-1599.
Sali A, Blundell TL (1993) Comparative protein modelling by satisfaction of spatial restraints. J Mol Biol 234:779-815.
Salussolia CL, Prodromou ML, Borker P, Wollmuth LP (2011a) Arrangement of subunits in functional NMDA receptors. J Neurosci 31:11295-11304.
Salussolia CL, Corrales A, Talukder I, Kazi R, Akgul G, Bowen M, Wollmuth LP (2011b) Interaction of the M4 segment with other transmembrane segments is required for surface expression of mammalian alpha-amino-3-hydroxy-5-methyl-4-isoxazolepropionic acid (AMPA) receptors. J Biol Chem 286:40205-40218.
Schauder DM, Kuybeda O, Zhang J, Klymko K, Bartesaghi A, Borgnia MJ, Mayer ML, Subramaniam S (2013) Glutamate receptor desensitization is mediated by changes in quaternary structure of the ligand binding domain. Proc Natl Acad Sci U S A 110:5921-5926.
Schmid SM, Korber C, Herrmann S, Werner M, Hollmann M (2007) A domain linking the AMPA receptor agonist binding site to the ion pore controls gating and causes lurcher properties when mutated. J Neurosci 27:12230-12241.
Schneggenburger R (1996) Simultaneous measurement of Ca2+ influx and reversal potentials in recombinant N-methyl-D-aspartate receptor channels. Biophysical journal 70:2165-2174.
Schorge S, Elenes S, Colquhoun D (2005) Maximum likelihood fitting of single channel NMDA activity with a mechanism composed of independent dimers of subunits. The Journal of physiology 569:395-418.
Schwarz G (1978) Estimating Dimension of a Model. Ann Stat 6:461-464.
Sgambato-Faure V, Cenci MA (2012) Glutamatergic mechanisms in the dyskinesias induced by pharmacological dopamine replacement and deep brain stimulation for the treatment of Parkinson's disease. Prog Neurobiol 96:69-86.
Siegler Retchless B, Gao W, Johnson JW (2012) A single GluN2 subunit residue controls NMDA receptor channel properties via intersubunit interaction. Nat Neurosci 15:406-413, S401-402.
Sirrieh RE, MacLean DM, Jayaraman V (2013) Amino-terminal domain tetramer organization and structural effects of zinc binding in the N-methyl-D-aspartate (NMDA) receptor. J Biol Chem 288:22555-22564.

Smart OS, Goodfellow JM, Wallace BA (1993) The pore dimensions of gramicidin A. Biophysical journal 65:2455-2460.
Smith MA, Ellis-Davies GC, Magee JC (2003) Mechanism of the distance-dependent scaling of Schaffer collateral synapses in rat CA1 pyramidal neurons. The Journal of physiology 548:245-258.
Smith TC, Howe JR (2000) Concentration-dependent substate behavior of native AMPA receptors. Nat Neurosci 3:992-997.
Sobolevsky AI, Beck C, Wollmuth LP (2002) Molecular rearrangements of the extracellular vestibule in NMDAR channels during gating. Neuron 33:75-85.
Sobolevsky AI, Rosconi MP, Gouaux E (2009) X-ray structure, symmetry and mechanism of an AMPA-subtype glutamate receptor. Nature 462:745-756.
Sobolevsky AI, Prodromou ML, Yelshansky MV, Wollmuth LP (2007) Subunit-specific contribution of pore-forming domains to NMDA receptor channel structure and gating. The Journal of general physiology 129:509-525.
Soderling TR, Derkach VA (2000) Postsynaptic protein phosphorylation and LTP. Trends Neurosci 23:75-80.
Standaert DG, Testa CM, Young AB, Penney JB, Jr. (1994) Organization of N-methyl-D-aspartate glutamate receptor gene expression in the basal ganglia of the rat. J Comp Neurol 343:1-16.
Stuhmer W (1991) Structure-function studies of voltage-gated ion channels. Annu Rev Biophys Biophys Chem 20:65-78.
Sun Y, Olson R, Horning M, Armstrong N, Mayer M, Gouaux E (2002) Mechanism of glutamate receptor desensitization. Nature 417:245-253.
Swanson GT, Kamboj SK, Cull-Candy SG (1997) Single-channel properties of recombinant AMPA receptors depend on RNA editing, splice variation, and subunit composition. J Neurosci 17:58-69.
Talukder I, Wollmuth LP (2011) Local constraints in either the GluN1 or GluN2 subunit equally impair NMDA receptor pore opening. The Journal of general physiology 138:179-194.
Talukder I, Borker P, Wollmuth LP (2010) Specific sites within the ligand-binding domain and ion channel linkers modulate NMDA receptor gating. J Neurosci 30:11792-11804.
Talukder I, Kazi R, Wollmuth LP (2011) GluN1-specific redox effects on the kinetic mechanism of NMDA receptor activation. Biophysical journal 101:2389-2398.
Tarabeux J et al. (2011) Rare mutations in N-methyl-D-aspartate glutamate receptors in autism spectrum disorders and schizophrenia. Transl Psychiatry 1:e55.
Traynelis SF, Wollmuth LP, McBain CJ, Menniti FS, Vance KM, Ogden KK, Hansen KB, Yuan H, Myers SJ, Dingledine R, Sibley D (2010) Glutamate receptor ion channels: structure, regulation, and function. Pharmacol Rev 62:405-496.
Tu W, Xu X, Peng L, Zhong X, Zhang W, Soundarapandian MM, Balel C, Wang M, Jia N, Lew F, Chan SL, Chen Y, Lu Y (2010) DAPK1 interaction with NMDA receptor NR2B subunits mediates brain damage in stroke. Cell 140:222-234.
Van Hove J, Coughlin C, Scharer G (1993) Glycine Encephalopathy.
Vance KM, Simorowski N, Traynelis SF, Furukawa H (2011) Ligand-specific deactivation time course of GluN1/GluN2D NMDA receptors. Nat Commun 2:294.
Villarroel A, Regalado MP, Lerma J (1998) Glycine-independent NMDA receptor desensitization: localization of structural determinants. Neuron 20:329-339.

Villmann C, Becker CM (2007) On the hypes and falls in neuroprotection: targeting the NMDA receptor. Neuroscientist 13:594-615.
Wang DT, Hill AP, Mann SA, Tan PS, Vandenberg JI (2011) Mapping the sequence of conformational changes underlying selectivity filter gating in the K(v)11.1 potassium channel. Nat Struct Mol Biol 18:35-41.
Watanabe J, Beck C, Kuner T, Premkumar LS, Wollmuth LP (2002) DRPEER: a motif in the extracellular vestibule conferring high Ca2+ flux rates in NMDA receptor channels. J Neurosci 22:10209-10216.
Weston MC, Schuck P, Ghosal A, Rosenmund C, Mayer ML (2006) Conformational restriction blocks glutamate receptor desensitization. Nat Struct Mol Biol 13:1120-1127.
Williams K (2001) Ifenprodil, a novel NMDA receptor antagonist: site and mechanism of action. Curr Drug Targets 2:285-298.
Wo ZG, Oswald RE (1995) Unraveling the modular design of glutamate-gated ion channels. Trends Neurosci 18:161-168.
Wollmuth LP, Sobolevsky AI (2004) Structure and gating of the glutamate receptor ion channel. Trends Neurosci 27:321-328.
Wollmuth LP, Kuner T, Sakmann B (1998a) Intracellular Mg2+ interacts with structural determinants of the narrow constriction contributed by the NR1-subunit in the NMDA receptor channel. The Journal of physiology 506 (Pt 1):33-52.
Wollmuth LP, Kuner T, Sakmann B (1998b) Adjacent asparagines in the NR2-subunit of the NMDA receptor channel control the voltage-dependent block by extracellular Mg2+. The Journal of physiology 506 (Pt 1):13-32.
Wollmuth LP, Kuner T, Seeburg PH, Sakmann B (1996) Differential contribution of the NR1- and NR2A-subunits to the selectivity filter of recombinant NMDA receptor channels. The Journal of physiology 491 (Pt 3):779-797.
Wood MW, VanDongen HM, VanDongen AM (1995) Structural conservation of ion conduction pathways in K channels and glutamate receptors. Proc Natl Acad Sci U S A 92:4882-4886.
Wyllie DJ, Behe P, Colquhoun D (1998) Single-channel activations and concentration jumps: comparison of recombinant NR1a/NR2A and NR1a/NR2D NMDA receptors. J Physiol 510:1-18.
Yao Y, Belcher J, Berger AJ, Mayer ML, Lau AY (2013) Conformational Analysis of NMDA Receptor GluN1, GluN2, and GluN3 Ligand-Binding Domains Reveals Subtype-Specific Characteristics. Structure 21:1788-1799.
Yelshansky MV, Sobolevsky AI, Jatzke C, Wollmuth LP (2004) Block of AMPA receptor desensitization by a point mutation outside the ligand-binding domain. J Neurosci 24:4728-4736.
Ylilauri M, Pentikainen OT (2012) Structural mechanism of N-methyl-d-aspartate receptor type 1 partial agonism. PLoS One 7:e47604.
Yuan H, Hansen KB, Vance KM, Ogden KK, Traynelis SF (2009) Control of NMDA receptor function by the NR2 subunit amino-terminal domain. J Neurosci 29:12045-12058.
Yuan H, Hansen KB, Zhang J, Pierson TM, Markello TC, Fajardo KV, Holloman CM, Golas G, Adams DR, Boerkoel CF, Gahl WA, Traynelis SF (2014) Functional analysis of a de novo GRIN2A missense mutation associated with early-onset epileptic encephalopathy. Nat Commun 5:3251.

Zhang W, Cho Y, Lolis E, Howe JR (2008) Structural and single-channel results indicate that the rates of ligand binding domain closing and opening directly impact AMPA receptor gating. J Neurosci 28:932-943.
Zheng J, Zagotta WN (2003) Patch-clamp fluorometry recording of conformational rearrangements of ion channels. Sci STKE 2003:PL7.
Zhou Y, Pearson JE, Auerbach A (2005) Phi-value analysis of a linear, sequential reaction mechanism: theory and application to ion channel gating. Biophysical journal 89:3680-3685.
Zuo J, De Jager PL, Takahashi KA, Jiang W, Linden DJ, Heintz N (1997) Neurodegeneration in Lurcher mice caused by mutation in delta2 glutamate receptor gene. Nature 388:769-773.